THESIS FOR THE DEGREE OF DOCTOR OF PHILOSOPHY

Data-driven Ship Performance Models - - Emphasis on Energy Efficiency and Fatigue Safety

XIAO LANG

Department of Mechanics and Maritime Sciences
CHALMERS UNIVERSITY OF TECHNOLOGY
Gothenburg, Sweden, 2023

Data-driven Ship Performance Models - - Emphasis on Energy Efficiency and Fatigue Safety

XIAO LANG

ISBN 978-91-7905-794-7

Doktorsavhandlingar vid Chalmers tekniska högskola
Ny serie nr 5260
ISSN 0346-718X

Chalmers University of Technology
Department of Mechanics and Maritime Sciences
Division of Marine Technology
SE-412 96, Gothenburg
Sweden
Telephone: +46 (0)31-772 1000
`www.chalmers.se`

Printed by Chalmers Reproservice
Gothenburg, Sweden, 2023

To my parents

Data-driven Ship Performance Models - - Emphasis on Energy Efficiency and Fatigue Safety

XIAO LANG
Chalmers University of Technology
Department of Mechanics and Maritime Sciences
Division of Marine Technology

Abstract

Due to digitalization in the maritime industry, a huge amount of ship operation-related data has been collected. The main objective of this thesis is to exploit machine learning/big data analytics to build data-driven ship performance models, focusing on speed-power relationship modeling, and fatigue accumulation assessment during a ship's operation at sea.

The speed-power performance models are established in three different ways: 1) semi-empirical white-box models, 2) machine learning black-box methods, and 3) physics-informed grey-box models. The white-box models include improved semi-empirical formulas for ship added resistance due to head waves, and further developed formulas in arbitrary wave headings. Validation studies using three case study ships show good agreement between the speed predictions by the white-box models and the long-term averages of full-scale measurements. Different supervised machine learning methods' capabilities have been compared for black-box modeling. The XGBoost algorithm is found to have the most reliable predictive ability, with the highest efficiency suitable for onboard devices. The novel grey-box models are proposed by considering the physical principles in model tests and big data information from real sailing. It has been demonstrated that the proposed grey-box models can improve prediction accuracy by approximately 30% for ship speed estimation and provides 50% less cumulative error of sailing time than the black-box methods.

The impact of voyage optimization-aided operations on the encountered wave conditions and ship fatigue damage is investigated in this thesis. By recommending appropriate routes, voyage optimization can greatly extend the fatigue life of a ship by at least 50%. The machine learning techniques are also applied to a ship's fatigue assessment. The results indicate that the proposed data-driven fatigue assessment models could increase accuracy by approximately 70% for the case study vessel compared to other prominent spectral methods.

Keywords: added resistance due to waves, ship performance, energy efficiency, speed-power relationship, fatigue assessment, full-scale measurements, grey-box, machine learning, semi-empirical.

Preface

This thesis presents research performed at the Department of Mechanics and Marine Sciences at Chalmers University of Technology from October 2018 to October 2022. Financial support for this research was provided by the European Commission (Horizon 2020) project EcoSail 820593, the Swedish Transport Administration project Via Kaizen TRV2019/119989, and the Vinnova project 2021-02768.

As my Ph.D. voyage is approaching its end, I would like to take the opportunity to recognize the people without whom this thesis would not have been possible.

First and foremost, I would like to express my deepest gratitude to Professor Wengang Mao for being my supervisor and for giving me the opportunity to become a Ph.D. student. Thank you for all the guidance, discussions and constant support in my studies, work and life that you have provided me for the last couple of years.

This gratitude also goes to my co-supervisor, Professor Jonas Ringsberg, head of the Division of Marine Technology. Thanks for your great support during the early stages of my academic life, your tireless work to ensure a stimulating and joyful research atmosphere in our division and to bring us all forward. Special thanks to my co-supervisor, Associate Professor Leif Eriksson, for providing fruitful guidance.

I would also like to thank all my current and former colleagues at the Division of Marine Technology for creating a pleasant work environment. Many thanks to Dr. Helong Wang for all the support and encouragement you have given me since I joined our group. Also, many thanks go to Dr. Da Wu for his fruitful feedback and ideas. I am also grateful to Dr. Shun-Han Yang for all the discussions we have had. Thank you Daiyong, Chi, and Daniel, for the nice cooperation and teamwork. Thank you Artjoms for being a good friend and nice neighbour in the office.

Special thanks to Muye, Xin, and their family for all the great moments we have experienced together in Gothenburg. I would also like to thank Hao, Yigeng, and Mengcheng for always being there for me. Thank you Naichen, Ze, Yuhan, Chengqian, Shaobo, Zhiyi, and all my friends in Sweden; you have lit up my life here.

Finally, this thesis is dedicated to my beloved family. Thank you my lovely cat Batman (Fufu in Chinese). Special thanks to my girlfriend Mengqiao, for your love and tireless encouragement. I would also like to express my sincerest gratitude to my dear parents for their constant support, love and encouragement over the years.

Xiao Lang
Gothenburg, December 2022

Contents

List of appended papers

Each of the six appended papers presents the data-driven ship performance models developed and implemented by the author of this thesis. The shipping companies provide full-scale measurements. The model experiment results are extracted from the public literature and provided by ship owners. The contributions of the authors to each paper are specified below in the list of papers.

Paper I	**X. Lang**, W. Mao. "A semi-empirical model for ship speed loss prediction at head sea and its validation by full-scale measurements". *Ocean Engineering*, vol. 209, 107494, Aug. 2020. DOI: 10.1016/j.oceaneng.2020.107494.
Paper II	**X. Lang**, W. Mao. "A practical speed loss prediction model at arbitrary wave heading for ship voyage optimization". *Journal of Marine Science and Application*, vol. 20, Dec. 2021. DOI: 10.1007/s11804-021-00224-z.
Paper III	**X. Lang**, D. Wu, W. Mao. "Comparison of supervised machine learning methods to predict ship propulsion power at sea". *Ocean Engineering*, vol. 245, 110387, Feb. 2022. DOI: 10.1016/j.oceaneng.2021.110387.
Paper IV	**X. Lang**, D. Wu, W. Mao. "Physics-informed machine learning models for ship speed prediction". Submitted to *Expert Systems with Applications.*
Paper V	**X. Lang**, H. Wang, W. Mao, N. Osawa. "Impact of ship operations aided by voyage optimization on a ship's fatigue assessment". *Journal of Marine Science and Technology*, vol. 26, Sep. 2020. DOI: 10.1007/s00773-020-00769-8.
Paper VI	**X. Lang**, D. Wu, C. Zhang, J.W. Ringsberg, W. Mao. "Machine learning methods for ship fatigue assessment". Submitted to *International Journal of Fatigue.*

Authors' contributions (CRediT):

Xiao Lang (All papers): Conceptualization, Methodology, Formal analysis, Writing - original draft, Writing - review & editing, Investigation, Validation, Visualization, Software.

Wengang Mao (All papers): Conceptualization, Resources, Writing - review & editing, Supervision, Project administration, Funding acquisition.

Da Wu (Paper III & IV & VI): Writing - review & editing, Supervision.

Helong Wang (Paper V): Writing - review & editing, Methodology (Voyage optimization), Software (Voyage optimization).

Naoki Osawa (Paper V): Writing - review & editing, Supervision.

Chi Zhang (Paper VI): Writing - review & editing, Investigation.

Jonas W. Ringsberg (Paper VI): Writing - review & editing, Supervision.

List of other selected papers by the author

Paper A **X. Lang**, W. Mao, D. Zhang, L.E.B. Eriksson, L. Jonasson, C. Zhang. "Comparison between full-scale measurements and theoretical fuel consumption model in a real Arctic ship navigation". In *Proc. The 29th International Ocean and Polar Engineering Conference*, Hawaii, USA, Jun. 2019.

Paper B **X. Lang**, W. Mao. "A simplified ship wave induced added resistance calculation method and full-scale measurements validation in head sea". In *Proc. The 30th International Ocean and Polar Engineering Conference*, Virtual, Online, Oct. 2020.

Paper C H. Wang, **X. Lang**, W. Mao. "Voyage optimization combining genetic algorithm and dynamic programming for fuel/emissions reduction". *Transportation Research Part D: Transport and Environment*, vol. 90, 102670, Jan. 2021. DOI: 10.1016/j.trd.2020.102670.

Paper D **X. Lang**, D. Wu, W. Mao. "Benchmark study of supervised machine learning methods for a ship speed-power prediction at sea". In *Proc. The 40th International Conference on Ocean, Offshore and Arctic Engineering*, Virtual, Online, Jun. 2021.

Paper E **X. Lang**, D. Wu, W. Mao. "A machine learning ship's speed prediction model and sailing time control strategy". In *Proc. The 32nd International Ocean and Polar Engineering Conference*, Virtual, Online, Jun. 2022.

Nomenclature

Greek notations

α	Parameter of S-N curve [-]
α_T	Draft coefficient [-]
$(1+\alpha_U)$	Advance coefficient [-]
β	Relative wave angle [deg.]
γ	Peak enhancement factor [-]
Γ	Gamma function [-]
ΔV	Speed reduction [knots]
ζ_a	Regular wave amplitude [m]
η_D	Propulsion efficiency [-]
η_h	Hull efficiency [-]
η_o	Open water efficiency [-]
η_r	Relative rotative efficiency [-]
η_s	Shaft efficiency [-]
θ	Wave spreading direction [deg.]
Θ	Ship heading [deg.]
ϑ	Mean wave direction [deg.]
λ	Wavelength [m]
λ_i	i-th stress spectral moment [MPa^2(rad/s)^i]
ξ_p	Smooth function[-]
ρ_A	Air density [kg/m^3]
Υ	L_2 regularization term [-]
φ_{CR}	Relative current direction [deg.]
φ_{WR}	Relative wind direction [deg.]
ω	Angular frequency [rad/s]
ω_p	Angular peak frequency [rad/s]
$\overline{\omega}$	Frequency factor [-]
$\overline{\omega_\beta}$	Encountered frequency factor [-]
$C_{\overline{\omega}}(\beta)$	Encountered frequency correction factor [-]

Latin notations

A_{XV}	Transverse projected area [m^2]
A_r	Cross-sectional area [m^2]
a_1	Amplitude factor [-]
a_2	Speed correction factor [-]
B	Ship width [m]
B_f	Bluntness coefficient [-]
B_i	Regression coefficient [-]
b_1	Slope adjustment factor [-]
C_{AA}	Wind resistance coefficient [-]
C_B	Block coefficient [-]
C_{H_s}	Ship propulsion power correction factor [-]
d	Fatigue damage accumulated in a stationary sea state [-]
d_1	Slope adjustment factor [-]
E	Average entrance angle [deg.]
F_a	Longitudinal force [N]
F_n	Froude number [-]
f_z	Frequency of zero-crossing [Hz]
g	Gravitational acceleration [N/kg]
H_s	Significant wave height [m]
k_e	Encountered wave number [-]
k_{yy}	Longitudinal radius of gyration [-]
k_1	Form factor [-]
L_E	Length of entrance [m]
L_{pp}	Ship length between perpendicular [m]
m	Parameter of S-N curve [-]
M_h	Horizontal bending moment [Nm]
M_t	Torsional moment [Nm]
M_v	Vertical bending moment [Nm]
m_1, m_2, m_3, m_4	Mean value, standard deviation, skewness, and kurtosis
P_B	Brake power [kW]

P_D	Propulsion power [kW]
P_E	Effective power [kW]
R_A	Model-ship correction resistance [N]
R_{AA}	Added resistance due to wind [N]
R_{APP}	Resistance of appendages [N]
R_{aw}	Non-dimensional added resistance due to wave [-]
R_{AW}	Added resistance due to wave [N]
R_{awr}	Non-dimensional added resistance due to wave reflection [-]
R_{awm}	Non-dimensional added resistance due to ship motion [-]
R_B	Wave resistance of bulbous bow [N]
R_{CALM}	Calm water resistance [N]
R_F	Friction resistance [N]
R_{TOTAL}	Ship total resistance [N]
R_{TR}	Additional resistance from immerses transom [N]
R_W	Wave resistance of bare hull [N]
S	Stress range [MPa]
T	Ship mean draft [m]
T_{aft}	Ship draft at stern [m]
T_{fwd}	Ship draft at stem [m]
T_R	Ship trim [m]
T_p	Wave peak period [s]
T_z	Mean wave period [s]
U_{wind}	Eastward wind speed [m/s]
V_{wind}	Northward wind speed [m/s]
$U_{current}$	Eastward current speed [m/s]
$V_{current}$	Northward current speed [m/s]
V	Speed through water [knots]
$\widehat{V_w}$	Expected speed in calm water [knots]
V_{CR}	Relative current speed [m/s]
V_g	Speed over ground [knots]
V_w	Speed through calm water [knots]
V_{WR}	Relative wind speed [m/s]

z_1, z_2, z_3	Surge [m], heave [m], and sway [m]
z_4, z_5, z_6	Roll [deg.], yaw [deg.], and pitch [deg.]

CHAPTER 1

Introduction

1.1 Background

Shipping is the backbone of international trade in the global economy, contributing to about 80% of global trade by volume (UNCTAD, 2018). Currently, one of the greatest challenges in the maritime industry is developing measures to reduce fuel costs and air pollutant emissions of ships, as well as enhance their safety.

From an energy efficiency perspective, the greenhouse gas (GHG) emissions from shipping increased from 977 million tonnes in 2012 to 1076 million tonnes in 2018 (9.6% increase), and the share of shipping emissions in global anthropogenic GHG emissions has increased from 2.76% in 2012 to 2.89% in 2018. Fossil fuel-induced emissions from shipping have attracted exceptional attention from both the public and maritime authorities. To reduce GHG emissions from shipping, as shown in Figure 1.1, a protocol was adopted to amend the convention; a new Annex VI was added to the MARPOL 73/78 convention in 1997 and entered into force in 2005 for the prevention of air pollution from ships. Furthermore, the 2011 amendments to MARPOL Annex VI introduced mandatory measures to reduce GHG emissions. A new chapter was added to Annex VI regarding “Regulations on the carbon intensity of international shipping”. The mandatory energy efficiency mechanism, i.e., ship Energy Efficiency Design Index (EEDI) has been enforced to regulate shipping energy efficiency since the 1st of January 2013 (IMO, 2011). In 2018, the IMO committed to reducing total annual GHG emissions from international shipping by at least 50% by 2050 (IMO, 2020). The amended regulations incorporate the new Energy

Efficiency Existing Ship Index (EEXI) and the Carbon Intensity Index (CII), which are measures that target improving the technical and operational efficiencies of ships. The amended regulations are scheduled to be enforced on the 1st of November 2022, with the requirements for EEXI and CII certifications coming into effect on the 1st of January 2023 (IMO, 2022).

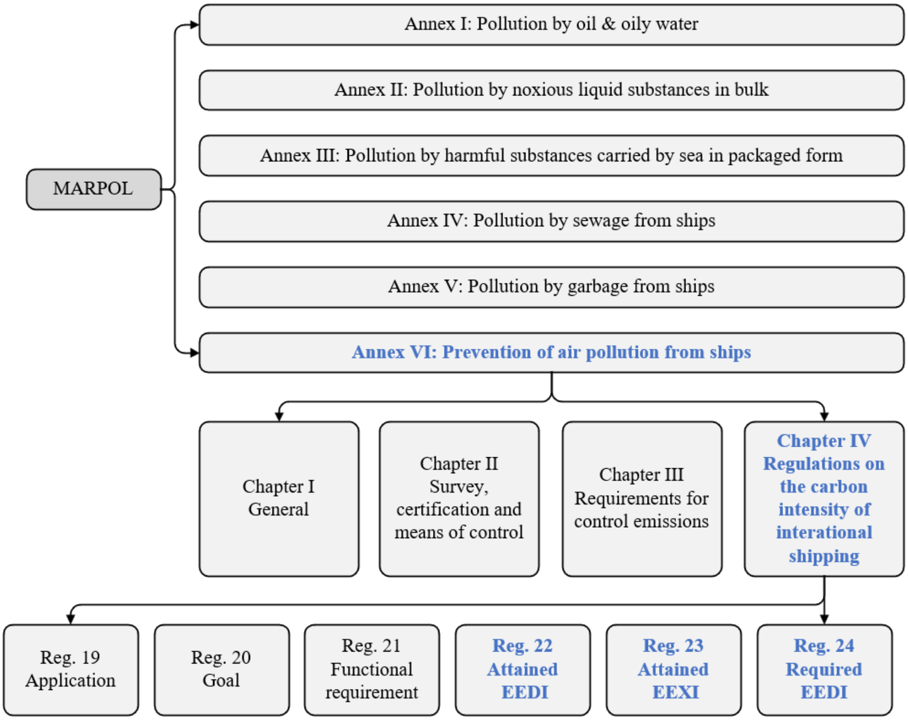

Figure 1.1: The evolution of IMO MARPOL energy efficiency regulations for ships.

For ocean-crossing ships, the fatigue damage accumulated on ships is always a big challenge to ship safety. Nowadays, the increase in ship size led to large ships undertaking more severe wave loads when sailing in the open sea, and the wide use of high-tensile steel for ship construction. The safety assessment of ship structures according to classification rules may lead to potential risks for the ships. For example, high-frequency vibration, also known as whipping/springing, observed in the full-scale measurements, is reported to contribute to a large part of the total fatigue (Storhaug, 2014). It may also lead to a significant increase in the extreme responses of ship structures. Consequently, fatigue failures and fractures occur earlier than expected in these vessels (Moe et al., 2005; Storhaug et al., 2007).

With the development of digitalization in shipping, a lot of sensors have been installed onboard ships to measure shipping energy efficiency and safety (motion, stress, etc.) related parameters. The collected data can be used to establish data-driven ship performance models, through big data analytics and machine learning methods. The performance models contribute to a better understanding of ship energy efficiency and safety, and monitor a ship's fuel consumption, sailing speed, and accumulated fatigue damage. For instance, in practical aspects, performance monitoring can help onboard crews obtain a more accurate estimated time of arrival (ETA). It can detect performance changes continuously over time due to biofouling on ship hulls/propellers, to schedule biofouling cleaning and maintenance for shipping companies. Additionally, the performance models can be embedded into different measures to increase shipping energy efficiency and safety. Ship voyage optimization system is one of the most attractive and widely implemented measures by the shipping industry (DNV GL, 2015). With the use of voyage optimization, ships can avoid harsh weather conditions and choose sailing routes that minimize fuel consumption (GHG emission), reduce the risk of ship and cargo damage, and increase arrival punctuality (Simonsen et al., 2015; Wang et al., 2017). The models describing the ship performance at sea are the core elements in evaluating optimization objective functions (Wang et al., 2020; Lang et al., 2020). Therefore, more accurate performance models are extremely important for the reliability and utilization of energy efficiency and safety measures.

1.2 Literature review and motivations

1.2.1 Ship speed-power modeling

In the energy system of a ship, certain key components, such as models that estimate ship total resistance and propulsive coefficients, are required for the speed-power model. A comprehensive overview of different generic semi-empirical models is systematically conducted in Tillig et al. (2017). In those semi-empirical models, the total resistance of a ship is often divided into three components: ship resistance in still water, namely, calm water resistance R_{CALM}, added resistance due to waves R_{AW} and added resistance due to wind R_{AA}. Added ice-induced resistance should also be considered if the ship sails in the Arctic. Different model uncertainties for estimating these components and their impacts on speed-power relationship are also discussed in Tillig et al. (2018).

The estimations of R_{CALM} and R_{AA} are often reliable through model tests or empirical formulas; however it is challenging to accurately estimate a ship's added resistance due to waves R_{AW} (Strom-Tejsen et al., 1973). Based on well-established seakeeping theories, models for estimating R_{AW} include two components (Pérez Arribas, 2007). The first is the diffraction-induced resistance when an incident wave reflects on the ship hull, dominating short waves. In the long-wave region, the added resistance is primarily caused by the drift force from radiated waves due to ship motions. The viscous effect is neglected since viscous damping is much smaller than the hydrodynamic damping of ship motions. Thus, the added resistance from waves can be regarded as a non-viscous phenomenon. This implies that the added resistance observed in model tests can be scaled up to approximate the resistance for full-scale results (Pérez Arribas, 2007). Even though experimental methods can provide reliable results of added resistance due to waves, it is too expensive. Numerical analyses based on slender-body theory or 3D panel method can also be used to estimate the added wave resistance (ITTC, 2018). Havelock (1942) made the first attempt to calculate this added resistance by integrating longitudinal pressure over the wetted hull of the ship. Boese (1970) continued Havelock's work using strip theory, developing a method known as the direct pressure integration method. Maruo (1957) proposed the superposition principle, where the wave-induced added resistance is proportional to the square of the wave amplitude. The momentum conservation method was then developed according to momentum balancing through the control volume of the ship hull (Maruo, 1960, 1963). The radiated energy method was initially introduced by Gerritsma and Beukelman (1972) and subsequently further implemented in head seas for a Series 60 hull (Salvesen, 1978). Parallel to these works, Faltinsen et al. (1980) proposed asymptotic formulas which estimate added resistance for wall-side ship hulls in short waves. Often, there are large uncertainties involved in these models. For instance, accurate measures of the reflected and diffracted resistances due to short waves are rarely available; these phenomena are nonlinear in nature, and the resulting values are small (Strom-Tejsen et al., 1973). Specifically, as the size of a modern ship increases, short-wave regions become progressively imperative. The ability to estimate the added wave resistance correctly is an essential factor in ship speed-power performance modeling.

Additionally, the theoretical methods mentioned above are relatively complicated as they rely on potential flow or strip theory-based numerical analyses to estimate ship motion responses (Tillig, 2020). The computational efforts required by such approaches typically ranges from minutes to days. Since the applications of those approaches generally require running the numerical analysis hundreds or thousands of times, those approaches are not feasible for the development and evaluation of energy efficient measures to guide ship operations, such as the voyage optimization system (ITTC, 2018).

Alternatively, various semi-empirical formulas have been developed based on the aforementioned theoretical models. Fujii and Takahashi (1975) applied solutions theorized by Ursell and Dean (1947) and developed the original formula for diffraction-dominated added resistance; further development was executed by Takahashi (1988) and Tsujimoto et al. (2008) using more experimental data, resulting in the NMRI method. Simultaneously, Jinkine and Ferdinande (1974) established a semi-empirical method for quickly calculating the added resistance of a cargo ship in the long-wave region. It was later developed for the short-wave region through several joint industry projects led by MARIN; the result is known as the STAwave-1 method (Boom et al., 2013). With the support of an extracted measurement database, the empirical STAwave-2 formula (ITTC, 2014) combines the Faltinsen et al. (1980) method for both short waves and long waves based on the technique of Jinkine and Ferdinande (1974). Liu et al. (2016) introduced a fast approach by statistically simplifying the combination of the above Faltinsen et al. (1980) and Jinkine and Ferdinande (1974) methods. It is denoted as the NTUA method in this thesis, based on existing experimental results and targets in engineering applications. Tillig (2020) averaged the STAwave-2 formula and the NTUA method with an angular function for oblique waves in the ShipCLEAN model. The abovementioned wave-induced added resistance developments are briefly summarized in Figure 1.2.

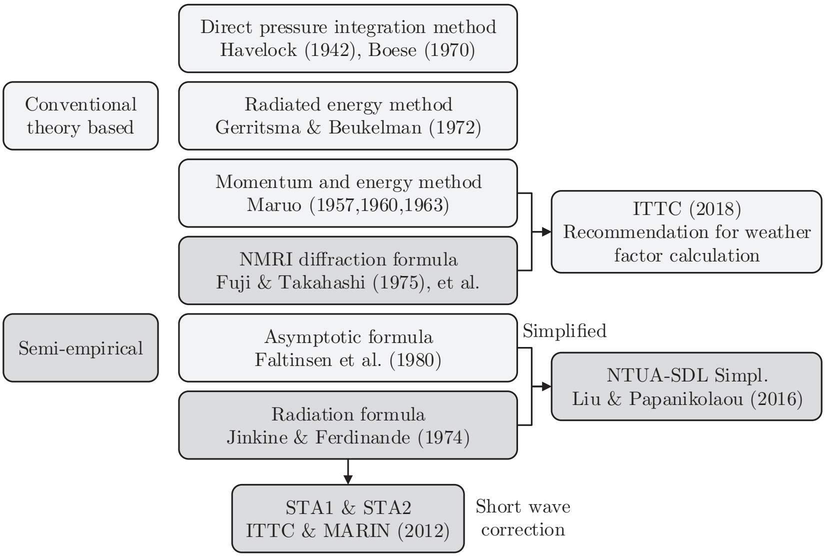

Figure 1.2: Summary of the development of various methods to estimate wave-induced added resistance.

Kwon (2008) extended the formulas developed by Townsin and Kwon (1982) to a direct speed loss (defined as the ship speed through water decrease in wind and waves in this thesis) estimation model that assesses the impact of weather in terms of the encountered wave and wind conditions. Kwon's method has been widely adopted for ship speed loss estimation in the development of voyage optimization systems (Larsson et al., 2015; Lu et al., 2015; Shao et al., 2012). This method only takes into account ship type, block coefficient, and other operating conditions as inputs. Since it has not considered other ship characteristics, there may be potential uncertainties. It was reported in Lu et al. (2015) that significant deviations could be found between the predictions and measurements for each specific ship. Bolbot and Papanikolaou (2016) and Yasukawa and Masaru (2020) also found that the bow shape has a high influence on the magnitude of added resistance. Recently, data-driven techniques have been increasingly employed in the realm of wave-induced added resistance. The indirect measurement of added wave resistance from an in-service container ship was estimated by Nielsen et al. (2021). Liu and Papanikolaou (2020) proposed a regression model for arbitrary wave headings, that added a few parameters and various piecewise resistance components, trying to give the best fit to a large amount of experimental data. Machine learning methods have been applied for the wave-induced added resistance estimation, by using artificial neural networks and tree-based ensemble methods (Cepowski, 2020; Herradon de Grado and Bertram, 2016; Mittendorf et al., 2022a).

With the fast development of measurement sensor technology, present ships are instrumented with different sensors to measure ship navigation related parameters. A large amount of ship energy performance related data is collected to better understand a ship's energy performance, i.e., ship speed-power relationship in terms of encountered sea environments (Berthelsen and Nielsen, 2021; Dalheim and Steen, 2020; Huffmeier and Mathias, 2021). Sophisticated machine learning methods have been implemented to build data-driven models that predict propulsion power or fuel consumption. For example, the artificial neural networks (ANNs) were used to establish data-driven ship performance models for the estimation of shaft power of large merchant ships based on either simulated and full-scale data (Bal Beşikçi et al., 2016; Laurie et al., 2021; Moreira et al., 2021; Parkes et al., 2018; Petersen et al., 2012; Theodoropoulos et al., 2021; Zhang et al., 2019). Canbulat et al. (2019) applied Bayesian belief network to quantify energy performance for a dry bulk on the ship-port interface. In Kim et al. (2021), six months of in-service data of a container ship was used to compare the capability of ANNs and multiple linear regression, establishing the relationship between fuel consumption and main engine RPM, ship speed, and other parameters. Brandsæter and Vanem (2018) compared different regression models for the speed-shaft thrust relationship establishment of an ocean-going ship based on full-scale measurements over several months. Karagiannidis and Themelis (2021) investigated the effect of data pre-processing on the ship fuel consumption machine learning modeling. The low resolution of noon report data was also used to build data-driven models for fuel consumption predictions. For example, back-propagation neural networks and Gaussian process regression (GPR) are used in Hu et al. (2019) to predict the fuel consumption in terms of shaft power. The GPR was also used in Yoo and Kim (2019) to model the power performance of a container ship based on engine RPM. Different machine learning methods were compared for predicting the fuel consumption and shaft power based on 780 navigational noon report records (Uyanık et al., 2020). Mittendorf et al. (2022b) applied the adaptive training methodology to estimate the speed-power model drift caused by biofouling, for an LNG tanker service over a five-year span.

There is also an emerging trend to study data-driven methods to improve both ship speed predictions and energy efficiency measures. Petersen et al. (2012) compared ANNs and GPR for the fuel consumption and ship speed prediction of a domestic ferry by using two-month data sets totalling 254 trips. Tree-based supervised machine learning algorithms as well as rigid and lasso regressions were applied for the ferry data set by Soner et al. (2018, 2019) and Bassam et al. (2022). Mao et al. (2016F) applied a 2nd-order autoregression model to establish the relationship between ship speed and engine RPM and extracted sea environments from one-year measurements of a container ship. Gan et al. (2017) constructed a multi-layer perceptron network for long-term speed prediction of inland ships using AIS data. Coraddu et al. (2019) proposed a deep learning model to estimate the speed loss of two Handymax chemical/product tankers based on two-year onboard measurements, with main engine fuel consumption, auxiliary engine power, shaft power, ship draft and metocean data as input features. Some studies have been conducting regarding machine learning ship speed modeling (Abebe et al., 2020; Milaković et al., 2020; Moreira et al., 2021; Yuan et al., 2021).

Ship performance models based on first principles or semi-empirical methods are often referred to as white-box models (WBMs). The data-driven regression/machine learning models are classified as black-box models (BBMs). A third model category, grey-box models (GBMs), is classified by Haranen et al. (2016). GBMs combine the physical properties underlying WBMs and the knowledge from operational data in BBMs. Except for much fewer full-scale data requirements than BBMs and higher accuracy than WBMs, GBMs also have good model interpretability and extrapolation capability. They can avoid unreasonable predictions for unseen scenarios. The advantages and disadvantages of different model types are summarized in Table 1.1.

Current research on ship speed-power modeling is conducted with either BBMs based on data, or WBMs based on first principles. For BBMs, often very low-resolution data, such as noon reports, is used for the model training due to the lack of access to ship data. Those ship speed-power performance models are primarily trained to monitor and estimate the fuel/power consumption and speed of a ship in terms of ship operational parameters. However, to apply data-driven ship models for energy efficiency measures in optimal ship operations, it is essential to model energy performance in metocean conditions. Some products of data-driven ship performance models have already been developed, such as those from BMT (2021), GreenSteam (2021), HITACHI (2021), and NAPA (2021). Almost all of these models use the same machine learning technique, artificial neural networks, to establish BBMs that describe the energy performance of a ship. The capability and sensitivity of those models were not well discussed in the public community.

Table 1.1: Advantages and disadvantages of WBMs, BBMs and GBMs.

Type	Description	Advantage	Disadvantage
WBMs	Based on prior knowledge and physical principles	Do not need historical data and can extrapolate beyond the given data range with good interpretability	Requires extensive prior knowledge, and the accuracy depends on assumptions and uncertainties implicit in the model
BBMs	Established using experimental or full-scale sailing data and is purely data-driven	Do not require prior knowledge and are more accurate than WBMs	Require large number of full-scale measurements, model interpretability and extrapolation is poor, and may result in unreasonable results for unseen data
GBMs	Developed based on physical properties underlying WBMs and knowledge from operational data in BBMs	Less full-scale data required than for BBMs, higher accuracy than WBMs, contains good model interpretability and extrapolation capability and can avoid unreasonable results for unseen data	

1.2.2 Ship fatigue assessment

Fatigue damage accumulated on ships when sailing at sea is an important challenge for ship safety. The investigation by Jordan and Cochran (1978), as well as that of Jordan and Knight (1978) for commercial ships in the United States, showed that there were, on average, 86 structural failures (cracks) per ship at any inspection. Different fatigue assessment methods were proposed to predict the fatigue life of ship structures. If time series of detailed structural stresses are available, the corresponding fatigue damage can be straightforwardly estimated by the rainflow counting method based on Palmgren–Miner's rule (Miner, 1945; Palmgren, 1924). The rainflow counting method carried out in the time-domain is often taken as the "truth". The definition of the rainflow counting method has been detailed in de Jonge (1982), Rychlik (1987), and Rychlik (1993).

For ship fatigue design and assessment, the time series of stresses are not always available, since only a small number of ships have been employed with sensors (and in a short measurement campaign) to measure structural strain/stress. Simulating those time series stresses for large amounts of sea states requires expensive computation efforts. Therefore, ship fatigue design is commonly conducted in the frequency domain by assuming Gaussian processes, also known as the narrow-band approximation (Rychlik, 1987). However, except for general uncertainties such as fatigue accumulation law, significant uncertainties remain in current fatigue assessment methods (Dong et al., 2022; Fricke et al., 2002; ISSC, 2018; Lang et al., 2020), wave load and structural stress calculations (Li et al., 2014; Yang et al., 2021; Yosri et al., 2022), wave modeling (Mao et al., 2010; Olsen et al., 2006), and structural analysis (Fricke, 2017; Gaidai et al., 2019; Thompson, 2018; Yamamoto, 2017). Since actual ship fatigue loads are not narrow-banded, several correction methods were proposed to improve the approximation, such as Jiao and Moan (1990) considering the bimodal spectral response, and Dirlik (1985), Tovo (2002), and Zhao and Baker (1990) simulating or modeling the probability distribution of stress range. An empirical formula between stress range and ship encountered significant wave height was also proposed for fatigue design and operations (Mao et al., 2010). Furthermore, fatigue loads of a ship are not Gaussian distributed. Models included the third and fourth stress spectral moments were proposed by Winterstein (1985, 1988). Figure 1.3 presents a typical procedure for direct fatigue assessment according to classification guidelines (DNV GL, 2018) and potential uncertainties associated with each assessment step.

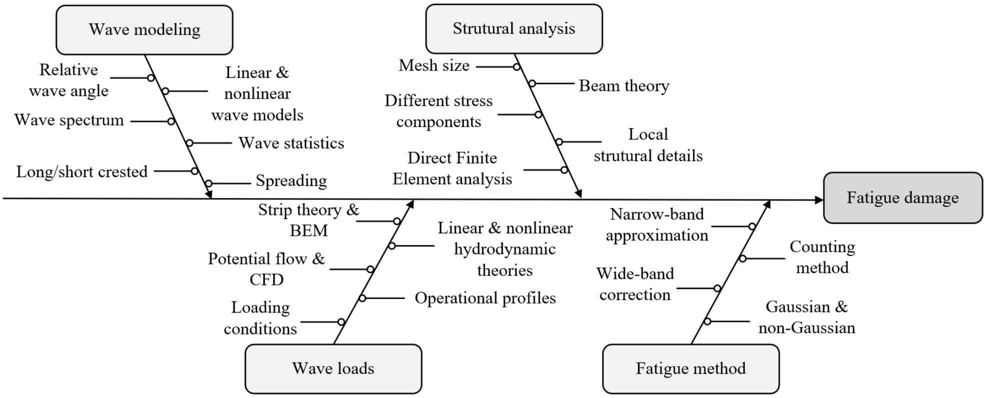

Figure 1.3: Modeling diagrams of ship response (stress) and associated uncertainties for fatigue analysis.

With the digitization of the current shipping industry, large quantities of data are collected to monitor the stress signals of a ship, indicating fatigue accumulation (Mao, 2014; Storhaug, 2014). Data-driven approaches have been used in fatigue analysis and structure life prediction (Bao et al., 2021; Feng et al., 2023; He et al., 2021; Masoudi Nejad et al., 2022; Yan et al., 2019). However, little research has been done using machine learning techniques to investigate how ship fatigue damage accumulates in terms of encountered wave conditions during actual navigation.

Data-driven approaches can be straightforward ways to assess ship fatigue damage based on measurement data. For example, if the motion based fatigue model is established, ship fatigue damage can be monitored through the ship's motion monitoring signal. Furthermore, if a metocean condition based fatigue model is feasible, the ship fatigue damage accumulation can be predicted using environmental data. More importantly, these data-driven models will not involve the uncertainties that existed in the traditional assessment procedure, as Figure 1.3 shows. The data-driven methods have the potential to establish more robust ship fatigue assessment models.

1.3 Objectives

The main objective of this thesis is to explore machine learning/big data analytics to build data-driven ship performance models, focusing on speed-power relationship modeling, and accumulated fatigue assessment during a ship's operation at sea. Different methodologies to establish such speed-power performance models should be investigated, including 1) semi-empirical white-box models, 2) machine learning black-box methods, and 3) physics-informed grey-box models. The data-driven ship fatigue assessment method should consider the encountered environmental conditions. To achieve the overall objective, eight main tasks and research activities have been conducted in this thesis:

1. A speed-power performance white-box model is developed in head waves, with improved semi-empirical formulas for added resistance due to head waves.
2. The white-box model and semi-empirical formulas are further developed from addressing head waves to also addressing waves from arbitrary angles. These WBMs are developed to allow for fast calculation while achieving acceptable accuracy.
3. The impact of speed-power performance WBMs on the voyage optimization of a ship regarding sailing trajectories and encountered wave environments is studied.
4. Different machine learning and statistical methods' capabilities for ship speed-power performance modeling are investigated and compared. Ship operational profiles and encountered metocean data are applied as training features.
5. The black-box model established by the suitable machine learning algorithm is applied for sensitivity analysis, in terms of the data volume, stationary period of each data sample, and online performance prediction.
6. Physics-informed speed-power performance grey-box models are developed by combining physical principles from WBMs, with big data inferences from BBMs. The proposed GBMs have better model interpretability, and extrapolation capability for unseen scenarios than BBMs.
7. The impact of ship voyage optimization on encountered wave environments and ship fatigue life is investigated.

8. A machine learning black-box model is established for ship fatigue assessment by considering encountered wave conditions. The benefits of using the proposed BBM for fatigue assessment compared to conventional spectral methods are demonstrated.

1.4 Assumptions and limitations

The added resistance formulas are derived from a series of model test measurements from public literature. Most model tests were conducted at the design loading condition, which is the most common ship sailing condition (Lang et al., 2022). Thus, the semi-empirical formulas and white-box models in this study are verified at the design loading condition, and have not investigated the variation in draft and trim. To establish and verify the data-driven speed-power and fatigue assessment models, several assumptions are made:

1. The shallow water effects have not been considered throughout the data-driven performance models' development. Only the open sea (deep water) full-scale data are filtered for the performance model establishment and verification.
2. This study relies fundamentally on the assumption that the reanalysis dataset represents the ground truth of the encountered metocean conditions. The author has not tried to investigate the validity of the hindcast data, but is aware that there might be uncertainties involved. Since onboard metocean measurements are not available, the spatio-temporal interpolation of the hindcast data is reasonable and widely used in state-of-the-art research.
3. The full-scale measurements of ship operations data are assumed to be accurate enough to reflect the actual performance when sailing in a real seaway. The aleatoric uncertainties of the measurements exist, but for the models establishment and verification, the measurements were filtered for erroneous samples.
4. Other environmental parameters, such as water temperature, and salinity, are assumed to have negligible influences. This study has not considered the impacts of biofouling on ship resistance. To minimize uncertainties involved in biofouling, the white-box models verification is based on the long-term average of full-scale measurements, and dataset for cross-validation in black-box and grey-box modeling has been shuffled in time series.
5. The collected model test results regarding wave-induced added resistance from available publications are assumed to be correct and reliable.

1.5 Outline of the thesis

The research activities performed in this thesis are summarized in the six appended papers. A white-box speed-power model is proposed in Paper I, including improved semi-empirical formulas for added resistance due to head waves. The white-box model and semi-empirical formulas in head waves are extended to arbitrary wave headings in Paper II. Paper III compares different machine learning black-box techniques for ship propulsion power modeling. Furthermore, a novel, physics-informed machine learning method is proposed in Paper IV that establishes the grey-box model for ship speed prediction. Paper V investigates the impacts of voyage optimization on wave statistics and, consequently, the fatigue life of the ship. The machine learning technique is then applied in Paper VI to establish a data-driven fatigue assessment model. Figure 1.4 illustrates the interconnectedness of the scope of the papers.

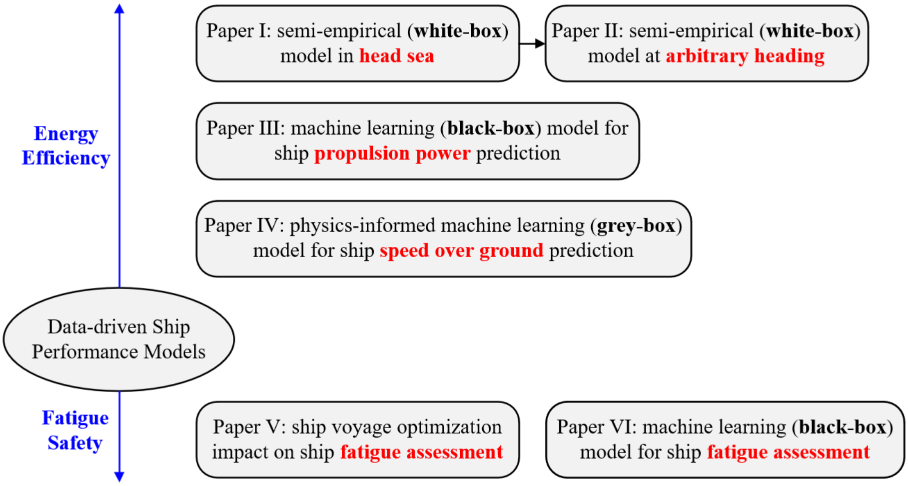

Figure 1.4: Structure and workflow of the appended papers to achieve thesis objectives.

From Figure 1.4, the left portion illustrating this thesis is organized as follows. In Chapter 2, the proposed methodologies for ship speed-power performance modeling are briefly described. For the completeness of this thesis, the general ship propulsion concept, the semi-empirical formulas developed in Papers I and II, and the machine learning black-box/grey-box models in Papers III and IV are presented. Chapter 3 introduces the method for ship fatigue assessment by the traditional method as well as the developed machine learning model from Papers V and VI. The experimental model tests, full-scale measurements, and related data processing are elaborated in Chapter 4. Chapter 5 presents selected important results and summaries. The conclusions are presented in Chapter 6, followed by some possible future research in Chapter 7.

CHAPTER 2

Method for the ship speed-power modeling

2.1 General concept of ship propulsion

The energy system of a ship normally includes energy consumption due to propulsion, heating and auxiliary equipment (Woud and Stapersma, 2002). Fuel consumption in a seaway is dependent on many parameters, such as marine engine operating parameters, propeller efficiency and ship resistance (Carlton, 2012). Ship propulsion power is generally connected to the sailing speed and the encountered sea environments. To estimate ship propulsion power/fuel consumption, a typical workflow is illustrated in Figure 2.1.

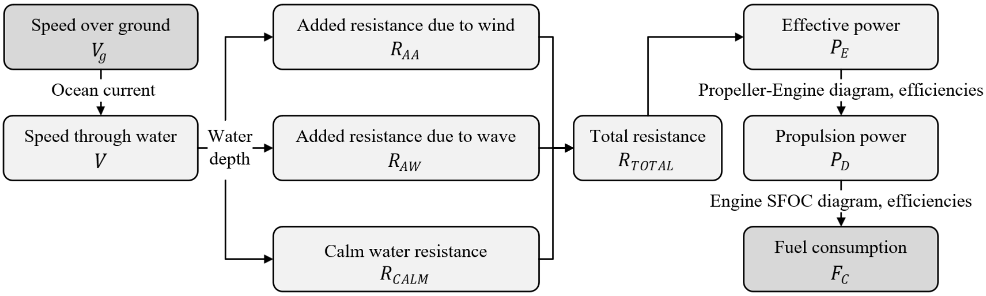

Figure 2.1: Typical workflow for the conventional estimation of the speed to propulsion power/fuel consumption of a ship.

In the workflow, the first step is acquiring ship resistance at different sailing speeds by either model tests, numerical computation methods or semi-empirical formulas. When a ship is sailing in a seaway, the wave and wind environments affect ship performances for most of her journey time. Hence, added resistance due to wind R_{AA} and wave R_{AW} should also be accounted for when estimating the total resistance R_{TOTAL}. The total resistance of a ship must be compensated by the thrust force provided by propellers powered by marine engines with certain RPM under various work conditions. The engine configuration, propeller efficiencies and fuel-related factors of a ship will be used to compute the propulsion power and fuel consumption for sailing under different operational and environmental conditions.

The power required to take a ship sailing forward with at a specific speed through water V, overcoming total resistance R_{TOTAL}, is namely effective power P_E:

$$P_E = R_{TOTAL} \times V \tag{2.1}$$

where the effective power P_E is transmitted from the onboard marine engine supplied brake power P_B, that generates the propulsion power P_D to rotate the propeller:

$$P_B = \frac{P_D}{\eta_s} = \frac{P_E}{\eta_s \cdot \eta_h \cdot \eta_r \cdot \eta_o} \tag{2.2}$$

where η_s is shaft efficiency, η_h is hull efficiency, η_o is open water efficiency, and η_r is relative rotative efficiency. The fuel consumption can then be predicted from the multiplication of the engine brake power P_B, with the specific fuel oil consumption (SFOC) and operation time. Dependent on the engine type and propeller properties used on a specific ship, propulsion efficiency is often provided by the manufactures or ship owners and can be used to calculate the final fuel consumption.

2.2 Total resistance of a ship in a real seaway

2.2.1 Calm water resistance

An approximate calm water resistance calculation method was proposed by Holtrop and Mennen (1982), based on full-scale trials and model experiments. The method accounts for the main dimensions, type, appendage arrangement and immersed transom sterns of a ship. The total resistance in still water is divided into six different components:

$$R_{CALM} = R_F(1 + k_1) + R_{APP} + R_W + R_B + R_{TR} + R_A \tag{2.3}$$

where the frictional resistance R_F is estimated by ITTC-1957 frictional correlation line (ITTC, 2002), and the empirical formulas calculate the form factor $1 + k_1$, the resistance of appendages R_{APP}, wave resistance of bare hull R_W, wave resistance of bulbous bow R_B, additional resistance from immersed transom R_{TR} and model-ship correlation resistance R_A.

Additionally, suppose the towing tank resistance test results are available. In that instance, the calculation of calm water resistance is preferentially performed using the interpolation of the measurement value to avoid the potential deviation of different types of ships.

2.2.2 Added resistance due to wind

The wind-induced added resistance is determined by the area of the ship superstructure and the relative wind. The relative wind is the vectorial summation of the ship speed and direction as well as the wind speed and direction (Lewis, 1988). In this study, the added resistance due to wind is predicted by the ISO (2015) guideline:

$$R_{AA} = \frac{1}{2}\rho_A \left[C_{AA}\left(\varphi_{WR}\right) A_{XV} {V_{WR}}^2 - C_{AA}(0) A_{XV} {V_g}^2\right] \tag{2.4}$$

where ρ_A is air mass density, A_{XV} is the transverse projected area above waterline included superstructures, V_{WR} is relative wind speed, φ_{WR} is relative wind direction, V_g is ship speed over ground (here convert in m/s), C_{AA} is the wind resistance coefficient and $C_{AA}(0)$ represents the wind resistance coefficient in head wind. The wind resistance coefficients are based on the data derived from huge amounts of model tests performed in the wind tunnel.

2.2.3 Added resistance due to waves

An actual sea state is typically multiplied by a spreading function $D(\theta)$ and a wave spectrum of predefined formats. In this study, a Cosine-Squared spreading function $D(\theta)$ and the the Jonswap wave spectrum are applied to describe irregular waves of actual sailing wave conditions (Hasselmann et al., 1973):

$$D(\theta) = \begin{cases} \frac{2}{\pi}\cos^2(\theta) & \text{for} - \frac{\pi}{2} \leq \theta \leq \frac{\pi}{2} \\ 0 & \text{otherwise} \end{cases} \tag{2.5}$$

$$S(\omega|H_s, T_p, \gamma)D(\theta) = \frac{320{H_s}^2}{{T_p}^4\omega^5} \exp\left(\frac{-1950}{{T_p}^4\omega^4}\right)\gamma^{\exp\left[\frac{-(\omega-\omega_p)^2}{2\sigma^2{\omega_p}^2}\right]} D(\theta) \tag{2.6}$$

where θ is the wave spreading direction. The spectrum is described by the significant wave height H_s, wave peak period T_p and peak enhancement factor γ (set to the standard value 3.3). The spectral width parameters are $\sigma = 0.07$ for $\omega \leqslant \omega_p$, $\sigma = 0.09$ when $\omega > \omega_p$.

The added resistance due to wave R_{AW} in a real seaway consisting of irregular waves, is conventionally estimated by integrating wave resistance in regular waves $R_{aw}(\omega)$ multiplied with the wave spectrum $S(\omega)$ over the entire range of wave frequency w:

$$R_{AW}(\omega|H_s, T_p, \gamma, V, \beta) = 2\int_0^{\infty}\int_{-\frac{\pi}{2}}^{+\frac{\pi}{2}} S\left(\omega|H_s, T_p, \gamma\right) \frac{R_{aw}\left(\omega|V, \beta\right)}{\zeta_a(\omega)^2} D(\theta-\beta) d\theta d\omega \tag{2.7}$$

where $\zeta_a(\omega)$ is the amplitude of the regular wave to achieve the added resistance $R_{aw}(\omega)$, β is the relative wave angle ($\beta = 0°$ stands for head sea). The term R_{aw}/ζ_a^2 is often referred as the transfer function (RAOs) of the added resistance in waves.

2.3 Semi-empirical white-box model for added resistance in waves

For a ship sailing with speed through water V and relative wave angle β, the added resistance in regular waves of frequency ω can be evaluated by the sum of two components, i.e., added resistance due to wave reflection R_{awr} and added resistance due to ship motions R_{awm} (Strom-Tejsen et al., 1973):

$$R_{aw}(\omega|V,\beta) = R_{awr}(\omega|V,\beta) + R_{awm}(\omega|V,\beta) \tag{2.8}$$

where $R_{awr}(\omega|V,\beta)$ and $R_{awm}(\omega|V,\beta)$ are assumed to be uncoupled. The added resistance in waves is regarded as a non-viscous phenomenon.

2.3.1 Added resistance due to wave reflection

$R_{awr}(\omega|V,0)$ in head wave

Fujii and Takahashi (1975) initially introduced the semi-empirical formula for diffraction-induced added resistance four decades ago, and it was further developed by Tsujimoto et al. (2008) as the primary NMRI method. The added resistance due to wave reflection in head wave $R_{awr}(\omega|V,0)$ is given by $\frac{1}{2}\rho g \zeta_a^2 B B_f \alpha_T \left(1+\alpha_U\right)$, where the draft coefficient α_T and advance coefficient $(1+\alpha_U)$ have further calibrated based on the supplementary experimental data (Kuroda et al., 2008; Takahashi, 1988; Tsujimoto et al., 2008); the advance coefficient was determined as:

$$1+\alpha_U = 1 + C_U F_n, \text{ where } C_U = \max(-310 B_f + 68, 10) \tag{2.9}$$

where the bluntness coefficient B_f is usually estimated by the integration method, considering the shape of water plane and encountered wave direction. The bluntness coefficient is simplified by Liu et al. (2016), and it is highly correlated to the block coefficient as an approximation expression:

$$B_f = 2.25 \sin^2 E \tag{2.10}$$

The average entrance angle $E = \arctan(B/2L_E)$ is defined by the ship width B and length of entrance L_E. Notably, the length of entrance has been modified to the length between the fore perpendicular and the point where it reaches 99% ship width at the waterline surface (Liu et al., 2016). The latest developed draft coefficient $\alpha_T = 1 - e^{-2kT}$ was evolved, instead of the NMRI version of Bessel function, due to the exponential decay that is observed to be more equivalent to the real physical wave energy dissipation (Liu et al., 2016; Valanto and Hong, 2015).

However, it still cannot catch up the tail increase for high-frequency wave reflection, as DTC container, KVLCC2 tanker and HSVA cruise model tests presented in el Moctar et al. (2012), Guo and Steen (2011), Liu et al. (2016), Sadat-Hosseini et al. (2013), and Valanto and Hong (2015). In the proposed model, a wavelength correction factor was thusly added and tuned in NMRI expression. The new modified formula presents a significantly better prediction performance in the short-wave region, which matches the reasonable resistance increase owing to the extremely short wave. The formula expression is given as:

$$R_{awr}(\omega|V,0) = \frac{1}{2}\rho g \zeta_a^2 B B_f \alpha_T \left(1+\alpha_U\right) \left(\frac{0.19}{C_B}\right)\left(\frac{\lambda}{L_{pp}}\right)^{F_n - 1.11} \tag{2.11}$$

The wavelength correction factor is settled by block coefficient C_B, Froude number F_n and the ratio between wavelength λ and ship length L_{pp}. However, $k_e T$ is proposed to replace kT as the non-dimensional frequency in the draft coefficient:

$$\alpha_T = 1 - e^{-2k_e T} \tag{2.12}$$

where $k_e = k(1 + \Omega \cos\beta)^2$ and $\Omega = \frac{\omega V}{g}$, the circular frequency of incident regular waves is ω and wave number of incident regular waves is k.

$R_{awr}(\omega|V,\beta)$ at arbitrary wave heading

For the added resistance due to wave reflection at other encountered relative wave angles, the magnitude of $R_{awr}(\omega|V,\beta)$ has shown a decline from the head wave to the following sea, as the heading angle β increases. Minor negative values are observed in the HSVA cruise, DTC container and a bulk carrier model tests for a few short waves at $120° \leqslant \beta \leqslant 180°$el Moctar et al. (2012), Kadomatsu (1988), and Valanto and Hong (2015). Thus, a simplified modification factor, $\cos\beta$, is proposed to express the physical phenomenon.

The advance coefficient is another parameter tuned by Froude number F_n and the encountered relative wave angle β, by ceiling and floor functions. The resistance force has been investigated, and an obvious increase is observed when $\beta \leqslant 90°$; the negative values become weaker when β exceeds 90°, with a higher F_n. The modified added resistance due to wave reflection for arbitrary wave angles is written as:

$$R_{awr}(\omega|V,\beta) = \begin{cases} R_{awr}(\omega|V,0) \cdot F_n^{(\lfloor\cos\beta\rfloor - \lceil\cos\beta\rceil)F_n} \cos\beta & \text{for } 0 \leqslant \beta \leqslant \frac{\pi}{2} \\ R_{awr}(\omega|V,0) \cdot F_n^{-1.5(\lfloor\cos\beta\rfloor + \lceil\cos\beta\rceil)F_n} \cos\beta & \text{for } \frac{\pi}{2} < \beta \leqslant \pi \end{cases} \tag{2.13}$$

2.3.2 Added resistance due to ship motion

$R_{awm}(\omega|V,0)$ in head wave

Parallel to the NMRI formula, Jinkine and Ferdinande (1974) developed their approximate formula for ship motion-induced added resistance calculations in the long-wave region. This formula was derived through the experimental data of a fine hull fast cargo ship for $F_n \geq 0.12$ condition. The original model is given by:

$$R_{awm}(\omega|V,0) = 4\rho g \zeta_a^2 B^2 / L_{pp} \overline{\omega}^{b_1} \exp\left[\frac{b_1}{d_1}\left(1 - \overline{\omega}^{d_1}\right)\right] a_1 a_2 \tag{2.14}$$

where a_1 is the amplitude factor, a_2 is the speed correction factor, b_1, d_1 is the slope adjustment factor and $\overline{\omega}$ is the frequency factor. The amplitude factor was formulated by Jinkine and Ferdinande (1974) and has been continually modified. The most recent expression was developed by Liu et al. (2016), and further parameters tuned in this study viz:

$$a_1 = 60.3 {C_B}^{1.34} \left(\frac{1}{C_B}\right)^{1+F_n} \tag{2.15}$$

while block coefficient C_B and Froude number F_n were used as modification parameters. The speed correction factor a_2 has been extended to the span $0 \leqslant F_n \leqslant 0.3$, compared to the original high speed domain (Grin, 2012; ITTC, 2014; Liu et al., 2016). The speed correction factor a_2 is sensitive to the longitudinal radius of gyration k_{yy} and the block coefficient C_B in the high-speed region, ascertained through careful analysis of experimental data. Moreover, it has a slightly steeper slope compared to the formula in Liu et al. (2016) when $F_n < 0.12$. Hence, the following formula is consequently introduced:

$$a_2 = \begin{cases} 0.0072 + 0.24F_n & \text{for } F_n < 0.12 \\ {F_n}^{-1.05C_B + 2.3} \exp((-2 - \lceil \frac{k_{yy}}{0.25} \rceil - \lfloor \frac{k_{yy}}{0.25} \rfloor)F_n) & \text{for } F_n \geq 0.12 \end{cases} \tag{2.16}$$

where the ceiling and floor functions allow for discrete scales of F_n, concerning the correlation between k_{yy} and the typical value 0.25 (ITTC, 2017).

The frequency factor $\overline{\omega}$ is determined by the frequency of heave and pitch motions. The resonance responses of these motions are regarded as the leading cause of radiation-induced added resistance, reaching the peak value in head wave. Liu et al. (2016) have separated the expression to lower and normal speed. Still, it may not match the experimental data well for some instances when k_{yy} do not equal 0.25, especially for HSVA cruise (Liu et al., 2016; Valanto and Hong, 2015). The resonance position has been observed to move horizontally from $\lambda/L_{pp} < 1$ to $\lambda/L_{pp} > 1$ with higher Froude number F_n. The longitudinal radius of gyration variation also influences this trend. Consequently, the expression is further adjusted in this study, and the modified formula is given by:

$$\overline{\omega} = \begin{cases} \dfrac{\sqrt{L_{pp}/g}\,\sqrt[c_1]{k_{yy}}\,0.05^{0.143}}{1.09 + \lceil \frac{k_{yy}}{0.25} \rceil 0.08}\omega & \text{for } F_n < 0.05 \\ \dfrac{\sqrt{L_{pp}/g}\,\sqrt[c_1]{k_{yy}}\,{F_n}^{0.143}}{1.09 + \lceil \frac{k_{yy}}{0.25} \rceil 0.08}\omega & \text{for } F_n \geq 0.05 \end{cases} \tag{2.17}$$

where the root $c_1 = 0.4567\frac{C_B}{k_{yy}} + 1.689$, and the improved expression results are more fit to the resonance position in experimental measurements. The slope adjustment factors are also further calibrated in this study, concerning the longitudinal radius of gyration k_{yy} and the block coefficient C_B:

$$b_1 = \begin{cases} (19.77\frac{C_B}{k_{yy}} - 36.39)/\lceil \frac{k_{yy}}{0.25} \rceil & \text{for } \overline{\omega} < 1, C_B < 0.75 \\ 11/\lceil \frac{k_{yy}}{0.25} \rceil & \text{for } \overline{\omega} < 1, C_B \geqslant 0.75 \\ -12.5/\lceil \frac{k_{yy}}{0.25} \rceil & \text{for } \overline{\omega} \geqslant 1, C_B < 0.75 \\ -5.5/\lceil \frac{k_{yy}}{0.25} \rceil & \text{for } \overline{\omega} \geqslant 1, C_B \geqslant 0.75 \end{cases} \tag{2.18}$$

$$d_1 = \begin{cases} 14 & \text{for } \overline{\omega} < 1, C_B < 0.75 \\ 566\left(\frac{L_{pp}}{B}\right)^{-2.66} \cdot 2 & \text{for } \overline{\omega} < 1, C_B \geqslant 0.75 \\ -566\left(\frac{L_{pp}}{B}\right)^{-2.66} \cdot 6 & \text{elsewhere} \end{cases} \tag{2.19}$$

while $C_B = 0.75$ is adopted as the boundary to define the piece-wise.

$R_{awm}(\omega|V,\beta)$ at arbitrary wave heading

In view of the ship motion-induced added resistance $R_{awm}(\omega|V,\beta)$ at an arbitrary wave heading, it is mainly attributed to the long waves (small values of ω) attacking from various angles, and it reaches peak value at the resonance state of the ship motion. From the collected experimental tests, such as el Moctar et al. (2012), Fujii and Takahashi (1975), Journée (2001), Kadomatsu (1988), Liu et al. (2016), Takahashi (1988), and Valanto and Hong (2015), its peak position moves horizontally from the $\lambda/L_{pp}=1$ position to the lower λ/L_{pp} region as the encountered wave angles β increase. It can be readily explained that the encountered frequency $\overline{\omega_\beta}$ decreases from the head wave until the following wave. Thus, a novel encountered frequency correction factor $C_{\overline{\omega}}(\beta)$ was introduced in this study:

$$\overline{\omega_\beta}=\overline{\omega}*C_{\overline{\omega}}(\beta) \tag{2.20}$$

where the suggested values of $C_{\overline{\omega}}(\beta)$ for typical wave angles are listed in Table 2.1, and the $C_{\overline{\omega}}(\beta)$ value of other specific encountered wave angles can be further interpolated.

Table 2.1: Encountered frequency correction factor for typical relative wave angle.

β	0°	30°	45°	60°	90°	120°	135°	150°	180°
$C_{\overline{\omega}}(\beta)$	1	0.925	0.9	0.8	0.75	0.7	0.7	0.7	0.6

The $R_{awm}(\omega|V,\beta)$ peak value shows a declining trend as the relative wave angle β increases. The roll motion dominates the ship motion instead of heave and pitch motions when β is close to 90°. An amplitude adjustment factor $e^{-(\frac{\beta}{\pi})^4\sqrt{F_n}}$ and a compensation factor for roll motion considering the ratio between wavelength λ and ship width B, Froude number F_n and the relative wave angle β are thus tuned in the proposed formula:

$$R_{awm}(\omega|V,\beta)=R_{awm}\cdot e^{-(\frac{\beta}{\pi})^4\sqrt{F_n}}+[\frac{\lambda}{B}\cdot\max(\cos\beta,0.45)]^{-6F_n}\sin\beta \tag{2.21}$$

2.3.3 A correction factor for ship resistance and power

The conventional integration method from ITTC (2014) and ISO (2015) considers wave effect through extensive benchmark study of experimental test results and sea trails. The semi-empirical methods developed by ITTC (2014), ISO (2015) and other scholars can give a fair estimation of the “mean” wave resistance of large ship samples for design purposes. For ship operations, such as voyage optimization and performance monitoring, an individual ship’s performance at a specific operational and environmental condition is more important rather than the “average” wave resistance.

However, the discrepancy between estimations from the linear superposition principle and the observed wave resistance of a ship cannot be avoided for an individual ship. The integration method assumes ship response to the wave is linear. However, a ship response (reflections, motions) is known to be nonlinear, especially in harsher sea states with large H_s. The propulsion efficiency may also be reduced due to the large nonlinear motions in severe wave conditions. Large waves lead a ship to experience unstable surf-riding along the waves as well. These factors contribute to the increase of propulsion power, and the discrepancy has been reported in Dalheim and Steen (2020) and Vitali et al. (2020). These factors are strongly related to the increase of sea states H_s that directly determine the added resistance due to waves R_{AW}. Therefore, a correction factor C_{H_s} is proposed to calibrate the semi-empirical R_{AW} to consider these factors. The total resistance of a ship R_{TOTAL} is estimated by:

$$R_{TOTAL} = R_{CALM} + R_{AA} + R_{AW} \times C_{H_s} \tag{2.22}$$

where the correction factor is wave height-based $C_{H_s} = \sqrt[3.5]{H_s}$ (Lang and Mao, 2021). For more general applications of this correction factor, a comprehensive investigation with extra experimental testing and full-scale measurement should be conducted to configure a flexible formula based on various input parameters.

2.4 Machine learning black-box model for ship propulsion power prediction

The machine learning (data-driven) models for ship propulsion power are used to describe the relationship between measured ship power (output) and all possible influence parameters (input features). The considered input features belonging to the general ship operation and weather conditions are summarized in Table 2.2. The general ship operation parameters contribute to the calm water resistance R_{CALM} and propulsion efficiency η_D. The operation parameters and wave/wind conditions affect the added resistances R_{AW} and R_{AA} (Lang and Mao, 2020).

Let P_D denote the objective target, i.e., the measured propulsion power, and $\underline{\overline{\mathbf{X}}}$ denote the input features, consisting of all the listed attributes in Table 2.2. The objective of the machine learning modeling is to derive the relationship between target/output (power) and input features as:

$$P_D = F(\underline{\overline{\mathbf{X}}}), \quad \underline{\overline{\mathbf{X}}} = [V, T, T_R, \Theta, H_s, T_z, \vartheta, U_{wind}, V_{wind}] \tag{2.23}$$

The workflow of the machine learning modeling is presented in Figure 2.2. First, full-scale measurement data is processed and feature-selected. Then, the processed (clean) data is split into the training and test sets and subsequently standardized.

The cross-validation is implemented to tune hyperparameters to decrease the generalization error, in the form of k-fold for the training set.

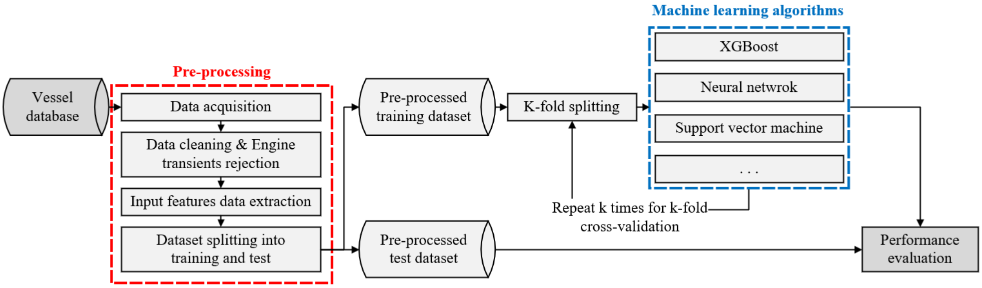

Figure 2.2: Workflow to establish data-driven models for ship propulsion power using different machine learning algorithms.

Table 2.2: Attributes used as inputs/features for machine learning modeling.

Class	Category	Description	Attributes
Input features	Operation	Speed through water	V [knots]
		Mean draft	T [m]
		Trim	T_R [m]
		Heading	Θ [°]
	Metocean	Significant wave height	H_s [m]
		Mean wave period	T_z [s]
		Mean wave direction	ϑ [°]
		Wind speed*	U_{wind} & V_{wind} [m/s]
Output target	Operation	Propulsion power	P_D [kW]

* U component denotes the speed from west to east, and V component denotes the speed from south to north.

Machine learning algorithms

In this study, different machine learning and statistical methods are used to build the ship speed-power performance models.

Linear regression

For a dataset with M statistical samples, the linear regression model can be written as:

$$\hat{P_D}_{(i)} = B_0 + B_1 V_{(i)} + B_2 T_{(i)} \ldots + B_9 V_{wind(i)} = \underline{\overline{\mathbf{X}}}_i^T \boldsymbol{B}, \quad i = 1, \ldots, M \tag{2.24}$$

where $\hat{P_D}_{(i)}$ is the predicted propulsion power, B_0 is the intercept term and $B_1 \sim B_9$ denote the regression coefficients. In the linear regression, the 10-dimensional coefficient vector $\boldsymbol{B}$ is solved by the least squares method, i.e., minimizing the objective function as:

$$Obj = \sum_{i=1}^{M} \left(P_{D(i)} - \hat{P_{D(i)}} \right)^2 \tag{2.25}$$

Polynomial regression

It is ubiquitously understood that a linear model cannot accurately capture the physical relationship of the speed-power performance of a ship, since the propulsion power is roughly proportional to the cube of the speed (Perera and Mo, 2018). The polynomial regression method can be used to consider the nonlinear relations. In this study, a total of nine different input features are considered as the input variables. The third-order multiple polynomial function is defined for the regression as:

$$\begin{aligned} \hat{P_{D(i)}} = {} & B_0 + B_1 V_{(i)} + B_2 T_{(i)} + \cdots + B_9 V_{wind(i)} + B_{11} V_{(i)}^2 + B_{12} V_{(i)} T_{(i)} + \cdots \\ & + B_{99} V_{wind(i)}^2 + B_{111} V_{(i)}^3 + B_{112} V_{(i)}^2 T_{(i)} + B_{113} V_{(i)}^2 T_{R(i)} + \cdots + B_{999} V_{wind(i)}^3 \end{aligned} \tag{2.26}$$

where the objective function and the least squares method are used the same way as the above linear regression (Equation 2.25) to identify the best $\boldsymbol{B}$.

Generalized additive model

The order of nonlinear relationship between output and input features is not easily identifiable, i.e., the determination and interpretation of the order of the polynomial models in Equation 2.26 is difficult. Generalized additive model (GAM) provides an alternative methodology to build a model, without advance knowledge of the order of nonlinear relationship between the output and input features, by adding nonlinear smooth functions (Hastie and Tibshirani, 1986). The standard formulation of the GAM model is written as:

$$\hat{P_{D(i)}} = B_0 + \xi_1 \left(V_{(i)} \right) + \xi_2 \left(T_{(i)} \right) + \cdots + \xi_9 \left(V_{wind(i)} \right), \quad i = 1, \ldots, M \tag{2.27}$$

where ξ_p $(p = 1, \ldots, 9)$ are the smooth functions of different forms. In this study, ξ_p are penalized B-splines to automatically model nonlinear relationships via the least squares method. The objective function is the same as in Equation 2.25.

Artificial neural network

Artificial neural networks are one of the most popular machine learning methods to establish complex data-driven (black-box) models. In a neural network, each neuron is connected to many other neurons, allowing signals to pass through the network from the input layer to the output layer unidirectionally, including through any number of hidden layers in between. Figure 2.3 presents the neural network with one hidden layer to predict the ship propulsion power P_D.

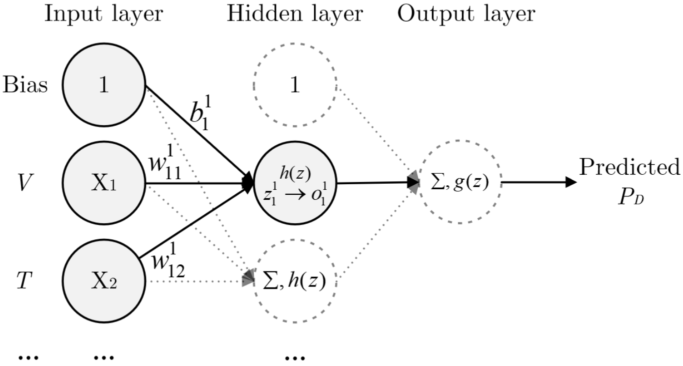

Figure 2.3: An example of a neural network with one hidden layer, predicting ship propulsion power.

The $h(z)$ and $g(z)$ are activation functions for the hidden and output layers, respectively. For regression purposes, identity function is applied for the output $g(z)$. In this study, Rectified Linear Unit (ReLU) function is used for $h(z)$ in hidden layers. The Square Error loss is introduced as the neural network regression objective function, with a L_2 regularization term Υ as:

$$Obj = \frac{1}{2}\sum_{i=1}^{M}\left(P_{D(i)} - \hat{P_{D(i)}}\right)^2 + \frac{\Upsilon}{2}\|\boldsymbol{w}\|^2 \tag{2.28}$$

Adam, a stochastic gradient-based optimizer, is applied to update weights $\boldsymbol{w}$ and minimize the loss (Kingma and Ba, 2014).

Support vector regression

Support vector regression (SVR) uses support vector machines to fit a hyperplane with a margin of tolerance ϵ that minimizes the error between the actual outputs of P_D and the predicted values $\hat{P_D}$ as (Cortes and Vapnik, 1995; Smola and Schölkopf, 2004):

$$\hat{\boldsymbol{P_D}} = \boldsymbol{w}^T\phi(\underline{\overline{\mathbf{X}}}) + b \tag{2.29}$$

where b is the intercept term, and $\phi(\underline{\overline{\mathbf{X}}})$ maps $\underline{\overline{\mathbf{X}}}$ into a higher-dimensional feature space. $\boldsymbol{w}$ is the normal vector, estimated by minimizing the objective function:

$$Obj = C\sum_{i=1}^{M} l_\epsilon\left(P_{D(i)}, \hat{P_{D(i)}}\right) + \frac{1}{2}\|\boldsymbol{w}\|^2 \tag{2.30}$$

where C is the regularization parameter and $\sum_{i=1}^{M} l_\epsilon(P_{D(i)}, \hat{P_{D(i)}})$ consists of the empirical error measured by the ϵ-insensitive loss function. The ϵ-insensitive loss function is defined as:

$$l_\epsilon\left(P_{D(i)}, \hat{P_{D(i)}}\right) = \begin{cases} 0 & \text{for } |P_{D(i)} - \hat{P_{D(i)}}| \leq \epsilon \\ |P_{D(i)} - \hat{P_{D(i)}}| - \epsilon & \text{otherwise} \end{cases} \tag{2.31}$$

It is a convex optimization problem used to get the hyperplane model as in Equation 2.29, which is solved by introducing the Lagrange multipliers α_i and α_i^* and expressed in an explicit form:

$$\hat{\boldsymbol{P_D}} = \sum_{i=1}^{M} (\alpha_i - \alpha_i^*) \cdot \kappa\left(\underline{\mathbf{X}}, \underline{\mathbf{X}}_i\right) + b \tag{2.32}$$

where $\kappa\left(\underline{\mathbf{X}}, \underline{\mathbf{X}}_i\right)$ is a kernel function that linearly separates the training data in a high-dimensional feature space. The Gaussian Radial Basis Function is applied in this study.

XGBoost

The XGBoost algorithm belongs to the ensemble machine learning method, which ensembles multiple modeling results of weak evaluators to obtain better regression or classification performance than a single model. Such as the bagging method that establishes multiple parallel independent weak evaluators at once, there is also a method like boosting that builds weak evaluators one by one to minimize the residual error after multiple iterations. The XGBoost is one of the gradient tree boosting algorithms (Friedman et al., 2000). For XGBoost, each weak evaluator is a tree. Assuming there is a total of K decision trees in the ensemble model, the prediction result on this sample is:

$$\hat{P_{D(i)}} = \sum_{k=1}^{K} f_k\left(\underline{\mathbf{X}}_i\right) \tag{2.33}$$

where f_k represents the k-th decision tree, and $f_k\left(\underline{\mathbf{X}}_i\right) = w_{q\left(\underline{\mathbf{X}}_i\right)}$ is the leaf weight on q-th leaf of that tree. Standard objective functions, such as error rate and mean square error, can only measure the model performance but cannot measure its computational efficiency. The XGBoost algorithm introduces model complexity to measure the efficiency, and the objective function of XGBoost is defined as:

$$Obj = \sum_{i=1}^{M} l\left(P_{D(i)}, \hat{P_{D(i)}}\right) + \sum_{k=1}^{K} \Omega\left(f_k\right) \tag{2.34}$$

where the first term represents the traditional loss function, which measures the difference between the real value $P_{D(i)}$ and the predicted value $\hat{P_{D(i)}}$, usually the root mean square error ($RMSE$). The second term represents the complexity of the model, which measures the tree model complexity from the structure of the tree. The XGBoost algorithm is trained additively; for example, when the new tree is added from the previous iteration, the cost function of the n-th iteration is $l(P_{D}{}_{(i)}^{(n)}, \hat{P_{D}}{}_{(i)}^{(n-1)} + f_n(\overline{\underline{\mathbf{X}}}_i))$, where f_n is the newly added tree at the n-th iteration. Applying Taylor expansion, the simplified objective function at the n-th iteration is:

$$Obj^{(n)} = \sum_{i=1}^{M}[g_i f_n\left(\overline{\underline{\mathbf{X}}}_i\right) + \frac{1}{2} h_i f_n\left(\overline{\underline{\mathbf{X}}}_i\right)^2] + \Omega\left(f_n\right) \tag{2.35}$$

where g_i and h_i are the first and second derivatives of the cost function $l(P_{D}{}_{(i)}^{(n)}, \hat{P_{D}}{}_{(i)}^{(n-1)})$ with respect to $\hat{P_{D}}{}_{(i)}^{(n-1)}$. Suppose a tree contains a total of T leaves, where each leaf index is j, then the weight on this leaf is w_j. Define $I_j = \{i|q(\overline{\underline{\mathbf{X}}}_i) = j\}$ as the instance set of leaf j, the optimal weight w_j^* of leaf j that can minimize the $Obj^{(n)}$ is:

$$w_j^* = -\frac{\sum_{i\in I_j} g_i}{\sum_{i\in I_j} h_i + \Upsilon} \tag{2.36}$$

where Υ is the $L2$ regularization parameter that controls the overfitting. The other features of the XGBoost, such as shrinkage and column subsampling, spit finding algorithms, weighted quantile sketch and system design, are elaborated in Chen and Guestrin, 2016.

2.5 Physics-informed grey-box model for ship speed prediction

The grey-box modeling generally has two types of architecture: serial modeling and parallel modeling (Estrada-Flores et al., 2006). Modeling a process using the serial technique entails configuring two or more models in a series fashion, with at least one WBM and one BBM. Also, the raw input data is pre-processed in the first model and subsequently fed into the following models in succession. The parallel modeling technique integrates the white-box and black-box models in parallel. The parallel architecture entails a WBM and BBM that is trained by reducing the residuals between model outputs and measured data.

In this study, the physics-informed grey-box model is established by the parallel modeling architecture. The architecture of the approach is depicted in Figure 2.4. Configuring two models in parallel, the first of which is a WBM that can derive the ship speed through calm water V_w based on measured propulsion power P_D and ship draft T. Then, the V_w is fed into the machine learning black-box model. The BBM models the speed reduction ΔV between the measured V_g and the white-box output V_w, based on both ship operational data and encountered ocean environmental data. Then the grey-box model can output the speed over ground prediction by subtracting ΔV from V_w.

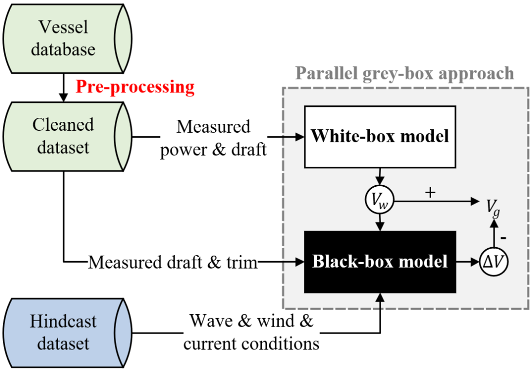

Figure 2.4: The parallel grey-box modeling procedure for ship speed over ground V_g prediction.

The white-box model predicts ship speed V_w (no weather impact) in terms of propulsion power P_D and draft T in calm water conditions. The WBM can be established by three approaches. If the model test measurement is not available, the speed-power relationship can be obtained by the traditional semi-empirical formulas in Sections 2.1 and 2.2.1, which calculate ship calm water resistance and required propulsion power by considering the total propulsion efficiency η_D. Then, the V_w can be calculated if propulsion power P_D and mean draft T are known. However, the semi-empirical method may contain great uncertainties for different individual ships, so the obtained V_w will generally have significant errors.

If sea trials and model tests provide a series of discrete speed-power measurements under different drafts T in calm water conditions, V_w can be estimated by the simplest bilinear interpolation or using a unary cubic equation polynomial regressed based on the “Cubic Rule”:

$$\widehat{P_D} = B_1 {V_w}^3 + B_2 {V_w}^2 + B_3 V_w + B_4 V_w T + B_5 T^2 + B_6 T \tag{2.37}$$

where $B_1 \sim B_6$ denote the regression coefficients. For a given ship speed and draft, the required propulsion power depends on several factors, such as ship types and the new technology/means for reducing ship resistance and boosting ship efficiency. The “Cubic Rule” may be oversimplified and not sufficiently accurate for most ships, and coefficients ranging from 1.45-4.8 instead of 3 (cube) are reported in various studies, such as Adland et al. (2020), Notteboom and Cariou (2009), and Wang and Meng

(2012). Thus, the polynomial regression based on the "Cubic Rule" may not give a reliable estimation of V_w. The simplest bilinear interpolation has large deviations near the upper and lower measurement boundaries.

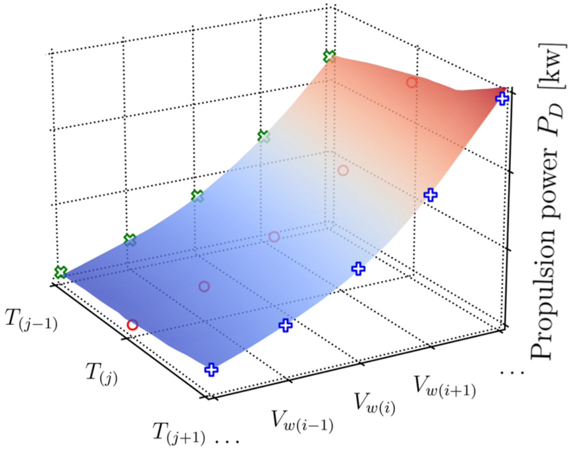

Figure 2.5: The measured speed-power scatters lie on the surface of a PDE solution.

Figure 2.5 shows the three-dimensional speed-power scatters under various drafts from model tests. The scatters form a surface in the space of $P_D - V_w - T$, which represents the solution of a partial differential equation (PDE). If the PDE can be found and solved, the relationship between P_D, V_w and T can be expressed explicitly and a more precise speed through calm water estimation can be obtained.

Raissi et al. (2019) proposed the physics-informed neural networks (PINNs) to handle supervised learning problems while adhering to any given physical rules, as expressed by generic nonlinear PDEs. In this study, the PDE is defined as:

$$A_1 \frac{\partial P_D}{\partial V_w} + A_2 \frac{\partial P_D}{\partial T} + G\left[P_D, V_w, T; \mu\right] = 0, \quad V_w \in \left[V_{wmin}, V_{wmax}\right], \ \ T \in \left[T_{min}, T_{max}\right] \tag{2.38}$$

where $P_D(V_w, T)$ is the propulsion power, V_w represents the speed through calm water, T is the draft and $G\left[P_D, V_w, T; \mu\right]$ is the nonlinear function. The above PDE contains unknown parameters, including A_1, A_2 and μ, which can be determined by applying the partial differential operation on Equation (2.37) with respect to V_w and T, respectively:

$$\frac{\partial P_D}{\partial V_w} = 3B_1 {V_w}^2 + 2B_2 V_w + B_3 + B_4 T \tag{2.39}$$

$$\frac{\partial P_D}{\partial T} = B_4 V_w + 2B_5 T + B_6 \tag{2.40}$$

Rearranging and simplifying Eqs. (2.39) (2.40) results in:

$$\frac{2B_5}{B_4}\frac{\partial P_D}{\partial V_w} - \frac{\partial P_D}{\partial T} - \frac{6B_1B_5}{B_4}{V_w}^2 - \left(\frac{4B_2B_5}{B_4} - B_4\right)V_w - \left(\frac{2B_5}{B_4}B_3 - B_6\right) = 0 \quad (2.41)$$

Comparing Equations (2.41) and (2.38), there exists the following relationship:

$$\begin{aligned} & A_1 = \frac{2B_5}{B_4}, A_2 = -1, \\ & N\left[P_D, V_w, T; \mu\right] = -\left(\frac{6B_1B_5}{B_4}{V_w}^2 + \left(\frac{4B_2B_5}{B_4} - B_4\right)V_w + \left(\frac{2B_5}{B_4}B_3 - B_6\right)\right) \end{aligned} \quad (2.42)$$

The PINNs aim to approximate the V_w through the artificial neural networks. For these purposes, a PINNs f is defined to represent P_D. Thus, Equation (2.38) is reformed to:

$$g{:=}A_1\frac{\partial f}{\partial V_w} + A_2\frac{\partial f}{\partial T} + \ G\left[f, V_w, T; \mu\right] \ , \quad V_w \in \left[V_{wmin}, V_{wmax}\right], \ \ T \in \left[T_{min}, T_{max}\right] \quad (2.43)$$

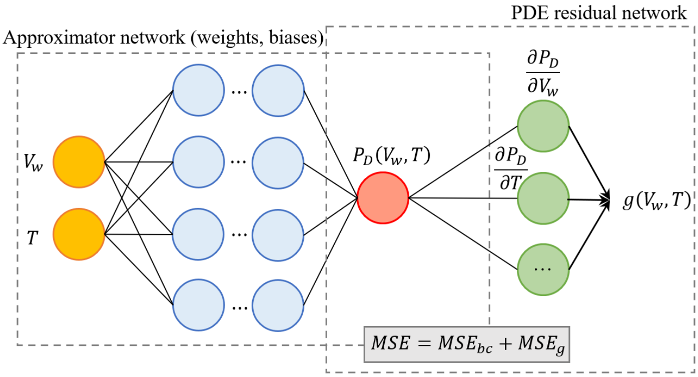

Figure 2.6: Schematic representation of the applied PINN for speed-power baseline modeling.

Figure 2.6 shows the described PINNs that consist of two interconnected networks. The approximator network approximates the ship propulsion power given the ship speed through water V_w and the draft T. The weights and biases of the approximator network are trainable. The left portion of Figure 2.6 calculates the residuals (mean squared error) appearing in the governing equations and the boundary conditions introduced by the approximator network, which are represented as MSE_g and MSE_{bc}. The two networks work together to minimize the total residuals MSE.

Since the propulsion power P_D is now represented by neural networks, the partial differentiation $\frac{\partial P_D}{\partial V_w}$ and $\frac{\partial P_D}{\partial T}$ can be obtained using automatic differentiation (AD), i.e., $\frac{\partial f}{\partial V_w}$ and $\frac{\partial f}{\partial T}$, respectively. To satisfy Equation (2.38), the neural networks f need to be trained to make $g \rightarrow 0$. To this end, the mean squared error (MSE) loss, MSE_g, is defined as:

$$MSE_g = \frac{1}{N}\sum_{i=1}^{N}\left|g\left(V_{w(i)}, T_{(i)}\right)\right|^2 \tag{2.44}$$

where $\left(V_{w(i)}, T_{(i)}\right)$ are sample data, and N is the sample size for training. The boundary conditions should be fulfilled as well. If $V_{w\,bc(i)}$, $T_{bc(i)}$ and $P_{D\,bc(i)}$ are defined as boundary values, the loss on the boundary conditions can be expressed as:

$$MSE_{bc} = \frac{1}{N_{bc}}\sum_{i=1}^{N_{bc}}\left|P_D\left(V_{w\,bc(i)},\ \ T_{bc(i)}\right) - P_{D\,bc(i)}\right|^2 \tag{2.45}$$

Thus, the total loss is defined as:

$$MSE = MSE_{bc} + MSE_g \tag{2.46}$$

The physics-informed neural networks is trained to output the propulsion power, $P_D(V_w, T)$, given the speed through water, V_w, and draft, T, w.r.t. the baseline.

It is not like the traditional PINNs whose PDE is given. The parameters in the govern Equation (2.38) need to be initially determined. To find the appropriate parameters, the coefficient vector $\boldsymbol{B}$ is randomly initialized and a candidate PDE is generated. The sample points $\left(V_{w(i)}, T_{(i)}\right)$ are obtained from Equation (2.37). The PINNs can be trained, and the loss MSE is evaluated. Then the generic algorithm is implemented to update the coefficient vector $\boldsymbol{B}$ and to minimize the MSE. Repeating these steps, the governing Equation (2.38) can be determined when the loss is smaller than a threshold.

A significant difference between the proposed PINNs and the polynomial regression is that the polynomial regression aims to minimize the error of propulsion power "strongly", meaning the target is limited to compare specific values of P_D and $\widehat{P_D}$ while the gradient information is completely ignored. However, the proposed PINNs aims to evaluate both the P_D and the $\frac{\partial P_D}{\partial V_w}$ and $\frac{\partial P_D}{\partial T}$ together. The PINNs approximates the solution surface of P_D in the space of $P_D - V_w - T$ in a "weak" fashion. Moreover, the boundary constraints, MSE_{bc}, can further "drag" the solution closer to the measurements and dramatically improve the accuracy.

Once the PINNs is established and solved, the expected speed through water $\widehat{V_w}$ can be inversely obtained from another neural network, h, whose inputs are $P_D(V_w, T)$

and T, i.e., $\widehat{V_w} = h(P_D(V_w, T), T)$, with $h = g^{-1}$

Table 2.3: Input features considered for the speed reduction ΔV prediction modeling.

Category	Description	Attributes
Operation	Expected speed in calm water	$\widehat{V_w}$ [knots]
	Mean draft	T [m]
	Trim	T_R [m]
Wave condition	Significant wave height	H_s [m]
	Mean wave period	T_z [s]
	Relative wave direction	β [°]
Wind condition	Relative wind speed	V_{WR} [m/s]
	Relative wind direction	φ_{WR} [°]
Current condition	Relative current speed	V_{CR} [m/s]
	Relative current direction	φ_{CR} [°]

Then the XGBoost algorithm in Section 2.4 is applied to establish the BBM that describes the relationship between speed reduction ΔV and the obtained speed through calm water $\widehat{V_w}$. The input features are listed in Table 2.3.

CHAPTER 3

Method for the ship fatigue assessment

The ship fatigue problem is generally recognized as a high-cycle fatigue accumulation process, i.e., the so-called S-N approach (IACS, 2006). The fatigue damage is estimated by the linear Palmgren-Miner's rule based on a specific S-N curve (DNV GL, 2018) as Equation (3.1):

$$d\left(t\right) = \sum_{i} \frac{n_i S_i^m}{\alpha} \tag{3.1}$$

where α and m are the S-N curve parameters, and are dependant on structural materials, geometries, working environments and method of fabrication (welding details). t is the length of duration for a sea state. In this study, the Ib S-N curve with $\alpha = 10^{12.76}$ and $m = 3$ (DNV GL, 2018) is assumed in the following analysis. The n_i is the number of stress cycle ranges S_i, which can be estimated by the rainflow counting method if structural stress signals are available. The non-recursive definition rainflow counting method, given by Rychlik (1987), is used in this study.

However, ship stress signals are rarely available for such purposes, since only a small number of ships have been employed with sensors (and in a short measurement campaign) to measure structural strain/stress. As cyclic stresses leading to ship fatigue are mainly caused by waves, an alternative approach for a direct fatigue calculation can be used (Lang et al., 2020). The stress response is estimated in the frequency domain by Response Amplitude Operators (RAOs) combined with encountered wave conditions, as depicted in Figure 3.1.

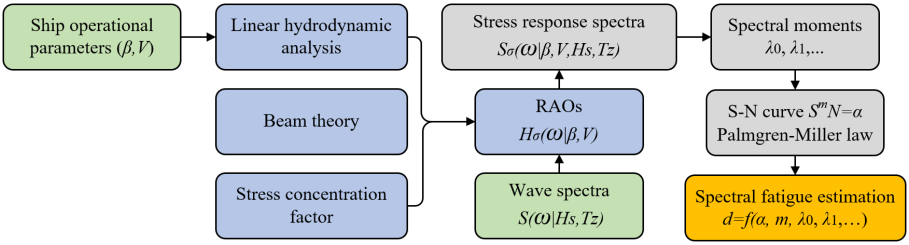

Figure 3.1: Workflow of the conventional ship fatigue damage calculation method by spectral fatigue assessment.

3.1 Spectral moments and narrow-band fatigue approximation

The RAOs are typically obtained by assuming the rigid body motions of a ship for wave loading analysis and the beam theory for stress analysis. Wave loadings applied to ships are estimated by the potential theory for ship fatigue assessment and described by a damped spring-mass system. Different axial force and bending moment RAOs at any given cross sections are estimated regarding various wave frequencies ω under a given ship speed V and relative wave heading β, including the longitudinal force $F_a(\omega|V,\beta)$, the vertical bending moment $M_v(\omega|V,\beta)$, the horizontal bending moment $M_h(\omega|V,\beta)$ and torsional moment $M_t(\omega|V,\beta)$. Then, for any structural details located at the given cross section, its nominal structural stress RAOs can be calculated by the beam theory as:

$$H_\sigma(\omega|V,\beta) = \frac{F_a\left(\omega|V,\beta\right)}{A_r} + \frac{M_v\left(\omega|V,\beta\right)}{I_v}\Delta z + \frac{M_h\left(\omega|V,\beta\right)}{I_h}\Delta y + \sigma_w(\omega|V,\beta) \quad (3.2)$$

where A_r, I_v and I_h define the cross-sectional area and area moments of inertia; Δz and Δy are the distances between the detail and neutral axes, respectively, and σ_w is the warping stress due to the torsional moment M_t. Normally, if the hot-spot or nominal stresses are used in the S-N method, the stress concentration factor at the location of interest should be obtained.

The frequency domain RAOs of structural stress can be easily employed to obtain the short-term stress response spectra of a ship. For ship fatigue life prediction, the long-term wave conditions are assumed to comprise a series of short-term stationary sea/wave states. Each stationary sea state can last for 30 minutes to 6 hours. The sea states are described by their statistical property, such as the significant wave height H_s, the wave period T_z, the wave spectrum and occasionally the spreading angles. Different wave spectra have been developed for such purposes. In this study, the ISSC wave spectrum (Tucker and Pitt, 1990) is used and defined as:

$$S\left(\omega \mid H_s,\ T_z\right) = \frac{4\pi^3 H_s^2}{T_z^4 \omega^5} \exp\left[-\frac{1}{\pi}\left(\frac{\omega T_z}{2\pi}\right)^{-4}\right] \tag{3.3}$$

Finally, the ship stress response spectra can be estimated by multiplying the square of stress RAOs with the encountered wave spectrum. The stress spectral moments λ_n, $n = 0, 1, 2, \ldots$, are further estimated calculated by:

$$\lambda_n\left(V, \beta, H_s, T_z\right) = \int_0^\infty \left|\omega + \frac{\omega^2 V \cos\beta}{g}\right|^n H_\sigma^2\left(\omega \mid V, \beta\right) S\left(\omega | H_s, T_z\right) d\omega \tag{3.4}$$

For a stationary sea state of time interval t, if the stress signals are assumed to be a narrow-band Gaussian process, its stress ranges follow the Rayleigh distribution. Then, fatigue damage accumulated during this period can be approximated by the so-called narrow-band approximation as:

$$d^{nb} = \frac{t f_z}{\alpha} 2^{\frac{3m}{2}} \Gamma(1 + \frac{m}{2}) \lambda_0^{m/2}, f_z = \frac{1}{2\pi}\sqrt{\frac{\lambda_2}{\lambda_0}} \tag{3.5}$$

where f_z is the frequency of zero-crossing, including the frequency of stress cycles, and $\Gamma()$ is the gamma function. The only variables in the above narrow-band approximation are the spectral moments, which can be easily estimated by Equation (3.4). However, it should be noted that the stress signals are seldom purely narrow-band processes. In addition, even though the motion and stress response are not Gaussian processes when ships sail at relatively high sea states, the Gaussian response assumption is commonly accepted for ship fatigue assessment (DNV GL, 2018). Therefore, different correction methods/coefficients are proposed to increase the accuracy of fatigue damage estimation using Equation (3.5).

3.2 Bandwidth correction

In this study, various spectral moments correction methods are implemented to investigate their accuracy for fatigue damage assessment, with an additional objective to identify all useful features of moments for machine learning based fatigue estimation. The first attempt is to introduce the bandwidth parameter to correct the narrow-band approximation. For example, Tovo (2002) proposed the model as:

$$d^{tv} = (\rho + (1 - \rho)\varepsilon_2^{m-1}) d^{nb}, \varepsilon_k = \frac{\lambda_k}{\sqrt{\lambda_0 \lambda_{2k}}} \tag{3.6}$$

where ε_k is defined as the bandwidth parameter, $\rho = \min(\frac{\varepsilon_1 - \varepsilon_2}{1 - \varepsilon_1}, 1)$, where the damage approaches to narrow-band approximation when ρ goes to 1. Another improved version of this method proposed by Benasciutti and Tovo (2007) is applied in this study, the fatigue damage d^{bt} is calculated with:

$$\rho = (\varepsilon_1 - \varepsilon_2)\frac{1.112e^{2.11\varepsilon_2}\left(1 - \varepsilon_1 - \varepsilon_2 + \varepsilon_1\varepsilon_2\right) + (\varepsilon_1 - \varepsilon_2)}{(\varepsilon_2 - 1)^2} \tag{3.7}$$

An alternative approximation was proposed by Wirsching and Light (1980) using only the bandwidth parameter ε_2, but regarding various S-N curve slope parameter m as follows:

$$d^{wl} = (a(m) + (1 - a(m)(1 - \sqrt{1 - \varepsilon_2^2})^{b(m)})d^{nb} \tag{3.8}$$

where $a\left(m\right) = 0.926 - 0.033m$ and $b\left(m\right) = 1.587m - 2.323$.

In this study, the correction methods that split the stress response spectra are not discussed, thus, the spectral methods will only investigate wave loads induced fatigue.

3.3 Machine learning method for ship fatigue assessment

The machine learning model is established to describe the fatigue damage of a ship accumulated during a sea state in terms of various input features. In this thesis, the model is based on three different types of input features (denoted as $\underline{\overline{\mathbf{X}}}$), and the proposed architecture for ship fatigue assessment is depicted in Figure 3.2. The prediction target is the observed ship fatigue damage in the assumed stationary 30-minutes sea states, i.e., $\boldsymbol{D} = [d_1, d_2 \ldots d_n]$, where n is the sample size. The observed fatigue damage is estimated by the rainflow counting method based on every 30-minute stress signal. The XGBoost algorithm in Section 2.4 is applied for the BBM establishment for fatigue assessment.

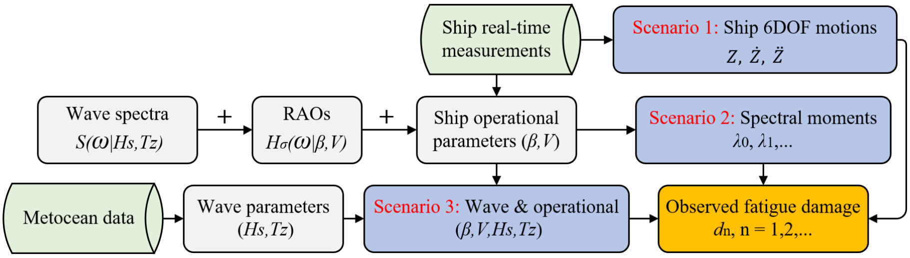

Figure 3.2: The flowchart of the proposed machine learning architecture for ship fatigue assessment.

If the 6 Degrees of Freedom (DOF) motions of a ship is known, then the first scenario is to use the statistics of ship motions as as input features, i.e., $\overline{\underline{\mathbf{X}}} = \left[m_1(\boldsymbol{Z}), m_1(\dot{\boldsymbol{Z}}), m_1(\ddot{\boldsymbol{Z}}), ...\right]$, to build a model to predict the ship fatigue. The mean value m_1, standard deviation m_2, skewness m_3 and kurtosis m_4 of the measured motions are extracted from each 30-minute stationary sea state. $\boldsymbol{Z}$ denotes ship motions, $\dot{\boldsymbol{Z}}$ is motions velocity, and $\ddot{\boldsymbol{Z}}$ is motions acceleration. Then the Pearson correlation coefficients of different statistics relative to rainflow counting fatigue damage are calculated and compared. The statistics with high correlation coefficients are applied as the input features for the motion-based machine learning model.

However, when predicting the fatigue of the ship for a period of time in the future or the entire service life, there is no data available on the ship's strain/stress and motions. Therefore, it is necessary to establish a black-box model of fatigue assessment based on the ship's operational profiles and different ocean conditions. The second scenario is as shown in Figure 3.2, using various orders of stress spectral moments from numerical simulations to build the model. The stress spectral moments λ_0 to λ_4 used in narrow-band fatigue assessment methods are applied as the input features in the second scenario $\overline{\underline{\mathbf{X}}} = [\lambda_0, \lambda_1, \lambda_2, \lambda_3, \lambda_4]$. In the third scenario, the fatigue damage is estimated directly based on ship operational profiles and wave condition, since the ship motions and spectral moments are highly related to the sea state and sailing speed. Thus, the input features for the third scenario are $\overline{\underline{\mathbf{X}}} = [H_s, T_z, \beta, V]$.

CHAPTER 4

Case study ships and their measurement data

In this thesis, the proposed semi-empirical WBMs are verified with both experimental test data and full-scale measurement data. The machine learning BBMs and physics-informed GBMs are trained and demonstrated by the full-scale measurement data. In the following sections, various types of data are briefly presented. Since the full-scale measurement data often contain a degree of measurement noise, the data pre-processing framework used in this thesis is also presented.

4.1 Experimental tests on regular waves

The proposed semi-empirical formulas for estimating the added resistance of a ship due to waves, as presented in Section 2, are developed using experimental tests on regular waves. Several model tests are available in the literature and have been collected for this study, i.e., S175 container (Fujii and Takahashi, 1975; Takahashi, 1988), KVLCC2 tanker (Guo and Steen, 2011; Sadat-Hosseini et al., 2013), DTC container (el Moctar et al., 2012), HSVA cruise (Valanto and Hong, 2015), S.A. Van Der Stel (Alexandersson, 2009), a bulk carrier (Kadomatsu, 1988) and Series 60 models with five various block coefficients C_B (Strom-Tejsen et al., 1973). The required parameters for those ships are listed in Table 4.1. For the development and verification of the semi-empirical models on regular head waves, the experimental results from the 11 aforementioned ships are used in Paper I. Five ships (the S175 container ship, the DTC container ship, the HSVA cruise ship, the S.A. Van Der Stel and the bulk carrier) are selected to verify the semi-empirical model for added resistance due to arbitrary wave heading angles. Table 4.2 presents the considered relative wave angles β and Froude numbers F_n of the experimental tests in Paper II.

Table 4.1: Main characteristics of the studied ships in the experiments conducted in available publications.

Ship type	L_{pp} [m]	B [m]	T [m]	C_B [-]	L_E [m]	k_{yy} [-]
S175 container	175	25.4	9.5	0.572	59.05	0.24
KVLCC2 tanker	320	58	20.8	0.8098	60	0.25
DTC container	355	51	14.5	0.661	112	0.27
HSVA cruise	220.27	32.2	7.2	0.654	72.42	0.263
S.A. Van Der Stel	152.5	22.8	9.14	0.563	61	0.22
Bulk carrier	285	50	18.5	0.829	51	0.25
Series 60 model 4210	121.96	16.254	6.492	0.6	52	0.25
Series 60 model 4211	121.96	16.816	6.73	0.65	46.522	0.25
Series 60 model 4212	121.96	17.42	6.97	0.7	38.606	0.25
Series 60 model 4213	121.96	18.062	7.22	0.75	30.48	0.25
Series 60 model 4214	121.96	18.757	7.495	0.8	22.8	0.25

Table 4.2: Considered relative wave angles and Froude numbers for arbitrary wave heading model tests.

Ship type	Relative wave angle β	Froude number F_n
S175 container	[0°, 30°, 60°, 90°, 120°, 150°, 180°]	0.250
DTC container	[0°, 30°, 60°, 120°, 150°, 180°]	0.052
HSVA cruise	[0°, 30°, 60°, 90°, 120°, 150°, 180°]	0.232
S.A. Van Der Stel	180°	[0.150, 0.200, 0.250, 0.300]
Bulk carrier	[0°, 45°, 90°, 135°, 180°]	0.100

4.2 Full-scale case study ships

A merchant chemical tanker, a PCTC sailing worldwide and a 2800TEU container ship sailing in the North Atlantic are employed as the case study vessels. The full-scale measurement data collected onboard these vessels are used to establish and verify the proposed performance models. The main characteristics of these studied ships are listed in Table 4.3. These parameters are applied as inputs in the semi-empirical WBMs. The three ships were instrumented with various sensors to collect large amounts of ship navigation- and performance-related data, up to a gigabyte per day. The parameters of the full-scale measurement data from the chemical tanker and PCTC are similar. In the full-scale measurements, the shaft torque, RPM and propulsion power were recorded by sensors installed in marine engines. The ship draft was measured at the stern and stem. A GPS tracker stored the longitude, latitude, speed over ground and ship heading at the wheelhouse of each ship. The measurements were collected with a frequency of 1 Hz.

Table 4.3: Main characteristics of the studied PCTC, container ship and chemical tanker used for full-scale measurements.

Parameter	Symbol	Unit	PCTC	Container	Chemical tanker
Length between perpendicular	L_{pp}	m	190	232	174.8
Breadth molded	B	m	32.26	32.2	32.2
Designed draft	T	m	9.5	10.78	10.98
Block coefficient	C_B	-	0.6	0.54	0.8005
Longitudinal radius of gyration	k_{yy}	-	0.26	0.26	0.25
Length of entrance	L_E	m	62	40	38.5
Transverse projected area	A_{XV}	m^2	985	750	400
Deadweight	DWT	tons	28126	40900	46067
Maximum continuous rating	P_c	kW	14700	21000	8200

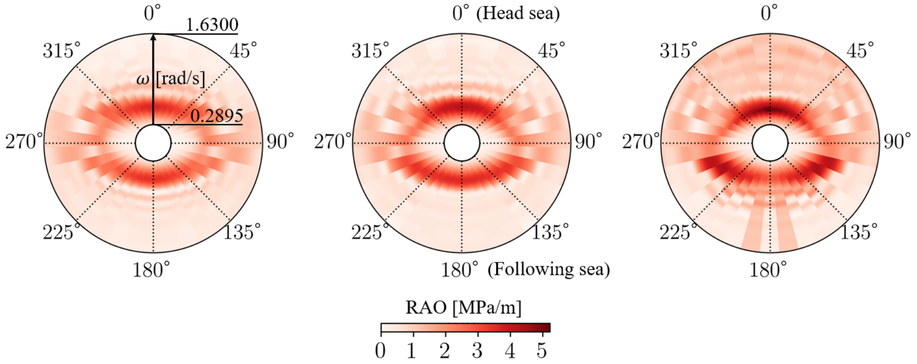

Figure 4.1: The vertical bending moment induced stresses RAOs polar heatmap of the amidship deck longitudinal stiffener for the container vessel case study at speed through water $V = 1.94$ knots (1 m/s, left plot), $V = 13.61$ knots (7 m/s, middle plot), and $V = 23.32$ knots (12 m/s, right plot). The ω ranged from 0.2895-1.63, representing the angular frequency of regular waves. 0° represents head sea, and 180° is following sea.

Except for the similar operational profiles measurement, the onboard-installed hull monitoring system also recorded real-time data of structural strain/stress and ship motions for the container ship. In order to separate the stresses caused by torsion and bending moments, the strain sensors were arranged at different locations of the same cross-section. The sensors were placed on the stiffener web and measure the nominal longitudinal strain of both the port and starboard sides. In this study, only the vertical bending-induced strain/stress at the middle section is applied for the fatigue analysis, thus, the considered strain/stress values are the average of strain/stress measured on the port and starboard sides. A Motion Response Unit (MRU) was installed at the central line and measured the 6DOF motions of the container vessel. The MRU measurements include 16 variables, including motions $\boldsymbol{Z} = [z_2, z_3, z_4, z_5, z_6]$, motions velocity $\dot{\boldsymbol{Z}} = [\dot{z}_2, \dot{z}_3, \dot{z}_4, \dot{z}_5, \dot{z}_6]$ and motions acceleration $\ddot{\boldsymbol{Z}} = [\ddot{z}_1, \ddot{z}_2, \ddot{z}_3, \ddot{z}_4, \ddot{z}_5, \ddot{z}_6]$. $z_1$to z_6 denote surge, heave, sway, roll, yaw and pitch, respectively. The measurement frequency of strain/stress and ship motions is 25 Hz, and the frequency for other operational parameters is 1 Hz.

For the conventional ship fatigue damage calculation by spectral fatigue assessment, the vertical bending moment RAOs are obtained by evaluating wave bending moments using a hydrodynamic analysis based on a 2-D potential theory code WaveShip (Mao et al., 2009, 2010). To determine the wave loads applied to the hull of this container ship, the fully-loaded condition is considered in the hydrodynamic analysis. The RAOs of the local stresses are computed by multiplying the girder stresses by a stress concentration factor (SCF), which is 2 for this container vessel. The RAOs of structural stress in the upper deck area (midship section) are applied. Figure 4.1 presents the vertical bending moment RAOs polar heatmap for three different speeds, i.e., V = 1.94 knots (1 m/s, left plot), V = 13.61 knots (7 m/s, middle plot), and V = 23.32 knots (12 m/s, right plot).

The angle of the polar diagram is the relative wave angle β, and the radius is the wave frequency ω ranging from 0.2895-1.63 rad/s. The color of the heatmap represents the value of the RAOs. The darker the color, the larger the value of $H_\sigma(\omega|V, \beta)$ and the larger the stress response in the same H_s and T_z conditions. As Figure 4.1 shows, it is obvious that the RAOs are sensitive to the variation of the relative wave angle β and the speed through water V. As the speed V increases, the value of $H_\sigma(\omega|V, \beta)$ increases. Under the same speed and wave conditions, the largest stress response exists at the head sea. For the beam sea $\beta \approx 90^{\circ}$, the stresses induced by waves are relatively smaller.

Several typical sailing routes recorded during the full-scale measurement campaign are illustrated in Figure 4.2. Furthermore, the ship baselines used to describe the calm water resistances obtained from model tests and sea trials are provided by the ship operators for this study. The coefficient of wind resistance for the PCTC is obtained from wind tunnel tests. For the chemical tanker and the container ship, the wind resistance R_{AA} is calculated according to the semi-empirical models in ISO (2015). The total propulsive efficiency η_D is extracted from the open water tests.

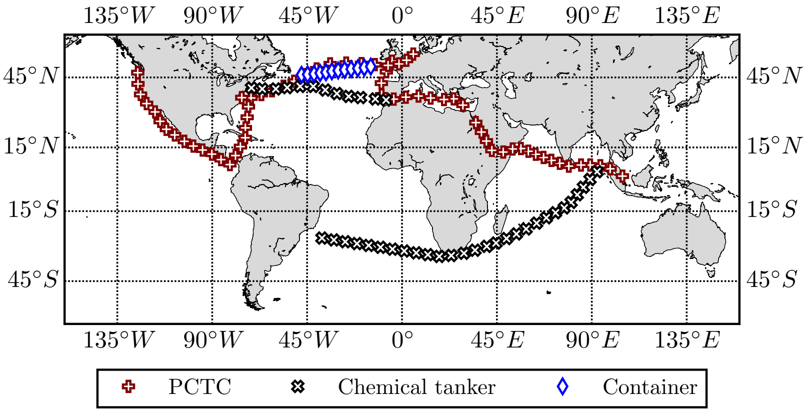

Figure 4.2: Typical routes of the three studied ships during their measurement campaigns. The PCTC and chemical tanker were sailing worldwide, while the container ship was sailing in the North Atlantic.

4.3 Metocean data

Table 4.4: Sources and resolutions of the metocean parameters used in this study.

Parameter	Source	Spatial resolution	Temporal resolution
H_s T_z ϑ U_{wind} V_{wind}	ERA5	0.5 × 0.5 degree	hourly
$U_{current}$ $V_{current}$	CMEMS	0.083 × 0.083 degree	daily

For the development of ship performance models, it is crucial to access reliable meteorological and oceanographic (metocean) data. The metocean data includes parameters for wind, waves and currents. The actual historical data from different hindcast data sources are used in this study. The mean wave direction ϑ, mean wave period T_z, significant wave height H_s, wind speed U_{wind} and V_{wind} are extracted from the reanalysis dataset ERA5 to construct the encountered sea states along sailing routes (Copernicus, 2019). For the current speed $U_{current}$ and $V_{current}$, the CMEMS (2019) observation data are applied. For both wind and currents, the U component denotes the speed from west to east, and the V component denotes the speed from south to north. The true velocity and direction are the vectorial summation of these two components. The spatial and temporal resolutions of the metocean parameters used in this study are listed in Table 4.4. The bathymetry information is accessed from GEBCO (2019).

4.4 Full-scale measurements data processing

4.4.1 White-box models for speed-power performance

Full-scale measurement data are used to verify the semi-empirical speed-power models for speed loss prediction. To predict the speed loss of a ship, the power setting should be first identified from the full-scale measurements. In this study, sailing waypoints from engine power settings close to 9000 kW (64% MCR) for the PCTC, 17000 kW (80% MCR) for the container and 5800 kW (70% MCR) for the chemical tanker are selected for the verification analysis.

The Kwon (2008) model that is commonly used in ship voyage optimization systems is compared with the semi-empirical speed-power models developed in this study. It utilizes Beaufort numbers as inputs to predict ship speed loss. Therefore, for the full-scale measurements of the three case study ships, the waypoints from the selected engine power settings are divided into various Beaufort number groups, i.e., BN-3, BN-4, BN-5, BN-6 and BN-7, based on the encountered significant wave height H_s. The interval of H_s for determining the Beaufort numbers of encountered metocean environments is determined according to Table 4.5, which uses criteria from the definitions in ISO (2015).

The relative wave heading angles β of approximately 0°, 30°, 60°, 90°, 120°, 150° and 180° are selected as the reference wave headings for comparison purposes. To increase the sample size of sailing conditions located at each wave heading span, the specific angles β are collected in the range of $\pm 5°$; for instance, $85° \sim 95°$ is represented as 90°. Notably, the measurement data with relative wave angles between $0° \sim 10°$ and $170° \sim 180°$ are considered head seas and following seas, respectively. Figure 4.3 presents the heatmaps of the measured speed through water versus the encountered wave heading angles, and these help with visualizing how V changes as β increases from a head to a following sea. All sailing speeds of a ship under each Beaufort scale and within each specific relative wave angle span are averaged to represent the measured (mean) speed for that sea condition. The red circle markers are the obtained averaged speeds used for the verification process. The full-scale measured V is significantly scattered along the averaged lines in the heatmaps.

Table 4.5: The probable span of H_s for the Beaufort scales considered in the verification dataset separation process.

Beaufort number	Significant wave height	Beaufort number	Significant wave height
BN-3	0.3 ~ 1.0 m	BN-4	1.0 ~ 1.5 m
BN-5	1.5 ~ 2.5 m	BN-6	2.5 ~ 4.0 m
BN-7	4.0 ~ 5.5 m		

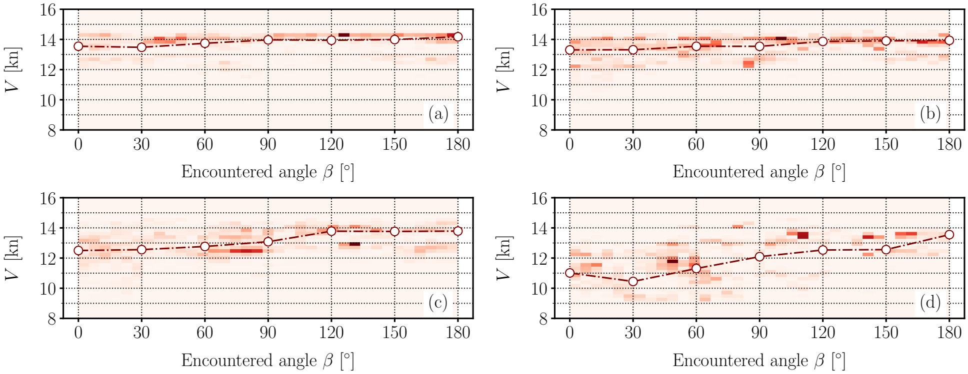

Figure 4.3: Heatmap and average measured speed through water V regarding wave heading angle β of the studied chemical tanker for (a) BN-3, (b) BN-4, (a) BN-5, and (b) BN-6.

For semi-empirical model verification in head waves, the PCTC and the chemical tanker are employed as the case study ships. The studied power settings are approximately 8800 kW (60% MCR) for the PCTC and 4300 kW (52% MCR) for the chemical tanker.

4.4.2 Black-box and grey-box models for speed-power performance

Approximately 5-year (2014-2018) measurement data from the chemical tanker were collected onboard and used in this study. Due to various measurement noise scenarios, such as sensor delays, server latency and other interruptions, the first step is to detect data discontinuities in time and synchronize them. Next, the raw data is labeled with different operation statuses, including anchor/drifting, at berth and sea passage in open sea areas. Since this study focuses on the speed-power model of a ship under navigation conditions, only the sea passage data is extracted and applied for further cleaning/processing. Obvious outliers (noised data samples) are deleted based on physical constraints, such as the measured propulsion power needing to be positive and less than the maximum engine power, the measured speeds cannot exceed the maximum ship speed, and other scenarios. Dynamic ship maneuvering conditions in the sea passage, such as voluntary acceleration and deceleration, sharp power increase due to engine soot-blowing operations and sharp course changes are also removed.

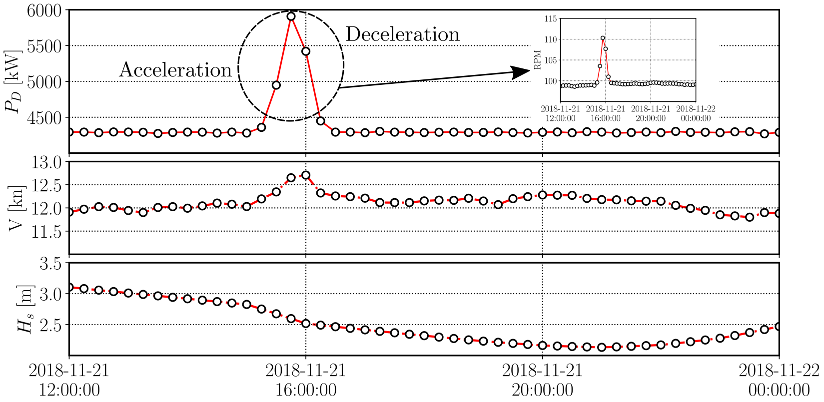

Figure 4.4: A sharp propulsion power P_D change during 12 hours sailing within a sea passage for the chemical tanker case study.

Figure 4.4 presents a typical sharp power increase during 12 hours of a sea passage. It occurred at 2018-11-21 15:00:00, when the measured power was increased rapidly from 4300 kW to 6000 kW and declined back within one hour. As Figure 4.4 shows, the speed through water V increased more than 0.5 knots and the encountered significant wave height H_s was decreasing. The small window in Figure 4.4 describes the measured RPM for the half-day navigation. Obviously, the ship operator adjusted the propeller rotation rates to accelerate and decelerate. This maneuvering phenomenon was filtered from the modeling dataset by analyzing the RPM change rate (first derivative), where the adjacent RPM cannot exceed a difference of 1 rev/min. The sharp course change is detected by the criteria of a five-degree change between adjacent measurements.

The comparison of the raw data and processed data used for machine learning is illustrated in Figure 4.5. There are many lower-speed and lower-power data close to zero due to the anchor and at berth conditions in the raw measurements, represented as grey dots. For the sea passage data, these smaller values have been removed, but there are remain many data samples with sudden changes in P_D and V for a short period caused by acceleration, deceleration and other maneuvering states. After the data processing/cleaning, the propulsion power P_D did not change dramatically with a stable value for a short span. This means that the maneuverability-related voluntary power changes have been filtered from the dataset. However, there remain some rapid decreases in ship speed, which is the involuntary speed loss caused by the encountered severe weather condition with large values of significant wave height H_s. For instance, at the end of 2017, the ship speed dropped to three knots when H_s was over 7 meters although with a stable propulsion power.

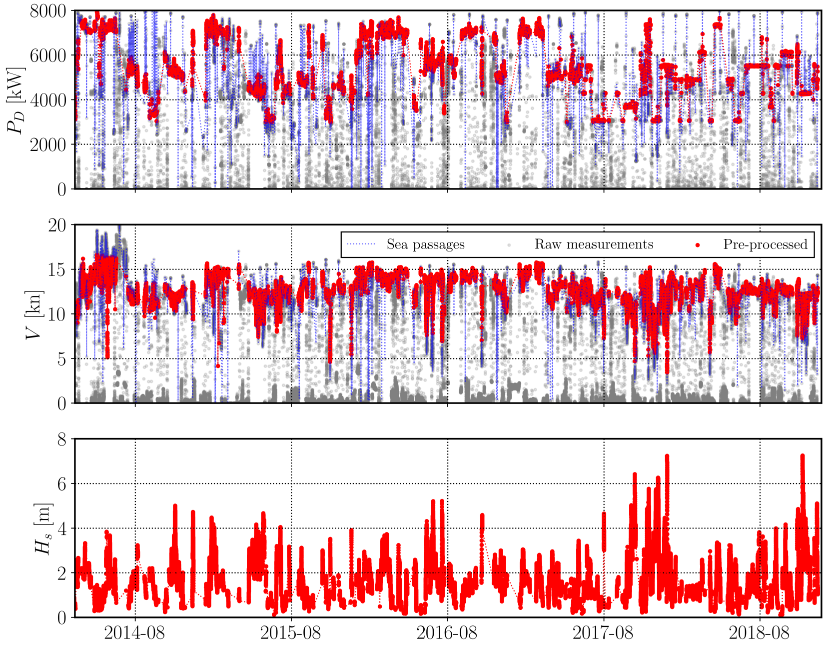

Figure 4.5: The propulsion power P_D, ship speed through water V and significant wave height H_s for raw measurements, sea passage condition and after pre-processing for the five-year sailing duration of the chemical tanker.

The raw measurements record about 165,000 data points, while, for the sea passage condition, the data volume decreases to approximately 85,000. Finally, a total of 63,093 data remains after the cleaning process. The frequency distribution histograms of the propulsion power P_D, ship speed through water V and significant wave height H_s in sea passage conditions from the raw measurements are compared with that from the pre-processed data in Figure 4.6. As shown in Figure 4.6, a large amount of the P_D and V of the raw measurements is concentrated around zero, indicating measurements during anchor, tug and at berth. The pre-processed dataset in Figure 5 is applied for machine learning analysis, with a wide distribution of feature ranges, i.e., P_D around 3000-8000 kW, V between 4-17 knots (major in $10 \sim 15$ knots) and H_s in the range of 0-7 meters (major in $0 \sim 3$ meters).

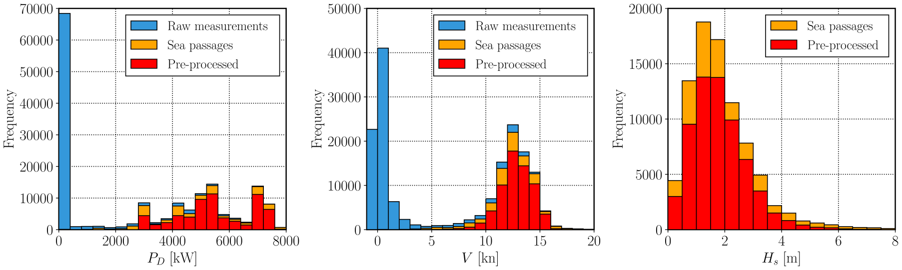

Figure 4.6: The frequency distribution histograms of P_D, V and H_s during sea passage conditions from the raw measurements and that from the processed data collected from the five-year sailing duration of the chemical tanker.

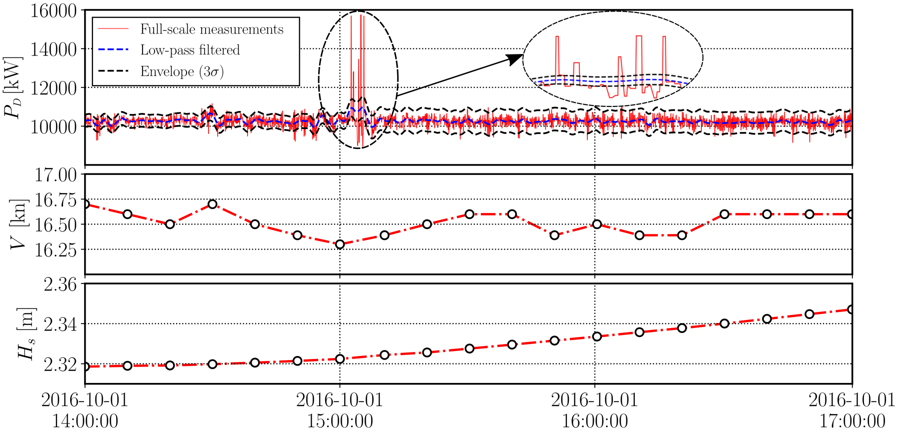

Figure 4.7: Extracted measured propulsion power P_D with an envelope of $\pm 3\sigma$ relative to the low-pass filter for spike value detection for the PCTC case study and the corresponding ship speed through water V as well as significant wave height H_s.

The data for the PCTC ship was collected for three months (June 30, 2016 to October 8, 2016). In addition to the same data processing procedure as for the chemical tanker, there are other nonphysical phenomena leading to spikes in the high-frequency raw data of the ship. These spikes are sudden changes that significantly deviate from their adjacent data samples. They can cause problems during the model training process, leading to an incorrect description of the model. Therefore, those spikes are detected and excluded by a low-pass filter and a running standard deviation. For instance, some spikes were observed in the measured propulsion power. This kind of power increase is a standard soot-blowing procedure conducted to clean the turbocharger during operations.

See Figure 4.7 for visualization of a one-period propulsion power spike value detection. The envelope is set as three times the running standard deviation ($\pm 3\sigma$). As Figure 4.7 shows, without considerable variation in V and H_s, the propulsion power has a significant jump, up to more than 15,000 kW. The measurements that deviate from the upper and lower boundaries are excluded for machine learning model establishment.

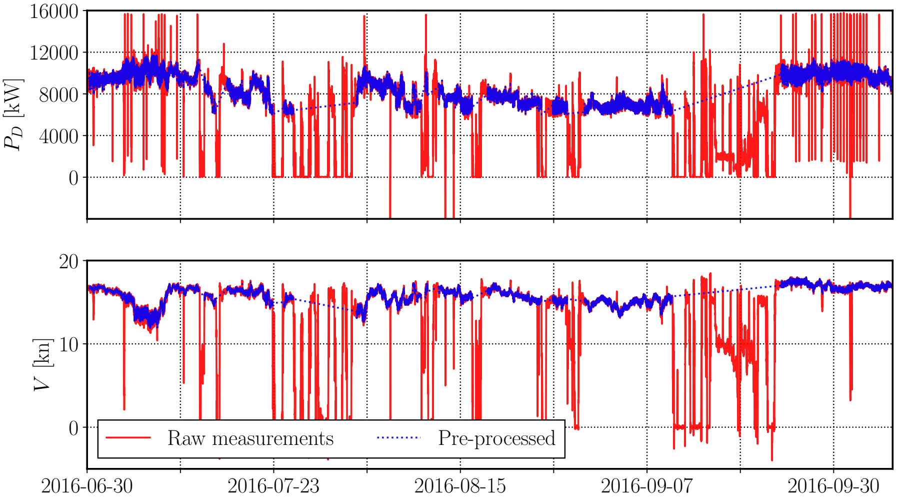

Figure 4.8: The propulsion power P_D and ship speed through water V raw measurements and after pre-processing for three-month sailing duration of the PCTC.

The raw measurements and pre-processed data of propulsion power P_D and ship speed through water V are presented in Figure 4.8. The P_D raw measurements in the solid red line have a huge fluctuation despite a stable V in the normal operation. Also, there are much lower speed and power data, related to the anchor or tug, and drastic short-term speed changes caused by ship maneuvering states. Data related to these phenomena are eliminated for the pre-processed data in the blue dotted line. The remaining P_D, V and other input features data are relatively stable and reliable for the dataset. A total of 8,632 data are fed into the following machine learning study.

4.4.3 Black-box models for fatigue assessment

The container ship case study operates the trade between Western Europe and Quebec, Canada. A total of 48 complete sailing voyages, from September 2007 to February 2010, are selected from the full-scale measurement and applied in the fatigue modeling and analysis. The other voyages were not included in this study because they were missing more than 50% of the measurements.

The focus of this study is fatigue assessment in open seas; therefore, the measurements close to coasts and shallow water areas are excluded by two spatial boundaries ($55^{\circ}W$ and $5^{\circ}W$ longitude). The applied spatial boundaries can also disregard the abnormal strain/stress samples in ports and coastal areas. Figure 4.9 shows one example of the response stress (25 Hz) for voyage 2008-03-01. The blue frame is the selected span by the spatial boundaries, and the mean value of the stresses are set to zero. It is clearly shown that the applied span consists only of the induced strain/stress in the normal navigation. The low-fluctuation strain/stress during anchor/drifting or calm water sailing near berth have been excluded.

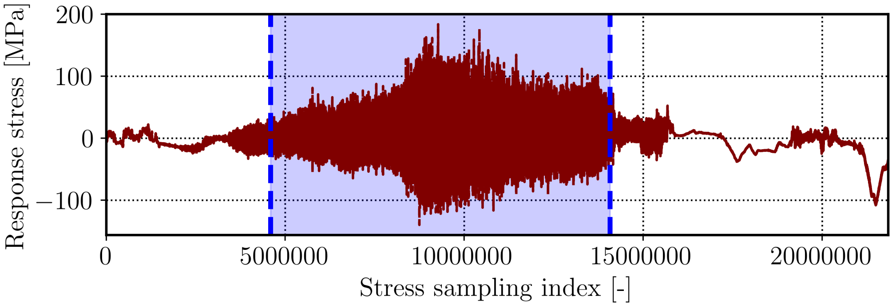

Figure 4.9: Time series of stress measured midship by the sensors relating to vertical bending-induced strain with SCF = 2, along the example voyage 2008-03-01. The blue frame is the selected study stress span by the voyage spatial boundary filter. The mean stress is set to zero.

In this study, a stationary sea state is assumed to be 30 minutes. After data synchronization and geographic boundary filtering for deep-sea conditions, the final applied sample size for fatigue machine learning modeling is 10,377.

For the i-th 30-minute stationary sea state, the fatigue damage accumulation d_i is calculated using the rainflow counting method based on the stress measurements. In addition to the ship stress response caused by wave-induced hydrodynamic loads, container vessels also need to consider two other wave-induced vibrations: springing/whipping. Figure 4.10 presents the normalized stress spectra ($\lambda_0 = 1$) by using the Fast Fourier transform (FFT) to transfer the response into the power spectral density, based on the stress measurements of the 2800TEU container ship's first westbound winter voyage in 2008. After geographic boundaries filtering, the 2008-01-06 voyage includes 277 stationary sea states, and the blue frame in Figure 4.10 (a) indicates the 150-th 30-minute sea state span.

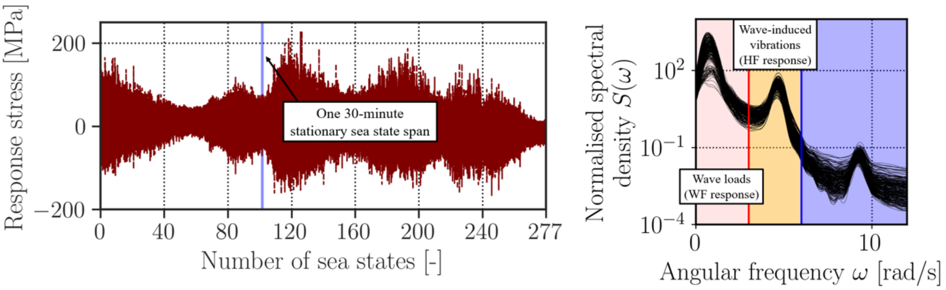

(a)

(b)

Figure 4.10: (a) the first westbound (from EU to Canada) winter voyage 2008-01-06 stress measurement span for the fatigue analysis after geographic boundaries filtering; this investigation window include 277 stationary sea states, (b) total 277 normalized spectra estimated from 30-minute stationary sea state stress measurements during this voyage.

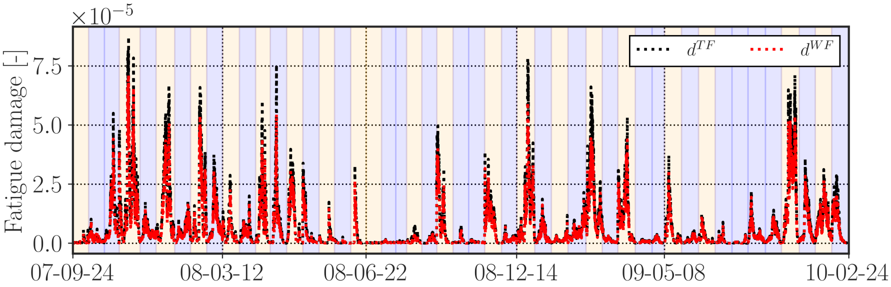

Figure 4.11: Fatigue damage d^{TF} and d^{WF} along the 48 case study voyages from September 2007 to February 2010, estimated by the rainflow counting method based on the measured stress. The orange frames represent the westbound sailing span of the voyage, and the blue frames indicate the eastbound voyages.

In Figure 4.10 (b), the typical multi-peak character of the spectra can be observed from the investigated 277 spectra. The first peak in the spectra is caused by the wave frequency ship responses, the second peak is caused by the whipping/springing, and some high-order ship responses cause the third peak (minor influence on the fatigue assessment). Here, the wave-induced hydrodynamic loads (main ship responses) are denoted as WF responses, while the wave-induced vibrations (whipping/springing) are denoted as the high frequency (HF) responses. In this study, not only the damage d^{WF} caused by the WF responses, but also the damage d^{TF} due to the total frequency (TF = WF+HF) are considered. The WF response is extracted from the total response by a Fourier analysis with a frequency range of 0-3 rad/s, and the frequency of TF is between 0-6 rad/s.

The fatigue damage along the 30-minute stationary sea states for the 48 case study voyages are estimated by the rainflow counting method, based on the measured stresses. For the 2800TEU container vessel, the Ib S-N curve with α=$10^{12.76}$ and m= 3 is assumed for the Palmgren-Miner's rule estimation in Equation (3.1). The total frequency responses-induced damage d^{TF} and wave loads-induced damage d^{WF} are presented in sailing sequence, i.e., from September 2007 to February 2010, in Figure 4.11.

CHAPTER 5

Summary of papers

This chapter presents a summary of the appended papers, including research activities, a selection of the important results, and highlights of main achievements.

5.1 Summary of Paper I

"A semi-empirical model for ship speed loss prediction in head seas and its validation with full-scale measurements"

Paper I proposes a white-box speed-power performance model for ship speed loss estimation, including improved semi-empirical formulas for added resistance due to head waves. The WBM not only provides relatively good speed loss predictions but also performs fast calculations. The improved semi-empirical formulas are derived in Section 2.3, and are verified by abundant published experimental data regarding regular head waves; see Table 4.1 in Section 4.1 for the varieties of applied ships. Full-scale measurements of the worldwide sailing PCTC and chemical tanker in Section 4.2 are used to verify the WBM.

The proposed formulas for added resistance due to head waves achieve better approximations compared to those of the two existing common approaches, the ITTC-STA2 and NTUA approaches (ITTC, 2014; Liu et al., 2016), for the verification with regular head waves. Some typical cases are presented in Figure 5.1.

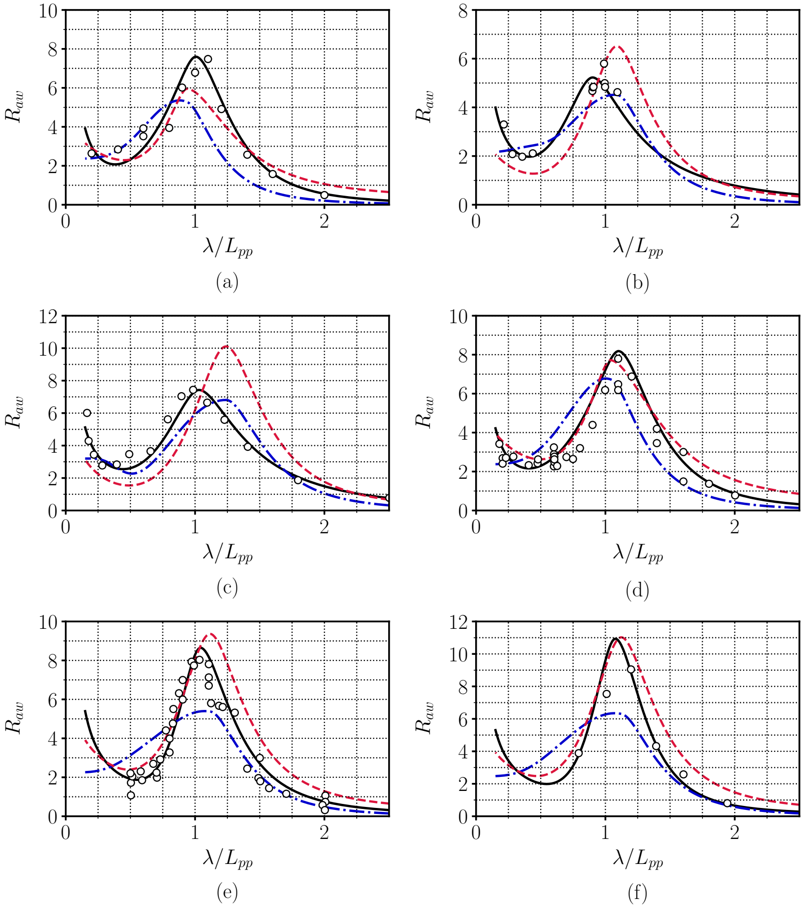

Figure 5.1: Added resistance in the regular head wave, ○ experimental data, ━━ CTH, -·-· ITTC-STA2, ---- NTUA; estimated for (a) Bulk carrier with $F_n = 0.010$, (b) DTC container ship with $F_n = 0.139$, (c) HSVA cruise ship with $F_n = 0.232$, (d) KVLCC2 tanker with $F_n = 0.142$, (e) S175 container ship with $F_n = 0.200$, and (f) S.A. Van Der Stel with $F_n = 0.250$.

Figure 5.1 (c) displays the verification and comparison for the HSVA cruise ship model test at $F_n = 0.232$. The proposed formulas (denoted as CTH) significantly improves the non-dimensional added resistance R_{aw} estimation for increases in resistance in the $\lambda/L_{pp} < 0.5$ short-wave region and for amplitude matching at the resonance region in the long-wave field. The magnitudes of the resonance resistance for the bulk carrier in Figure 5.1 (a) and the S175 container in Figure 5.1 (e) indicate that the developed formula results in better predictions than other methods. Although the remainder of the examples exhibit similar prediction performances in the resonance zone, the CTH formulas enhance the fit with regard to increases in added resistance tail of the short-wave region; see Figure 5.1 (b) for the DTC container ship and Figure 5.1 (d) for the KVLCC2 container ship.

Table 5.1: *MSE* analysis of all experimental measurement verification cases for regular head waves; outcomes are normalized by the proposed formulas results.

Ship type	Froude number	CTH	NTUA	ITTC-STA2	Best fit
S175 container	0.150	1	2.34	4.84	CTH
	0.200	1	3.90	3.26	CTH
	0.250	1	1.82	2.86	CTH
	0.275	1	1.23	12.99	CTH
KVLCC2 tanker	0.050	1	3.28	9.40	CTH
	0.090	1	1.19	3.91	CTH
	0.142	1	1.02	2.77	CTH
	0.180	1	1.10	3.01	CTH
DTC container	0.052	1	1.69	5.63	CTH
	0.139	1	4.15	2.20	CTH
HSVA cruise	0.166	1	6.70	1.11	CTH
	0.232	1	17.11	5.29	CTH
S.A. Van Der Stel	0.150	1	0.27	1.52	NTUA
	0.200	1	0.38	4.00	NTUA
	0.250	1	2.15	2.65	CTH
	0.300	1	1.66	3.40	CTH
Bulk carrier	0.000	1	5.61	2.62	CTH
	0.005	1	0.77	0.74	ITTC-STA2
	0.010	1	2.15	5.75	CTH
	0.150	1	1.19	6.33	CTH
Series 60 model 4210	0.266	1	5.81	6.67	CTH
	0.283	1	1.54	1.33	CTH
Series 60 model 4211	0.237	1	2.13	5.79	CTH
	0.254	1	4.67	4.73	CTH
Series 60 model 4212	0.207	1	3.50	10.32	CTH
	0.222	1	3.08	3.61	CTH
Series 60 model 4213	0.177	1	1.37	3.43	CTH
	0.195	1	1.03	2.52	CTH
Series 60 model 4214	0.147	1	0.96	1.83	NTUA
	0.165	1	1.03	1.48	CTH

The mean squared error (MSE) is used to evaluate the quality of all numerical predictions from a quantitative assessment viewpoint (Hastie et al., 2009). All assessment results are listed in Table 5.1. The MSE of the ITTC-STA2 and NTUA results are normalized by the values of the predicted values output by the CTH formulas. As Table 5.1 expresses, the proposed formulas have the best prediction performances for almost all the studied cases, except for three instances with the NTUA approach and one with the ITTC-STA2 formula. The introduced formulas demonstrate superior estimation ability compared with the other common methods in regular head wave conditions. Accordingly, the semi-empirical formulas are used for the calculation of wave-induced added resistance in the WBM.

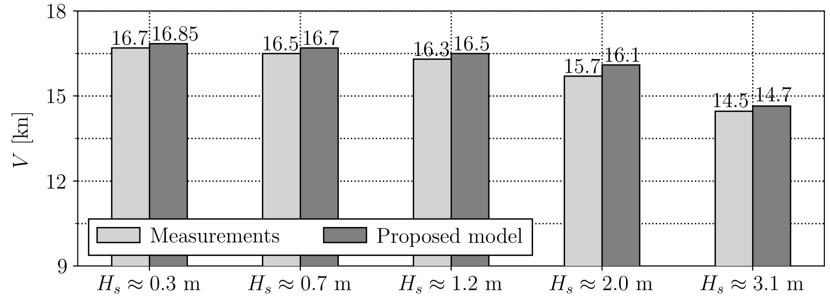

Figure 5.2: Speed prediction for the case study PCTC with various sea conditions; estimated for engine power setting of approximately 8800 kW.

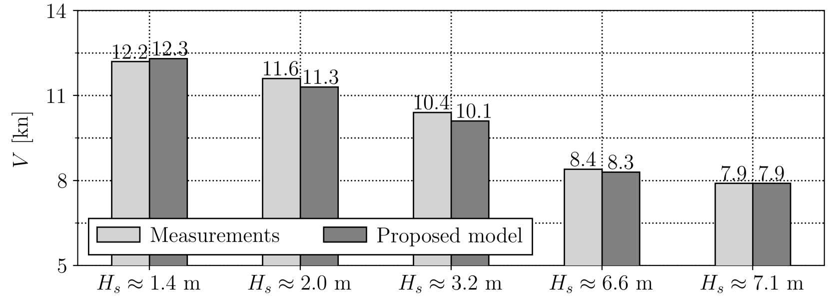

Figure 5.3: Speed prediction for the case study chemical tanker with various sea conditions; estimated for engine power setting of approximately 4300 kW.

The proposed WBM is further applied for the ship speed loss prediction in actual irregular head waves. When assessing a ship speed with real encountered wind and wave conditions, the power setting of the ship should be first defined. The pre-processed full-scale measurements with engine powers of approximately 8800 kW (60% MCR) for the PCTC and 4300 kW (52% MCR) for the chemical tanker are chosen as the power settings for the speed loss verification process. The ship speed measurements and the speed estimated by WBM, around a specific significant wave height, are averaged for comparison in Figure 5.2 and Figure 5.3. The speed under calm water conditions V_w at the defined engine power settings are 16.9 kn and 12.8

kn for the PCTC and tanker, respectively (Lang and Mao, 2020).

As Figure 5.2 illustrates, the proposed WBM produces consistently good predictions through considered wave conditions for the studied PCTC, with a maximum discrepancy of approximately 0.2 kn. The largest speed loss is approximately 2.4 kn at $H_s = 3.1$ m, which indicates a 14% involuntary speed loss caused by the encountered wave and wind conditions. Satisfactory accuracy is also observed for the chemical tanker in Figure 5.3, where the verification cases start from $H_s \approx 1.4$ m to harsh sea conditions with significant wave height around 7 m (4.5 m $< H_s <$ 5.5 m is skipped because too few measurements exist in that range). The model estimations have slight fluctuations compared to the corresponding measurements, but they are within acceptable agreement.

5.2 Summary of Paper II

"A practical speed loss prediction model at arbitrary wave heading for ship voyage optimization"

In this paper, the WBM and semi-empirical formulas developed in head waves in Paper I, are further developed to arbitrary wave heading. The improved formulas are verified by experimental data from five ships in Table 4.2. The proposed WBM is then applied for speed loss prediction and compared to the well-known Kwon (2008) method. The PCTC, chemical tanker and container ship in Section 4.2 are employed as the full-scale case study ships. The impact of such an improved speed loss prediction model on ship voyage optimization is also investigated.

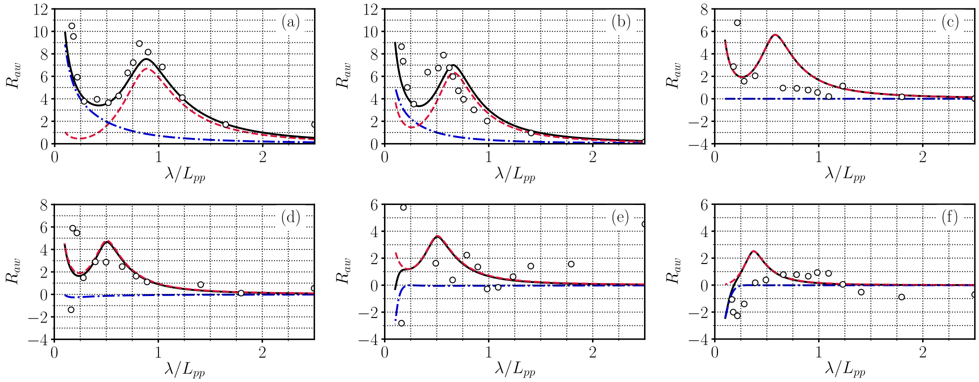

Figure 5.4: Added resistance for the HSVA cruise due to regular waves with arbitrary angles at $F_n = 0.232$, ○ experimental data, ——— R_{aw}, -·-·- R_{awr}, ---- R_{awm}; estimated at (a) 30 degrees, (b) 60 degrees, (c) 90 degrees, (d) 120 degrees, (e) 150 degrees and (f) 180 degrees.

Figure 5.4 shows one instance of the non-dimensional added resistance R_{aw} verification for the HSVA cruise ship, where the non-dimensional reflection-induced resistance R_{awr} and non-dimensional ship motion-induced resistance R_{awm} are illustrated as well. The experiment is conducted from 30° to 180°at a Froude number of $F_n = 0.232$. The proposed formulas predictions are in good agreement with the measurements for 30° and 60°, for both the tail increase in the extreme short-wave region and peak value seizing for the resonance position. Although some fluctuations exist for the other considered angles, the results align with the measurement trend. The peak value decreases and moves to the lower-wavelength (λ/L_{pp}) region as the relative wave angle increases. The negative resistance on the ship stern caused by the reflections of the following waves is captured.

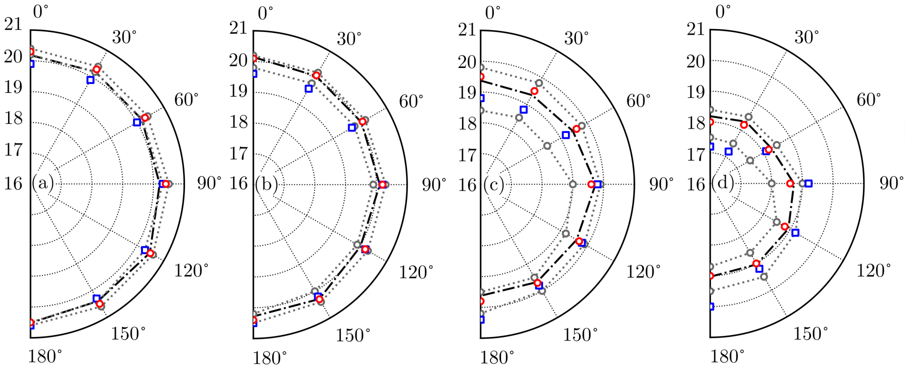

Figure 5.5: The speed loss estimation by both Kwon's method and the proposed model in comparison with the measurements for the case study container ship, ○ proposed model prediction, □ Kwon's method prediction, ⋯⋯ measured speed through water V upper and lower bound for each Beaufort scale H_s piecewise boundary, -·-·- average of real measurements; estimated for (a) BN-4, (b) BN-5, (c) BN-6 and (d) BN-7.

Figure 5.5 represents the speed loss estimation of the container ship. The speed losses predicted by the proposed WBM are consistently in relatively good agreement with the long-term averages of full-scale measurements (red circle markers coincide with the measurement averaged curve), even for the relatively harsher wave conditions. The Kwon (2008) method predicts a reasonable trend of speed loss in terms of Beaufort scales and wave headings, but the prediction errors increase as sea conditions become severer. Moreover, the Kwon (2008) method can only give one speed prediction for a specific Beaufort number, since it can not consider the specific metocean parameters, such as H_s and T_p. However, the significant wave height H_s varies greatly within the same Beaufort scale. The proposed model can also give speed estimation for upper and lower bound for wave conditions within each Beaufort scale (as the grey circle markers), which is estimated using limits of H_s within each Beaufort scale as in Table 4.5. For the blunt chemical tankers, the Kwon (2008) method even fails to give reasonable speed prediction (Lang and Mao, 2021).

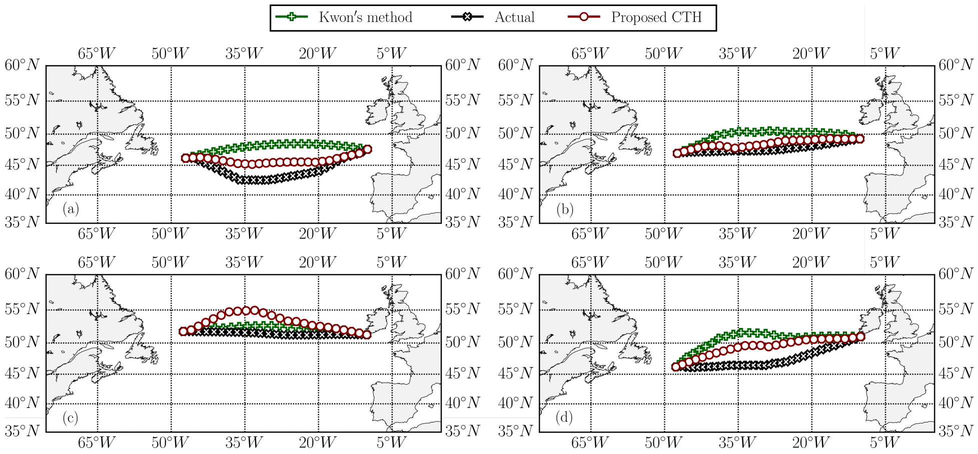

Figure 5.6: Optimal trajectories for the selected case study: (a) voyage 2009-01-18, (b) voyage 2009-02-18, (c) voyage 2009-12-26 and (d) voyage 2010-01-13.

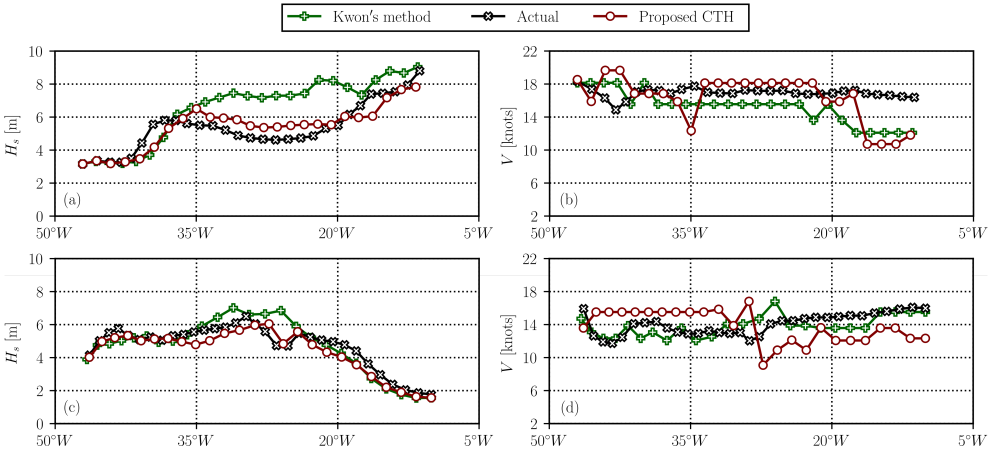

Figure 5.7: The encountered significant wave height H_s and ship speed V along the optimized and actual ship routes for the two case study voyages; (a) H_s along voyage 2009-01-18, (b) V along voyage 2009-01-18, (c) H_s along voyage 2010-01-13 and (d) V along voyage 2010-01-13.

The proposed WBM and the Kwon (2008) method are then implemented for voyage optimization of the case study container ship. Four winter voyages in the open sea, named 2009-01-18 and 2009-12-26 for eastbound, and 2009-02-18 and 2010-01-13 for westbound, are used to demonstrate how sensitive the voyage optimization results are to the accuracy of speed loss prediction models. In the voyage optimization analysis, the three-dimensional Dijkstra's algorithm (Wang et al., 2019) is applied, which allows a more flexible speed adjustment and route planning. Figure 5.6 presents the optimized trajectories for those selected routes based on the proposed model and the Kwon (2008) method. It shows that the speed loss prediction models have an essential impact on the voyage optimization results, i.e., two models lead to significantly different trajectories for the same voyage planning.

The encountered significant wave height H_s and ship speed V, along with the optimized ship routes and the actual voyages, are presented in Figure 5.7 for two typical voyages, i.e., the eastbound voyage 2009-01-18 and the westbound voyage 2010-01-13. The maximum difference of the encountered H_s for voyage 2009-01-18 is almost 2 meters. The voyage optimization using the proposed model recommends a sailing speed of 2 knots faster than that suggested by optimization with the Kwon (2008) method between the $35°W$ and $20°W$ areas, to avoid encountering harsh sea environments. When the ship encounters a large H_s above 6 m, the voyage optimization using the proposed model recommends slowing down considerably to decrease the added resistance due to waves. A similar difference can also be observed for voyage 2010-01-03, in which the route optimized by the Kwon (2008) method encounters harsher wave conditions. In contrast, the route navigated by the proposed model adjusts the speed to allow the ship to sail in the calmest possible wave conditions.

5.3 Summary of Paper III

"Comparison of supervised machine learning methods to predict ship propulsion power at sea"

This paper compares different supervised machine learning algorithms, i.e., XGBoost, artificial neural network, support vector regression and statistic methods, such as linear regression, polynomial regression and generalized additive model, to establish a black-box speed-power performance model using full-scale measurements. A generic data pre-process framework is proposed and applied in this study, including data synchronization, sea passage extraction, obvious outlier deletion, repeated values and drop-outs exclusions, maneuvering conditions and spike values detection in the raw measurements. The general ship operation parameters and encountered weather conditions are input as training features.

The results of the evaluation metrics and the training time of different models on the test set are compared and listed in Table 5.2. The machine learning models have higher accuracy than the explicitly regressed models. For the chemical tanker with a much longer measurement period, the statistical methods give worse predictions than those for the PCTC, since they cannot capture the speed-power relationship in terms of large variation of other related parameters, such as wind, wave, heading and draft. However, the time required for the statistical approaches is minimal. Especially for the linear regression and polynomial regression, the training time is less than 1 second. As for these three machine learning algorithms, although neural network and support vector regression have similar predictive capabilities to XGBoost, they require up to 10 times the training time. For the chemical tanker with a larger dataset, the training time difference is about 15 times. This is the advantage of the tree boosting system-based XGBoost method. It has good performance with much higher prediction efficiency.

Table 5.2: Accuracy measures of various machine learning data-driven models applied on the test set

Ship type	Algorithm	MAE [kW]	$RMSE$ [kW]	R^2 [-]	Time [s]
Chemical tanker	Linear regression	565.8	727.9	0.6775	<1
	Polynomial regression	379.1	490.3	0.8537	<1
	GAM	338.6	445.9	0.8789	5.3
	Neural network	57.9	89.6	0.9943	170.2
	Support vector regression	73.4	100.8	0.9938	176.6
	XGBoost	46.4	82.8	0.9958	11.7
PCTC	Linear regression	424.3	530.6	0.8415	<1
	Polynomial regression	148.6	204.7	0.9764	<1
	GAM	195.9	255.5	0.9632	1.2
	Neural network	84.0	120.2	0.9919	37.0
	Support vector regression	83.7	115.9	0.9924	12.9
	XGBoost	71.0	108.4	0.9934	3.3

For validation on unseen sailing voyages, the XGBoost model has good prediction results, where the artificial neural network and support vector regression models have much higher prediction errors and are not stable in the time series. Figure 5.8 presents one unseen voyage case study. The black markers represent the measurement data, and the red markers indicate the prediction by the XGBoost model. For this case study voyage, the XGBoost method generates the best data-driven ship performance model, with only a maximum error of about 200 kW. The prediction errors of ANN and SVR models for this voyage are significant. The physical model can predict better propulsion power than the data-driven models developed by ANN, SVR and the regression methods, with a maximum error of around 1,000 kW. The powers predicted by the physical model are constantly under the measured values during this voyage, while ANN, SVR and the statistical methods always over-predict the powers.

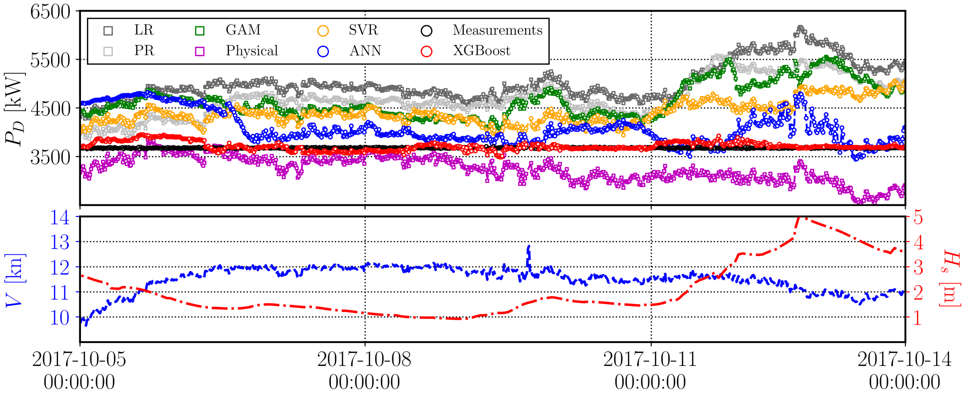

Figure 5.8: Comparison of power prediction by various models as well as ship speed V and encountered significant wave height H_s along voyage 2017-10-05.

In brief, the XGBoost model has the most stable and reliable predictive ability, with the highest model training efficiency suitable for onboard devices. The XGBoost model is applied for further analysis and discussion, and it is able to derive the ship speed-power baseline yearly or for a several-year span. Based on the sensitivity study, data volume of one year establishes a more solid data-driven ship speed-power model. The stationary period no larger than 1 hour is suggested for the machine learning modeling. For online estimation, if the previous voyage has accumulated enough data, the short-term data of about two days should be sufficient to accurately predict the propulsion power of a new voyage. It will not be ideal for unseen data, and it is necessary to continuously train with new data and update the model to achieve better results (Lang et al., 2022).

5.4 Summary of Paper IV

“Physics-informed machine learning models for ship speed prediction”

This paper proposes a novel physics-informed machine learning method to build a grey-box model predicting speed over ground for ocean crossing ships. In this method, the expected ship speed in calm water is first modeled by the physics-informed neural networks based on speed-power model test results. Then, the XGBoost machine learning algorithm is integrated to estimate ship speed reduction under actual weather conditions. The proposed GBM has been compared against the black-box model (XGBoost) using performance-monitoring data.

The $RMSE$ comparison between BBM and GBM on different individual voyages is presented in Figure 5.9. The proposed GBM has better V_g predictions for all the unseen test voyages. The mean value of the $RMSE$ is 0.5194 for the GBM and 0.6820 for the BBM, which is 30% higher. The results show that the GBM has a better predictive capability than the purely data-driven BBM. Only voyages 2, 4 and 5 have similar $RMSE$ for both models, indicating that the training data can provide enough information for prediction in those conditions for BBM. However, at voyages 3, 7, 13, etc., the GBM improved the performance dramatically due to the physical information added and enhanced prediction accuracy.

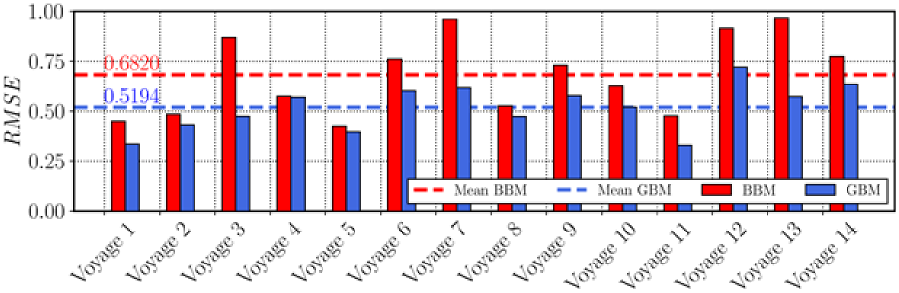

Figure 5.9: The $RMSE$ comparison for the individual voyages as a test set case study for GBM and BBM of speed over ground V_g modeling for the chemical tanker.

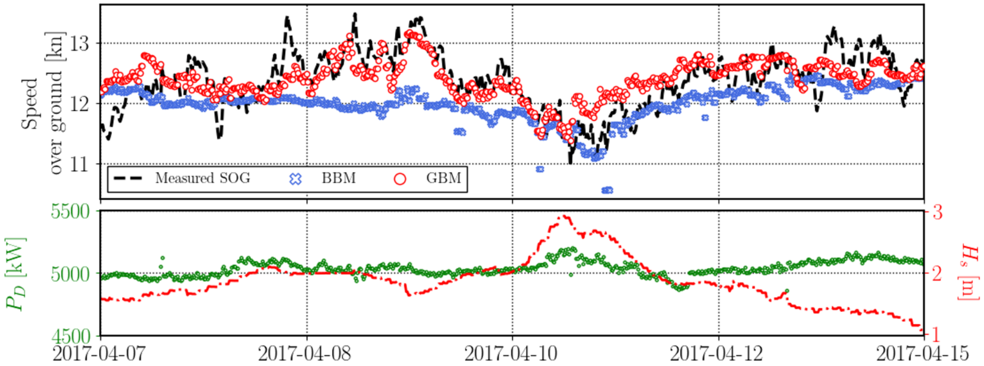

Figure 5.10: Comparison of speed over ground prediction V_g by BBM and GBM continuous learning as well as ship propulsion power P_D and encountered significant wave height H_s along voyage 5.

In reality, the model usually needs to accumulate measurement data and update itself dynamically during voyages, due to the lack of training data. This is known as continuous learning and involves recording new data and updating existing models in chronological order. To check the availability of performing continuous learning based on the GBM and BBM, several voyages of chemical tanker were selected and the data before each voyage was used to pre-train the models. The continuous learning is then conducted as data updating. See Figure 5.10 for the voyage 5 case study; the models are trained using measurements collected over two years. The results of GBM are close to the measured values, but BBM under-estimates the speed. Also, for the other voyage case studies, both BBM and GBM can predict the speed over ground with continuously updated training data. However, the GBM can improve accuracy faster and has better generalization ability than the BBM.

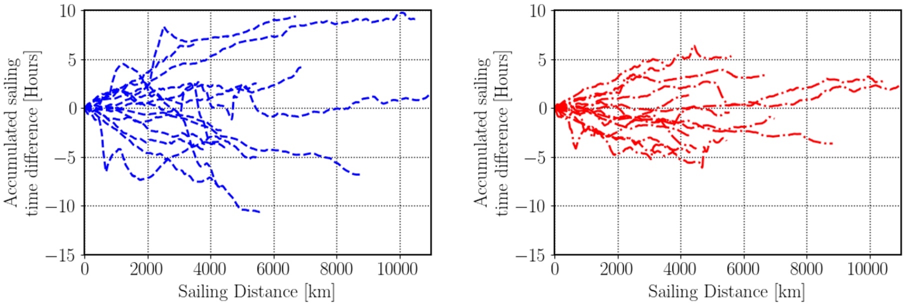

(a) BBM

(b) GBM

Figure 5.11: The accumulated error in sailing time for (a) the BBM and (b) the GBM of all 14 sailing voyages of the chemical tanker case study.

Further analysis and discussion of the comparison between the proposed GBM and BBM is conducted for ETA estimation. All 14 sailing voyages of the chemical tanker are employed for the study. Figure 5.11 (a) presents accumulated sailing time difference of different voyages for the BBM, and Figure 5.11 (b) present the results for the proposed GBM. The time differences from BBM diverge widely as the sailing distance increases, and the maximum difference exceeds 10 hours. The sailing time estimated by the GBM is much closer to the real ETA, and the dashed lines concentrate in a smaller range. The biggest discrepancy of the GBM is approximately 5 hours, which is 50% less than the BBM.

5.5 Summary of Paper V

“Impact of ship operations aided by voyage optimization on ship fatigue assessment”

This paper investigates the impact of various voyage optimizations used to assist ship operations on long-term wave statistics and corresponding fatigue life between design and operational conditions. It lists the factors that can affect the fatigue design based on stress-based approaches. Fatigue estimation relies on long-term wave statistics, which are normally provided by classification guidelines. However, different ship operations, such as slow steaming and voyage-optimization-aided operations, could greatly affect the encountered wave statistics and affect the fatigue life of the ship.

In this study, the wave scatter diagram, from the classification society guidelines for ship fatigue design, is used as a reference for comparison with the wave statistics during ship operations assisted by different voyage optimization methods. To study the impact of voyage-optimization-aided ship operation on the long-term statistics of waves encountered by a ship, three years of full-scale measurements from the container ship equipped with a hull-monitoring system are used. The hull monitoring system used has an old, conventional weather routing system using the so-called Isochrone method for voyage optimization, to guide the navigation of the ship and avoid severe wave conditions.

All encountered wave conditions during the three-year measurement campaign are extracted and statistically processed. The classification society suggested a wave scatter diagram for the North Atlantic operation and is presented for comparison in Figure 5.12, which shows that the studied ship has planned safer routes and avoided extremely harsh sea areas compared to the DNV GL (2018) guidelines.

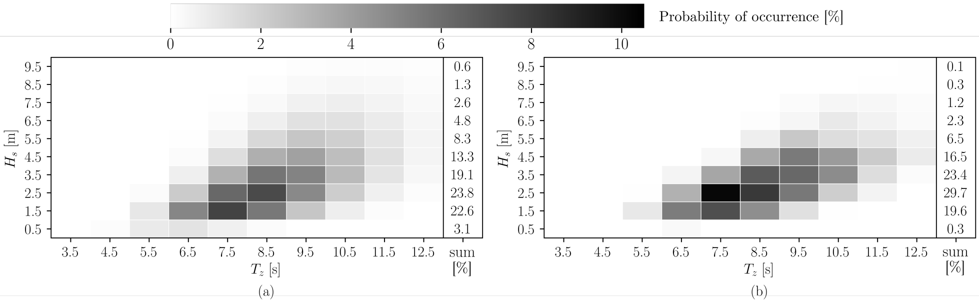

Figure 5.12: Comparison of wave scatter diagram between (a) DNV GL (2018) guidelines for North Atlantic sailing, (b) observed wave environments from the container ship case study during the three-year measurement campaign. NB: the color bar presents the probability of the occurrence of certain wave ranges.

To demonstrate the voyage optimization influence on fatigue life, the short-term encountered wave environments from four planned sailing routes of the case study ship are compared: 1) the actual routes; 2) the routes with minimum damage; 3) the routes with minimum fuel consumption; and 4) the Great Circle routes. The second and third routes are optimized by the 3D Dijkstra's Algorithm (3DDA)-based voyage optimization proposed in Wang et al. (2019). Figure 5.13 shows the fatigue damage accumulations over three years of sailing in the North Atlantic by different ship operations. It shows that the fatigue life can be effectively extended by at least 50% using voyage optimizations (Lang et al., 2020).

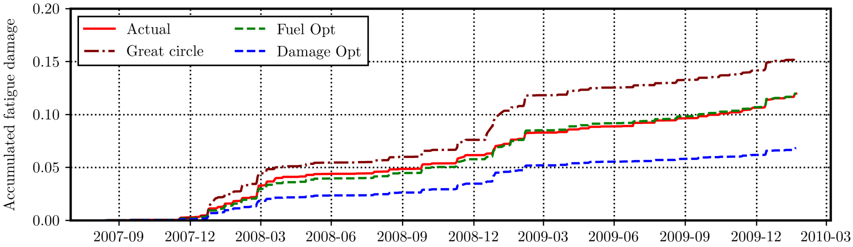

Figure 5.13: Fatigue damage accumulated along three-year measurement campaign estimated by the spectral method, where the encountered wave conditions are extracted along the actual, great circle, fuel-based optimization and damage-based optimization routes, respectively.

5.6 Summary of Paper VI

“Machine learning methods for ship fatigue assessment”

This study applied machine learning techniques to predict a North Atlantic sailing 2800TEU container vessel’s vertical bending induced fatigue damage, based on the full-scale measurement data of the onboard hull monitoring system. A generic fatigue machine learning architecture is proposed, and the model establishment consists of three scenarios. For scenario 1, the recorded ship heave and pitch motion responses $[z_2,\ z_6]$ and the related velocity $[\dot{z}_2,\ \dot{z}_6]$ and acceleration $[\ddot{z}_2, \ddot{z}_6]$ are deployed as input. The different stress spectral moments $[\lambda_0, \lambda_1, \lambda_2, \lambda_3, \lambda_4]$, wave parameters and operation profiles $[H_s, T_z, \beta, V]$ are applied for scenarios 2 and 3, respectively.

The modeling targets are wave frequency measured stress induced fatigue damage d^{WF}, and the total frequency measured stress induced fatigue damage d^{TF}, considering the high frequency whipping/springing. Based on the comparison of the test set of individual unseen voyage, the proposed machine learning models have achieved much better predictive ability than the commonly used spectral methods for d^{WF} prediction (in this study, the correction methods that split the stress response spectra are not discussed, thus, the spectral methods only investigate d^{WF}). It is also revealed that the high-frequency whipping/springing has introduced uncertainties and noise into the model establishment, especially for the motion-based model. The predictive abilities of the machine learning models for wave frequency measured stress induced fatigue damage d^{WF} are slighty better.

Figure 5.14 presents the fatigue damage d^{WF} accumulation for all 48 voyages. And the results of the best performing spectral method by Wirsching and Light (1980) d^{wl} are also shown for comparison. From the figure, the fatigue accumulations predicted by the three different machine learning models are very consistent with the measured value d^{WF}, and all have a nearly 100% increase in accuracy compared with d^{wl}.

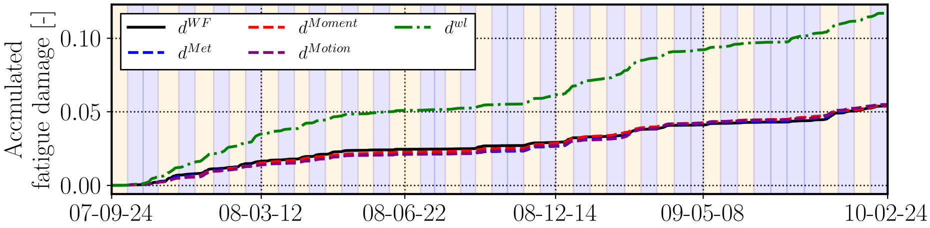

Figure 5.14: Accumulated fatigue damage for the 48 case study voyages from September 2007 to February 2010, estimated by the rainflow counting method based on the measured stress in wave frequency d^{WF}, spectral method d^{wl}, and three machine learning models d^{Met}, d^{Moment} and d^{Motion}.

Except for each individual unseen voyage as a test set, the fatigue assessment model should have the ability to assess the fatigue for a period of time in the future or for the entire life cycle of the ship. For this reason, the 33 voyages before February 2009 are applied as the training set, and the remaining 30% of the dataset (15 complete unseen voyages from February 2009 to February 2010) are used as the test set. The split is in better alignment with the needs of the shipping industry, which uses past data and weather condition forecasts to optimize ship operation.

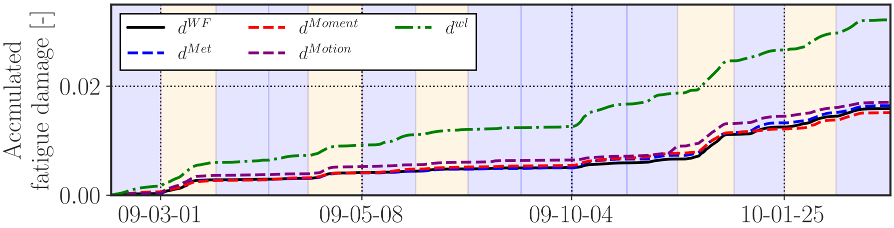

Figure 5.15: Accumulated fatigue damage along 15 unseen voyages from February 2009 to February 2010, estimated by the rainflow counting method based on the measured stress in wave frequency d^{WF}, spectral method d^{wl}, and three machine learning models d^{Met}, d^{Moment}, and d^{Motion}.

The accumulated fatigue damages during these one-year unseen sailing voyages estimated by the rainflow counting method d^{WF}, spectral method d^{wl} and machine learning models d^{Met}, d^{Moment} and d^{Moment} are presented in Figure 5.15. During the 15 cross-Atlantic navigations, the fatigue damage accumulated to 0.0159 until the end of February 2010 by d^{WF}. While the fatigue accumulation by d^{wl} still have around more than 90% over prediction than the observed fatigue d^{WF}. For machine learning approaches, the moment-based model d^{Moment} and metocean-based model d^{Met} have better predictions for d^{WF} accumulation than motion-based model d^{Motion}. The increase of d^{Moment} and d^{Met} accumulation follows the trend with observed fatigue damage d^{WF}. Although the motion-based model's predictions have some prediction discrepancy, it still has around 70% accuracy increase to the spectral method.

These results show that the machine learning models are robust and suitable for ship fatigue assessment. Based on the improvement, the ship can be operated wisely, leading to less maintenance, extended service life, and enhanced onboard safety.

CHAPTER 6

Conclusions

In this thesis, different data-driven ship performance models have been developed, focusing on speed-power and fatigue assessment modeling. Three ways to establish speed-power models have been investigated: 1) semi-empirical white-box models, 2) machine learning black-box methods, and 3) physics-informed grey-box models. The impact of ship voyage optimization on encountered wave environments and ship fatigue life has been investigated. A machine learning-based fatigue assessment model is also proposed. The main findings and conclusions are presented below, as well as the impacts of the work.

Semi-empirical white-box speed-power models

The white-box speed-power model in Paper I includes improved semi-empirical formulas for added resistance due to head waves. The formulas combine the further developed NMRI formulas (Tsujimoto et al., 2008) for short waves, and the improved semi-empirical models from Jinkine and Ferdinande (1974) for long waves. The formulas and WBM are extended to arbitrary wave headings in Paper II.

- The proposed semi-empirical formulas have been verified by experimental tests with good agreement.
- It is proven that the speed loss predictions from the proposed WBMs are better than those from the commonly used method (Kwon, 2008), in terms of the long-term averages of measurements from three full-scale case study ships. For the chemical tanker, which represents a blunt ship, the proposed model yields an

up to 40% accuracy increase under BN-6 weather conditions. The increases are as high as 7% for the PCTC (BN-6) and 6% for the container ship (BN-7).
- The importance of calibrating a generic ship speed-power performance model for reliable voyage optimization is demonstrated.

Machine learning black-box speed-power models

Different supervised machine learning algorithms are compared in Paper III, to establish a data-driven black-box ship speed-power model using full-scale measurements. A generic data pre-process framework is proposed and applied in this study. The general ship operation parameters and encountered weather conditions are input as training features.

- Based on the comparison, the XGBoost model has the most stable and reliable predictive ability, with the highest model training efficiency suitable for onboard devices.
- Data volume of one year establishes a more solid data-driven ship speed-power model. The stationary period no larger than 1 hour is suggested for the machine learning modeling.
- For online estimation, if the previous voyage has accumulated enough data, the short-term data of about two days should be sufficient to accurately predict the propulsion power of a new voyage. It would not be ideal for unseen data, and it is necessary to train continuously with new data and update the model to have better results.

Physics-informed grey-box speed-power models

Since the interpretability and extrapolation capability of unseen scenarios for pure data-driven black-box models is poor, a novel physics-informed grey-box speed-power model is proposed in Paper IV. In this model, the expected ship speed in calm water is modeled by the physics-informed neural networks (PINNs), based on a series of speed-power model test data. Then the expected ship speed, obtained in reverse from the PINNs is input into the black-box model built by the XGBoost algorithm.

- Based on the comparison of speed prediction along unseen voyages, the proposed GBM achieves much better performance than the BBM. With five years of abundant data, the GBM can improve the prediction accuracy by 30% for the chemical tanker.
- The GBM can approximate the measured values more efficiently when the training data is limited.
- Applying the proposed GBM to real maritime traffic can result in a more accurate ETA estimation. It has been proven that the GBM gives the accumulated sailing time difference at 50% lower than the BBM.

Data-driven methods for ship fatigue assessment

Through data analysis of container ships and VLCCs measurements, Paper V found that the ship operations aided by voyage optimization can influence the statistic of the encountered wave data and consequently ship fatigue life. A generic ship fatigue machine learning architecture is proposed in Paper VI, and the models are established by heave and pitch motion responses, stress spectral moments, wave parameters and operation profiles, respectively, for a 2800TEU container vessel.

- The difference in wave statistics from various optimization methods is about 10-30%.
- The ship fatigue life can be effectively extended by at least 50% by recommending optimized routes.
- Based on the long-term unseen voyage predictions, the predictions of the machine learning models have achieved at least a 70% accuracy increase compared to the traditional spectral methods.

The output of this work can contribute to higher education and research institutions with improved semi-empirical formulas for ship added resistance in waves, and knowledge of data-driven methods application in describing ship speed-power relationship and assessing ship fatigue damage in open sea navigations. Moreover, this work provides the maritime transportation industry with tools and methodology to account for ship energy efficiency and fatigue safety performance. For example, the shipping company can apply the methods for a more accurate ETA calculation, fuel consumption estimation, and performance monitoring. And the improved punctuality can help the transportation agency optimize the transport schedule for shippers' seaborne and land-based logistics. Shipping regulatory bodies can provide route planning guidance to avoid collisions with more precise ship speed estimation. Based on these improvements, the ship can also be operated wisely by embedding the proposed data-driven models in the voyage optimization system. This leads to fewer emissions and maintenance, and can extend service life and enhance onboard crew/cargo safety.

CHAPTER 7

Future work

The future research plan is to exploit the capabilities of machine learning/deep learning methods and the collected big data to improve ship performance models as well as other related applications.

Further improvements in the white-box models

The proposed white-box models can be further verified by different ships if additional full-scale measurements are available. It is reported in Mittendorf et al. (2022c), the proposed added resistance formulas have large uncertainty for a twin-screw ship with $C_B = 0.78$. More experiment tests should be collected for different ship types with C_B variation between 0.75 and 0.80, to update the boundary values of the piecewise funtion. Additionally, machine learning methods can be introduced in the modeling process to integrate ship specific parameters in the proposed formulas.

The wave height-based ship resistance and power increase correction factor is a preliminary idea for calibrating the models. A thorough investigation with additional full-scale measurements of ships should be conducted to configure a dimensionless formula for this factor based on various input parameters.

Extended applications of machine learning methods

A ship's performance at sea is strongly affected by the encountered sea environments, such as wind, wave, current, etc., denoted as sea state. A stationary sea state is a random process and is often assumed to last for from 30 minutes to several hours by the maritime community. The assumption is essential for describing stationary sea states, which are the basic inputs for quasi-static ship performance models. The available ship navigation and performance related data can help us check the reliability of this assumption. The deep learning clustering method could be applied to identify the duration of each stationary sea state from a continuous signal measurement. And a potential application for stationary sea state clustering is to give better environmental input to the ship's accumulated fatigue estimation.

Almost all current ship performance models are static/quasi-static models that estimate a ship's mean energy performance under stationary sea states (from 30 minutes to a few hours). However, ocean-going ships are mostly sailing in dynamic sea/wave environments, where a ship's response and energy performance can vary dramatically in seconds, especially under high waves. The dynamic models should be established to capture real-time dynamic changes during one stationary condition. It can be applied for optimal (auto-)control of a ship's navigation, such as fixed power/speed navigation for different shipping requirements.

A ship's energy performance changes continuously due to biofouling on ship hulls and propellers. These non-stationary properties may influence the accuracy of real-time ship performance. The deep learning methods can be used to predict the real-time performance change caused by biofouling, and develop energy efficiency measures to optimize the cleaning process.

References

Abebe, M., Shin, Y., Noh, Y., Lee, S., and Lee, I. (2020). Machine learning approaches for ship speed prediction towards energy efficient shipping. *Applied Sciences 2020, Vol. 10, Page 2325*, *10*(7), 2325.

Adland, R., Cariou, P., and Wolff, F.-C. (2020). Optimal ship speed and the cubic law revisited: Empirical evidence from an oil tanker fleet. *Transportation Research Part E: Logistics and Transportation Review*, *140*, 101972.

Alexandersson, M. (2009). *A study of methods to predict added resistance in waves* (MSc thesis). Royal Institute of Technology, Sweden.

Bal Beşikçi, E., Arslan, O., Turan, O., and Ölçer, A. (2016). An artificial neural network based decision support system for energy efficient ship operations. *Computers & Operations Research*, *66*, 393–401.

Bao, H., Wu, S., Wu, Z., Kang, G., Peng, X., and Withers, P. J. (2021). A machine-learning fatigue life prediction approach of additively manufactured metals. *Engineering Fracture Mechanics*, *242*, 107508.

Bassam, A. M., Phillips, A. B., Turnock, S. R., and Wilson, P. A. (2022). Ship speed prediction based on machine learning for efficient shipping operation. *Ocean Engineering*, *245*, 110449.

Benasciutti, D., and Tovo, R. (2007). On fatigue damage assessment in bimodal random processes. *International Journal of Fatigue*, *29*(2), 232–244.

Berthelsen, F. H., and Nielsen, U. D. (2021). Prediction of ships' speed-power relationship at speed intervals below the design speed. *Transportation Research Part D: Transport and Environment*, *99*, 102996.

BMT. (2021). Date of access: 2021-10-20. URL: https://www.bmt.org/.

Boese, P. (1970). Eine einfache methode zur berechnung der widerstandserhöhung eines schiffes im seegang. *Schriftenreihe Schiffbau*, *258*, 1–9.

Bolbot, V., and Papanikolaou, A. (2016). Parametric, multi-objective optimisation of ship's bow for the added resistance in waves. *Ship Technology Research*, *63*(3), 171–180.

Boom, H., Huisman, H., and Mennen, F. (2013). New guidelines for speed/power trials level playing field established for imo eedi. *SWZ Maritime*.

Brandsæter, A., and Vanem, E. (2018). Ship speed prediction based on full scale sensor measurements of shaft thrust and environmental conditions. *Ocean Engineering*, *162*, 316–330.

Canbulat, O., Aymelek, M., Turan, O., and Boulougouris, E. (2019). An application of BBNs on the integrated energy efficiency of ship–port interface: a dry bulk shipping case. *Maritime Policy & Management*, *46*(7), 845–865.

Carlton, J. (2012). *Marine propellers and propulsion (4th edition)*. Butterworth-Heinemann.

Cepowski, T. (2020). The prediction of ship added resistance at the preliminary design stage by the use of an artificial neural network. *Ocean Engineering*, *195*, 106657.

Chen, T., and Guestrin, C. (2016). XGBoost: a scalable tree boosting system. *Proceedings of the 22nd ACM SIGKDD International Conference on Knowledge Discovery and Data Mining*, 785–794.

CMEMS. (2019). *E.U. Copernicus Marine Service Information*. Retrieved May 18, 2019, from http://marine.copernicus.eu/

Copernicus. (2019). *Copernicus Climate Change Service (C3S): ERA5: Fifth generation of ECMWF atmospheric reanalyses of the global climate*. Retrieved May 16, 2019, from https://cds.climate.copernicus.eu/cdsapp#!/home

Coraddu, A., Oneto, L., Baldi, F., Cipollini, F., Atlar, M., and Savio, S. (2019). Data-driven ship digital twin for estimating the speed loss caused by the marine fouling. *Ocean Engineering*, *186*, 106063.

Cortes, C., and Vapnik, V. (1995). Support-vector networks. *Machine Learning*, *20*(3), 273–297.

Dalheim, Ø. Ø., and Steen, S. (2020). Preparation of in-service measurement data for ship operation and performance analysis. *Ocean Engineering*, *212*.

de Jonge, J. B. (1982). The analysis of load time histories by means of counting methods.

Dirlik, T. (1985). *Application of computers in fatigue analysis* (Doctoral dissertation). University of Warwick, UK.

DNV GL. (2015). *Energy management study 2015* (tech. rep.). Hamburg, Germany. https://www.dnvgl.com/

DNV GL. (2018). Fatigue assessment of ship structure. *DNVGL-CG-0129*.

Dong, Y., Garbatov, Y., and Guedes Soares, C. (2022). Review on uncertainties in fatigue loads and fatigue life of ships and offshore structures. *Ocean Engineering*, *264*, 112514.

el Moctar, O., Shigunov, V., and Zorn, T. (2012). Duisburg test case: post-panamax container ship for benchmarking. *Ship Technology Research*, *59*(3), 50–64.

Estrada-Flores, S., Merts, I., De Ketelaere, B., and Lammertyn, J. (2006). Development and validation of “grey-box” models for refrigeration applications: A review of key concepts. *International Journal of Refrigeration*, *29*(6), 931–946.

Faltinsen, O. M., Minsaas, K. J., Liapis, N., and Skjordal, S. O. (1980). Prediction of resistance and propulsion of a ship in a seaway. *Proceedings of the 13th Symposium on Naval Hydrodynamics*, 505–529.

Feng, C., Su, M., Xu, L., Zhao, L., Han, Y., and Peng, C. (2023). A novel generalization ability-enhanced approach for corrosion fatigue life prediction of marine welded structures. *International Journal of Fatigue*, *166*, 107222.

Fricke, W., Cui, W., Kierkegaard, H., Kihl, D., Koval, M., Mikkola, T., Parmentier, G., Toyosada, M., and Yoon, J.-H. (2002). Comparative fatigue strength assessment of a structural detail in a container ship using various approaches of classification societies. *Marine Structures*, *15*(1), 1–13.

Fricke, W. (2017). Fatigue and fracture of ship structures. In *Encyclopedia of maritime and offshore engineering* (pp. 1–12). John Wiley & Sons, Ltd.

Friedman, J., Hastie, T., and Tibshirani, R. (2000). Additive logistic regression: a statistical view of boosting (With discussion and a rejoinder by the authors). *The Annals of Statistics*, *28*(2), 337–407.

Fujii, H., and Takahashi, T. (1975). Experimental study on the resistance increase of a large full ship in regular oblique waves. *Journal of the Society of Naval Architects of Japan*, *1975*(137), 132–137.

Gaidai, O., Storhaug, G., Naess, A., Ye, R., Cheng, Y., and Xu, X. (2019). Efficient fatigue assessment of ship structural details. *Ships and Offshore Structures*, 1–8.

Gan, S., Liang, S., Li, K., Deng, J., and Cheng, T. (2017). Long-term ship speed prediction for intelligent traffic signaling. *IEEE Transactions on Intelligent Transportation Systems*, *18*(1), 82–91.

GEBCO. (2019). *GEBCO 2019 Grid*. Retrieved May 20, 2019, from https://www.gebco.net/data_and_products/gridded_bathymetry_data/#a1

Gerritsma, J., and Beukelman, W. (1972). Analysis of the resistance increase in waves of a fast cargo ship. *International Shipbuilding Progress*, *19*(217), 285–293.

GreenSteam. (2021). Date of access: 2021-10-20. URL: https://www.greensteam.com/.

Grin, R. (2012). On the prediction of wave added resistance. *Proceedings of 11th International Marine Design Conference.*

Guo, B. J., and Steen, S. (2011). Evaluation of added resistance of kvlcc2 in short waves. *Journal of Hydrodynamics*, *23*(6), 709–722.

Haranen, M., Pakkanen, P., Kariranta, R., and Salo, J. (2016). White, grey and black-box modelling in ship performance evaluation. *Proceedings of the 1st Hull Performance Insight Conference.*

Hasselmann, K., Barnett, T. P., Bouws, E., Carlson, H., Cartwright, D. E., Enke, K., Ewing, J. A., Gienapp, H., Hasselmann, D. E., Kruseman, P., Meerburg, A., Muller, P., Olbers, D. J., Richter, K., Sell, W., and Walden, H. (1973). Measurements of wind-wave growth and swell decay during the joint North sea wave project (JONSWAP). *Ergnzungsheft zur Deutschen Hydrographischen Zeitschrift Reihe.*

Hastie, T., and Tibshirani, R. (1986). Generalized additive models. *Statistical Science*, *1*(3), 297–310.

Hastie, T., Tibshirani, R., and Friedman, J. (2009). *The elements of statistical learning (2nd edition).* Springer.

Havelock, T. (1942). The drifting force on a ship among waves. *The London, Edinburgh, and Dublin Philosophical Magazine and Journal of Science*, *33*(221), 467–475.

He, L., Wang, Z., Akebono, H., and Sugeta, A. (2021). Machine learning-based predictions of fatigue life and fatigue limit for steels. *Journal of Materials Science Technology*, *90*, 9–19.

Herradon de Grado, E., and Bertram, V. (2016). Predicting added resistance in wind and waves employing artificial neural nets. *In Proc. of the 1st Hull Performance & Insight Conference, HullPIC*, *16.*

HITACHI. (2021). Date of access: 2021-10-20. URL: https://social-innovation.hitachi/en-eu/stories/energy/ai-captain/.

Holtrop, J., and Mennen, G. (1982). An approximate power prediction method. *International Shipbuilding Progress*, *29*(335), 166–170.

Hu, Z. H., Jing, Y. X., Hu, Q. Y., Sen, S., Zhou, T. R., and Osman, M. T. (2019). Prediction of fuel consumption for enroute ship based on machine learning. *Ieee Access*, *7*, 119497–119505.

Hüffmeier, J., and Johanson, M. (2021). State-of-the-art methods to improve energy efficiency of ships. *Journal of Marine Science and Engineering*, *9*(4), 447.

IACS. (2006). Guideline for Rule Development - Ship Structure, No. 106, International Association of Classification Societies.

IMO. (2011). Amendments to the annex of the protocol of 1997 to amend the international convention of pollution from ships, 1973, as modified by the protocol of 1978 relating thereto. *MEPC.203(62).*

IMO. (2020). Reduction of GHG emissions from ships, fourth IMO GHG study 2020 – final report. *MEPC 75/7/15.*

IMO. (2022). Amendments to the annex of the protocol of 1997 to amend the international convention of pollution from ships, 1973, as modified by the protocol of 1978 relating thereto. *MEPC.328(76).*

ISO. (2015). Ships and marine technology - guidelines for the assessment of speed and power performance by analysis of speed trial data. *15016.*

ISSC. (2018). Proceedings of the 20th International Ship and Offshore Structures Congress, Committee III.2: Fatigue and Fracture, M.K. Kaminski and P. Rigo (Eds.), The IOS Press.

ITTC. (2002). Resistance uncertainty analysis example for resistance test. *Recommended procedures 7.5-02-02-02.*

ITTC. (2014). Analysis of speed/power trial data. *Recommended procedures and guidelines 7.5-04-01-01.2.*

ITTC. (2017). Seakeeping experiments. *Recommended procedures and guidelines 7.5-02-07-02.1.*

ITTC. (2018). Calculation of the weather factor f_w for decrease of ship speed in wind and waves. *Recommended Procedures and Guidelines 7.5-02-07-02.8.*

Jiao, G., and Moan, T. (1990). Probabilistic analysis of fatigue due to Gaussian load processes. *Probabilistic Engineering Mechanics*, *5*(2), 76–83.

Jinkine, V., and Ferdinande, V. (1974). A method for predicting the added resistance of fast cargo ships in head waves. *International Shipbuilding Progress*, *21*(238), 149–167.

Jordan, C. R., and Cochran, C. S. (1978). In-service performance of structural details. *Ship Structure Committee, Report SSC-272, US. Coast Guard, Washington, DC.*

Jordan, C. R., and Knight, L. T. (1978). Further survey of in-service performance of structural details. *Ship Structure Committee, Report SSC-294, US. Coast Guard, Washington, DC.*

Journée, J. (2001). *Verification and validation of ship motions program SEAWAY.* Delft University of Technology Ship hydromechanics Laboratory, Report1213a.

Kadomatsu, K. (1988). *Study on the required minimum output of main propulsion engine considering maneuverability in rough sea* (Doctoral dissertation). Yokohama National University, Japan.

Karagiannidis, P., and Themelis, N. (2021). Data-driven modelling of ship propulsion and the effect of data pre-processing on the prediction of ship fuel consumption and speed loss. *Ocean Engineering, 222.*

Kim, Y. R., Jung, M., and Park, J. B. (2021). Development of a fuel consumption prediction model based on machine learning using ship in-service data. *Journal of Marine Science and Engineering*, *9*(2).

Kingma, D. P., and Ba, J. (2014). Adam: A method for stochastic optimization. *3rd International Conference on Learning Representations, ICLR 2015 - Conference Track Proceedings.*

Kuroda, M., Tsujimoto, M., Fujiwara, T., Ohmatsu, S., and Takagi, K. (2008). Investigation on components of added resistance in short waves. *Journal of the Japan Society of Naval Architects and Ocean Engineers*, *8*, 171–176.

Kwon, Y. J. (2008). Speed loss due to the added resistance in wind and waves. *The Naval Architect*, 14–16.

Lang, X., and Mao, W. (2020). A semi-empirical model for ship speed loss prediction at head sea and its validation by full-scale measurements. *Ocean Engineering*, *209*, 107494.

Lang, X., and Mao, W. (2021). A practical speed loss prediction model at arbitrary wave heading for ship voyage optimization. *Journal of Marine Science and Application*, *20*(3), 410–425.

Lang, X., Wang, H., Mao, W., and Osawa, N. (2020). Impact of ship operations aided by voyage optimization on a ship's fatigue assessment. *Journal of Marine Science and Technology.*

Lang, X., Wu, D., and Mao, W. (2022). A machine learning ship's speed over ground prediction model and sailing time control strategy. *International Journal of Offshore and Polar Engineering*, *32*(4), 386–393.

Larsson, E., Simonsen, M., and Mao, W. (2015). DIRECT optimization algorithm in weather routing of ships. *Proceedings of the 25th International Offshore and Polar Engineering Conference.*

Laurie, A., Anderlini, E., Dietz, J., and Thomas, G. (2021). Machine learning for shaft power prediction and analysis of fouling related performance deterioration. *Ocean Engineering*, *234*, 108886.

Lewis, E. V. (1988). *Principles of naval architecture (2nd edition)* (Vol. 2. SNAME). The Society of Naval Architects; Marine Engineers.

Li, Z., Mao, W., Ringsberg, J. W., Johnson, E., and Storhaug, G. (2014). A comparative study of fatigue assessments of container ship structures using various direct calculation approaches. *Ocean Engineering*, *82*, 65–74.

Liu, S., and Papanikolaou, A. (2020). Regression analysis of experimental data for added resistance in waves of arbitrary heading and development of a semi-empirical formula. *Ocean Engineering*, *206*.

Liu, S., Shang, B., Papanikolaou, A., and Bolbot, V. (2016). Improved formula for estimating added resistance of ships in engineering applications. *Journal of Marine Science and Application*, *15*(4), 442–451.

Lu, R., Turan, O., Boulougouris, E., Banks, C., and Incecik, A. (2015). A semi-empirical ship operational performance prediction model for voyage optimization towards energy efficient shipping. *Ocean Engineering*, *110*, 18–28.

Mao, W. (2014). Development of a spectral method and a statistical wave model for crack propagation prediction in ship structures. *Journal of Ship Research*, *58*(02), 106–116.

Mao, W., Ringsberg, J. W., Rychlik, I., and Storhaug, G. (2009). *Comparison between a fatigue model for voyage planning and measurements of a container vessel* (Vol. Volume 2: Structures, Safety and Reliability).

Mao, W., Ringsberg, J. W., Rychlik, I., and Storhaug, G. (2010). Development of a fatigue model useful in ship routing design. *Journal of Ship Research*, *54*(04), 281–293.

Mao, W., Rychlik, I., Wallin, J., and Storhaug, G. (2016F). Statistical models for the speed prediction of a container ship. *Ocean Engineering*, *126*, 152–162.

Maruo, H. (1957). The excess resistance of a ship in rough seas. *International Shipbuilding Progress*, *4*(35), 337–345.

Maruo, H. (1960). Wave resistance of a ship in regular head seas. *Bulletin of the Faculty of Engineering, Yokohama National University*, *9*, 73–91.

Maruo, H. (1963). Resistance in waves, research on seakeeping qualities of ships in Japan. *The Society of Naval Architects of Japan*, *8*, 67–102.

Masoudi Nejad, R., Sina, N., Ghahremani Moghadam, D., Branco, R., Macek, W., and Berto, F. (2022). Artificial neural network based fatigue life assessment of friction stir welding AA2024-T351 aluminum alloy and multi-objective optimization of welding parameters. *International Journal of Fatigue*, *160*, 106840.

Milaković, A.-S., Li, F., Marouf, M., and Ehlers, S. (2020). A machine learning-based method for simulation of ship speed profile in a complex ice field. *Ships and Offshore Structures*, *15*(9), 974–980.

Miner, M. A. (1945). Cumulative damage in fatigue. *Journal of Applied Mechanics*, *12*(3), A159–A164.

Mittendorf, M., Nielsen, U. D., and Bingham, H. B. (2022a). Data-driven prediction of added-wave resistance on ships in oblique waves—a comparison between tree-based ensemble methods and artificial neural networks. *Applied Ocean Research*, *118*, 102964.

Mittendorf, M., Nielsen, U. D., Bingham, H. B., and Liu, S. (2022c). Towards the uncertainty quantification of semi-empirical formulas applied to the added resistance of ships in waves of arbitrary heading. *Ocean Engineering*, *251*, 111040.

Mittendorf, M., Nielsen, U. D., Bingham, H. B., Gundermann, D., Schmode, D., and Deymier, C. (2022b). Performance analysis of a gas carrier using continual learning in a data stream context. *7th Hull Performance and Insight Conference (HullPIC'22)*, (May), 12.

Moe, E., Holtsmark, G., and Storhaug, G. (2005). Full scale measurements of the wave induced hull girder vibrations of an ore carrier trading in the North Atlantic. *RINA*.

Moreira, L., Vettor, R., and Soares, C. G. (2021). Neural network approach for predicting ship speed and fuel consumption. *Journal of Marine Science and Engineering*, *9*(2).

NAPA. (2021). Date of access: 2021-10-20. URL: https://www.napa.fi/.

Nielsen, U. D., Johannesen, J. R., Bingham, H. B., Blanke, M., and Joncquez, S. (2021). Indirect measurements of added-wave resistance on an in-service container ship. In T. Okada, K. Suzuki, and Y. Kawamura (Eds.), *Prac-*

tical design of ships and other floating structures (pp. 115–132). Springer Singapore.

Notteboom, T. E., and Cariou, P. (2009). Fuel surcharge practices of container shipping lines: Is it about cost recovery or revenue-making. *International Association of Maritime Economists (IAME) conference,*

Olsen, A. S., Schrøter, C., and Jensen, J. J. (2006). Wave height distribution observed by ships in the north atlantic. *Ships and Offshore Structures*, *1*(1), 1–12.

Palmgren, A. (1924). Die Lebensdauer von Kugellagern (Life Length of Roller Bearings or Durability of Ball Bearings). *Zeitschrift des Vereines Deutscher Ingenieure*, *14*, 339–341.

Parkes, A., Sobey, A., and Hudson, D. (2018). Physics-based shaft power prediction for large merchant ships using neural networks. *Ocean Engineering*, *166*, 92–104.

Perera, L. P., and Mo, B. (2018). Ship speed power performance under relative wind profiles in relation to sensor fault detection. *Journal of Ocean Engineering and Science*, *3*, 355–366.

Pérez Arribas, F. (2007). Some methods to obtain the added resistance of a ship advancing in waves. *Ocean Engineering*, *34*(7), 946–955.

Petersen, J. P., Winther, O., and Jacobsen, D. J. (2012). A machine-learning approach to predict main energy consumption under realistic operational conditions. *Ship Technology Research*, *59*(1), 64–72.

Raissi, M., Perdikaris, P., and Karniadakis, G. (2019). Physics-informed neural networks: A deep learning framework for solving forward and inverse problems involving nonlinear partial differential equations. *Journal of Computational Physics*, *378*, 686–707.

Rychlik, I. (1987). A new definition of the rainflow cycle counting method. *International Journal of Fatigue*, *9*(2), 119–121.

Rychlik, I. (1993). Note on cycle counts in irregular loads. *Fatigue Fracture of Engineering Materials and Structures*, *16*(4), 377–390.

Sadat-Hosseini, H., Wu, P.-C., Carrica, P. M., Kim, H., Toda, Y., and Stern, F. (2013). CFD verification and validation of added resistance and motions of KVLCC2 with fixed and free surge in short and long head waves. *Ocean Engineering*, *59*, 240–273.

Salvesen, N. (1978). Added resistance of ships in waves. *Journal of Hydronautics*, *12*(1), 24–34.

Shao, W., Zhou, P., and Thong, S. K. (2012). Development of a novel forward dynamic programming method for weather routing. *Journal of Marine Science and Technology*, *17*(2), 239–251.

Simonsen, M. H., Larsson, E., Mao, W., and Ringsberg, J. W. (2015). State-of-the-art within ship weather routing. *Proceedings of the 34th International Conference on Offshore Mechanics and Arctic Engineering - OMAE.*

Smola, A. J., and Schölkopf, B. (2004). A tutorial on support vector regression. *14*, 199–222.

Soner, O., Akyuz, E., and Celik, M. (2018). Use of tree based methods in ship performance monitoring under operating conditions. *Ocean Engineering*, *166*, 302–310.

Soner, O., Akyuz, E., and Celik, M. (2019). Statistical modelling of ship operational performance monitoring problem. *Journal of Marine Science and Technology (Japan)*, *24*(2), 543–552.

Storhaug, G. (2014). The measured contribution of whipping and springing on the fatigue and extreme loading of container vessels. *International Journal of Naval Architecture and Ocean Engineering*, *6*(4), 1096–1110.

Storhaug, G., Moe, E., and Lopes, T. (2007). Whipping measurements onboard a midsize container vessel operating in the North Atlantic. *Marintec China Proceedings (RINA, CMP and SNAME), International Symposium on Ship Design and Construction.*

Strom-Tejsen, J., Yeh, H., and Moran, D. (1973). Added resistance in waves. *Transactions of the Society of Naval Architects and Marine Engineers*, *81*, 109–143.

Takahashi, T. (1988). A practical prediction method of added resistance of a ship in waves and the direction of its application to hull form design. *Transactions of the West-Japan Society of Naval Architects*, *75*(75), 75–95.

Theodoropoulos, P., Spandonidis, C. C., Themelis, N., Giordamlis, C., and Fassois, S. (2021). Evaluation of different deep-learning models for the prediction of a ship's propulsion power. *Journal of Marine Science and Engineering*, *9*(2), 116.

Thompson, I. (2018). Fatigue damage variation within a class of naval ships. *Ocean Engineering*, *165*, 123–130.

Tillig, F., Ringsberg, J., Mao, W., and Ramne, B. (2017). A generic energy systems model for efficient ship design and operation. *Proceedings of the Institution of Mechanical Engineers, Part M: Journal of Engineering for the Maritime Environment*, *231*(2), 649–666.

Tillig, F. (2020). *Simulation model of a ship's energy performance and transportation costs* (Doctoral dissertation). Chalmers University of Technology, Sweden.

Tillig, F., Ringsberg, J. W., Mao, W., and Ramne, B. (2018). Analysis of uncertainties in the prediction of ships' fuel consumption – from early design to operation conditions. *Ships and Offshore Structures*, *13*(sup1), 13–24.

Tovo, R. (2002). Cycle distribution and fatigue damage under broad-band random loading. *International Journal of Fatigue*, *24*(11), 1137–1147.

Townsin, R. L., and Kwon, Y. J. (1982). Approximate formulae for the speed loss due to added resitance in wind and waves. *The Royal Institution of Naval Architects*, *124*, 199–207.

Tsujimoto, M., Shibata, K., Kuroda, M., and Takagi, K. (2008). A practical correction method for added resistance in waves. *Journal of the Japan Society of Naval Architects and Ocean Engineers*, *8*, 177–184.

Tucker, M., and Pitt, E. (1990). *Waves in Ocean Engineering* (1st Edition). Ellis Horwood Ltd.

UNCTAD. (2018). *Review of maritime transport 2018*. United Nations Publications, New York, USA.

Ursell, F., and Dean, W. R. (1947). The effect of a fixed vertical barrier on surface waves in deep water. *Mathematical Proceedings of the Cambridge Philosophical Society*, *43*(03), 374–382.

Uyanık, T., Karatuğ, Ç., and Arslanoğlu, Y. (2020). Machine learning approach to ship fuel consumption: A case of container vessel. *Transportation Research Part D: Transport and Environment*, *84*, 102389.

Valanto, P., and Hong, Y. (2015). Experimental investigation on ship wave added resistance in regular dead, oblique, beam, and following waves. *Proceedings of the 25th International Society of Offshore and Polar Engineers*.

Vitali, N., Prpić-Oršić, J., and Guedes Soares, C. (2020). Coupling voyage and weather data to estimate speed loss of container ships in realistic conditions. *Ocean Engineering*, *210*, 106758.

Wang, H., Mao, W., and Eriksson, L. (2017). Benchmark study on different weather routing optimization algorithms.

Wang, H., Lang, X., Mao, W., Zhang, D., and Storhaug, G. (2020). Effectiveness of 2D optimization algorithms considering voluntary speed reduction under uncertain metocean conditions. *Ocean Engineering*, *200*, 107063.

Wang, H., Mao, W., and Eriksson, L. (2019). A Three-Dimensional Dijkstra's algorithm for multi-objective ship voyage optimization. *Ocean Engineering*, *186*, 106131.

Wang, S., and Meng, Q. (2012). Sailing speed optimization for container ships in a liner shipping network. *Transportation Research Part E: Logistics and Transportation Review*, *48*(3), 701–714.

Winterstein, S. R. (1985). Non-normal responses and fatigue damage. *Journal of Engineering Mechanics*, *111*(10), 1291–1295.

Winterstein, S. R. (1988). Nonlinear vibration models for extremes and fatigue. *Journal of Engineering Mechanics*, *114*(10), 1772–1790.

Wirsching, P. H., and Light, M. C. (1980). Fatigue under wide band random stresses. *Journal of the Structural Division*, *106*(7), 1593–1607.

Woud, H. K., and Stapersma, D. (2002). *Design of propulsion and electric power generation systems*. MarEST, Institute of Marine Engineering, Science; Technology.

Yamamoto, N. (2017). Fatigue evaluation of ship structures considering change in mean stress condition. *Welding in the World*, *61*(5), 987–995.

Yan, W., Deng, L., Zhang, F., Li, T., and Li, S. (2019). Probabilistic machine learning approach to bridge fatigue failure analysis due to vehicular overloading. *Engineering Structures*, *193*, 91–99.

Yang, P., Li, J., Zhang, W., Wu, D., Gu, X., and Ma, Q. (2021). Analysis on statistical uncertainties of wave loads and structural fatigue reliability for a semi-submersible platform. *Ocean Engineering*, *237*, 109609.

Yasukawa, H., and Masaru, T. (2020). Impact of bow shape on added resistance of a full hull ship in head waves. *Ship Technology Research*, *67*(3), 136–147.

Yoo, B., and Kim, J. (2019). Probabilistic modeling of ship powering performance using full-scale operational data. *Applied Ocean Research*, *82*, 1–9.

Yosri, A., Leheta, H., Saad-Eldeen, S., and Zayed, A. (2022). Accumulated fatigue damage assessment of side structural details in a double hull tanker based on spectral fatigue analysis approach. *Ocean Engineering*, *251*, 111069.

Yuan, Z., Liu, J., Zhang, Q., Liu, Y., Yuan, Y., and Li, Z. (2021). A practical estimation method of inland ship speed under complex and changeful navigation environment. *IEEE Access*, *9*, 15643–15658.

Zhang, C., Zhang, D., Zhang, M., and Mao, W. (2019). Data-driven ship energy efficiency analysis and optimization model for route planning in ice-covered Arctic waters. *Ocean Engineering*, *186*, 106071.

Zhao, W., and Baker, M. J. (1990). *A new stress-tange distribution model for fatigue analysis under wave loading* (Vol. Environmental Forces of Offshore Structures and their Prediction).